THE UNIVERSITY *of* EDINBURGH

Farm level power curves for wind integration studies considering turbine wake and complex terrain effects

Abdulmutalib Yussuff
Institute for Energy Systems
The University of Edinburgh

A thesis submitted in fulfillment of the requirements for the degree of
Master of Science

THE UNIVERSITY *of* EDINBURGH
School of Engineering | Institute for Energy Systems

August, 2017

Declaration

I hereby declare that the review, analysis, and report contained in this dissertation were prepared entirely by myself and it is the product of my personal academic research in the field of sustainable energy systems at The University of Edinburgh. The contributions received from other researchers, resource persons, publications, and other relevant sources are duely cited and acknowledged.

The methodology and results of the computational fluid dynamics (CFD) simulation in Chapter 9 and Chapter 10 were based on the documentation of the Wind Farm Design and Optimisation models which I studied. Other analyses were based on industry standard packages used in GIS mapping, Digital Terrain Modelling, and analytical tools in MATLAB, Excel spreadsheet and Rstudio. Some of the analyses in Section 6.4 are based on the research by Timmers (2017).

The most challenging aspect of this research work is having to leverage industry standard packages in wind energy industry at a subsidized cost, which is not accompanied with the company's full technical support as per the company's Terms and Conditions on subsidized license. Some offered student license for free but with limited functionalities. Therefore, huge time investment on self-study through webinars, on-line materials leading to a significant amount of literature reviews.

Abdulmutalib Yussuff

August, 2017

Acknowledgements

I would like to gratefully acknowledge the guidance and encouragement of my supervisor, Professor Gareth Harrison, and members of the Institute for Energy Systems at the University of Edinburgh. My gratitude extends to my Personal Tutor, Dr. Sasa Djokic who guided me through all the challenging moments in my studies. I remain grateful for the tutelage and counsel. I also appreciate my thesis examiner, Dr. Camilla Thomson for her comments and suggestions.

My appreciation goes to the WindSim and AWS Truepower support team for providing subsidized academic versions of their wind farm design and data processing tools which were greatly helpful for this research work. Many thanks to Dr. Giorgio Crasto for his verbal guidance on best practices in wind resource assessment. Thanks to all my amazing coursemates whom made my overall study experience a greater one.

Finally, I remain grateful to the Foreign and Commonwealth Office, and the University of Edinburgh for providing the financial support that enabled me undertake my graduate programme in the United Kingdom.

Abstract

The increasing penetration of variable energy vector such as wind comes with enormous challenges. To surmount this, one of the important tasks in wind integration studies is the accurate forecasts of energy yield both in long and short terms to ensure the security of network and supply, and ultimately a penalty-free electricity trading. These activities require accurate knowledge of local wind climate at micro-scale level. However, microscale-quality data are seldom available and on-site wind measurement takes time. Wind dataset from met stations are usually collected at 10 metres height which is quite poor to be extrapolated to wind farm site and to boundary layer. Regional wind dataset on the other hand is collected at a resolution that is too coarse to capture short-scaled and short-lived local effects such as terrain and/or wake-induced turbulence.

This work combines an industry-standard microscale model by WindSim with WRF mesoscale model at 3 km resolution to obtain a downscaled, terrain- and wake-modified dataset with 300 metres resolution suitable for local wind climate predictions. The coupled model uses eleven years WRF dataset (2000-2010) as initials and inlet boundary conditions (BCs), a fixed pressure as the top BC, and the site's DTM dataset as the bottom BCs to drive CDF simulation in WindSim. The study site is 7km $\times$ 7km covering the entire Braes of Doune wind farm in Scotland. The refined dataset is probably the first attempt to downscale the recently developed regional WRF mesoscale model for a specific site in the UK by taking cognizance of terrain and wake effects. The results from the coupled model are verified in two steps- first, against the actual production data from ELEXON, and then against the previous power curve derived by fitting warranted power curve to the WRF dataset. To investigate the directional dependecy of power curves, a set of representative power curves are derived for 12 sectors at 30° interval. In addition, the vertical and directional profiles of wind speed, inflow angle, wind shear/exponent, turbulent kinetic energy, and turbulence intensity are derived for the study site.

The fidelity of the downscaled dataset to model the actual production pattern is demonstrated, and a set of normalized directional power curves and vertical profiles of micro-scale variables are predicted as representative of the wind farm site and could be used to predict power output, tendencies for turbine loading, and wind farm feasibility studies specific to the site.

Contents

Figures and Tables

Figures

Tables

Chapter 1

Introduction

This chapter gives a brief background on the wind energy issues in the global and the UK contexts. It is divided into four sections: Section 1.1 introduces the development in wind power deployment following the 1997 Kyoto protocol which served as a turning point in the energy and climate policies of most countries; Section 1.2 gives outline of the project deliverables; Section 1.3 gives a summary of project scope and contribution to knowledge; while Section 1.4 summarizes the overall organization of the chapters in this thesis.

1.1 Background

The global energy landscape has seen growth in wind energy generation due to ambitious climate change policy targets and the concerted effort against global climate change. In 2015, the global installed capacity of wind power reached about 435 GW or 7% of global power generation capacity, a record growth of 17.2% compared to 16.4% in 2014 [1]. Since the Kyoto protocol was adopted in Japan on December 11, 1997, wind power capacity addition (including onshore and offshore) has continued to increase on annual basis (see Figure 1.1), with the bulk of the increase, about 97% in 2014, coming from onshore capacity (see Appendix A.1) [1]. Onshore wind is relatively cheap compared to other renewable energy technologies (Appendix A.1, Figure A.1.1).

In the United Kingdom (UK), the total installed wind capacity in 2016 is about 14.5 GW including about 63% of onshore capacity [2]. Wind energy generation has been prolific with contribution of 11% and 17% in the whole of 2015 and in December 2015 respectively. In Appendix A.1, Figure A.1.3, the combined onshore and offshore wind capacity meets 13.5% of UK's annual power demand, while onshore wind power alone meets about 8%.

Based on the updated Renewable Energy Roadmap published by the UK DECC in 2013, the UK has exceeded its 15% renewables target sets out in the 2009 Renewable Energy Directives [3].

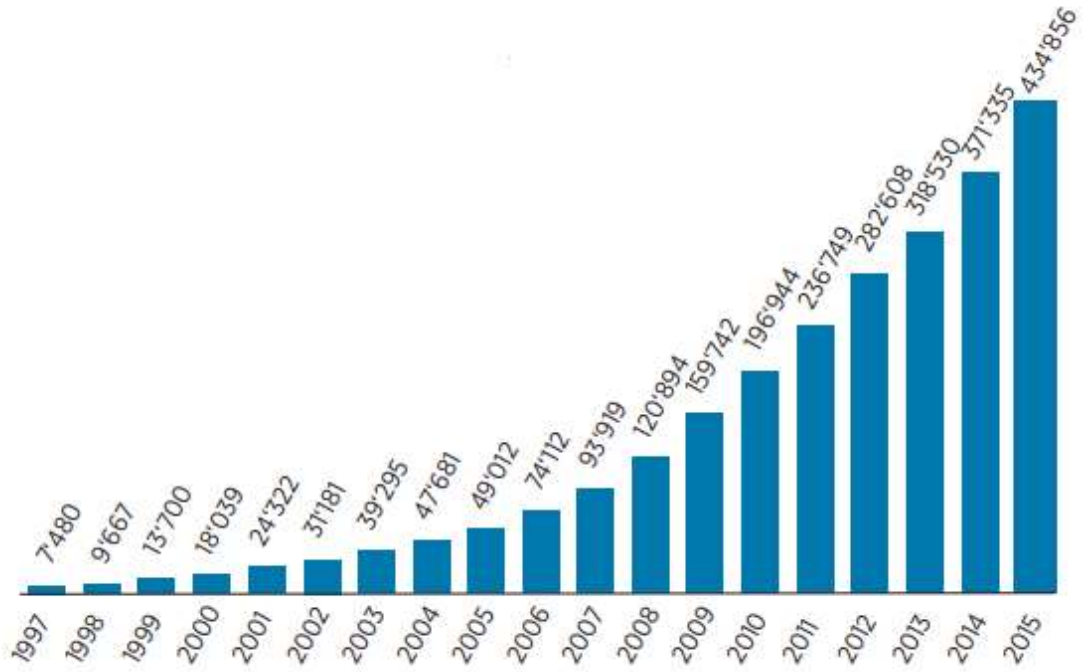

Figure 1.1: World total installed wind capacity (MW) post 1997 Kyoto [1]

Scotland on the other hand, sets out an ambitious target of reaching 100% renewables by 2020 [3]. Similarly, countries around Europe are increasing wind capacity in their energy mix due to its relatively low levelized cost of electricity (LCOE) and the opportunity for job creation. The increasing deployment also sees rapid improvement in size and sophistication of wind energy technologies such as rotor, mast, and control systems. The implication is the increasing scale and complexity of wind farms as more locations are exploited for wind energy generation [1].

As the investment in wind energy generation grows, the variability and technical limitation issues associated with wind energy will expectedly become more pronounced. The daunting engineering challenges that characterized grid integration of wind energy include those associated with variability of wind flow and aerodynamics. While it is difficult to gain control over wind variability, the challenges arising from wind turbine aerodynamics could be curtailed or minimized through sophisticated design of wind turbines and advanced wind farm planning and optimisation considering turbine wake and terrain related effects.

Wind farm design and optimisation is usually anchored on accurate wind resource assessment, a precursor for wind farm output forecasts. Several research efforts have been geared towards

making accurate wind resource data available to support wind farm output forecasts. One of such effort is the recent numerically simulated wind resource data for the entire regions of the United Kingdom (UK) developed at the Institute for Energy Systems, The University of Edinburgh using The Weather Research and Forecasting (WRF) Model. While the simulated wind resource data from WRF model sufficiently explains atmospheric processes that are about the size of a grid, it does not sufficiently explain processes that occur in short length of time and space which are central to grid integration of renewables.

This project addresses the gap in the foregoing by complimenting the WRF model with a higher resolution CFD model, and develop a new coupled model with spatio-temporal resolution sufficient for processes that occur at a local scale. It also provides critical review of wind integration studies, existing coupled models including their strengths and weaknesses, and the methodologies for incorporating effects of turbine wake, and terrain in the coupled model.

1.2 Aims and Objectives

The main goal of this project is to couple WRF mesoscale and WindSim CFD microscale models to simulate combined effects of wind turbine wake and site terrain on the performance or aggregate power curve of a wind farm for different wind directions. The objective is to generate wake and/or terrain modified wind datasets at higher spatio-temporal resolution which could be used to predict the anisotropic performance of a wind farm.

To achieve these aims, a set of specific tasks were accomplished:

- Develop a digital terrain model (DTM) for the case study wind farm;
- Employ WRF modelled wind datasets in combination with digital terrain, and wake models to drive computational fluid dynamics (CFD) simulation in WindSim;
- Develop wind resource maps and wind roses for the case study wind farm;
- Model the anisotropic profiles of the wind farm variables;
- Develop directional power curves for the wind farm;
- Compare the power forecasts from the above steps with actual production data;
- Establish uncertainties and conduct sensitivity analyses.

1.3 Scope and contribution to knowledge

This project uniquely brings the methodologies of developing Digital Terrain Model for any wind farm using third-party tools and its coupling with Wind Farm Design tools for the simulation of wind flow over complex terrains. It brings together latest advances in the downscaling of mesoscale Numerical Weather Prediction (NWP) model in wind energy industry and the overall linkage between the subject of improved forecasts of wind farm performance and wind integration studies. However, it does not attempt to validate the robustness of the wind farm design tools used but rather rely on the strengths presented by the WindSim CFD model, complimented by analytical tools including MATLAB, and R. The study focuses on answering such questions as the best practices in downscaling mesoscale model to a resolution suitable for predicting the performance of local wind farms, coupling the mesoscale with microscale models capable of considering the effects of site-specific characteristics that have impacts on wind farm output, and the extent to which turbine wake and site terrain modify wind flow.

1.4 Thesis outline

- **Chapter 1**: This chapter gives background on the wind energy issues in global and UK context; outline of project deliverables, and the contributions to knowledge.
- **Chapter 2**: This chapter marks the onset of literature review with emphasis on the concept of wind integration studies and where power curve fits in the accurate wind forecast for reliable operation and dispatch of reserve capacity.
- **Chapter 3**: In this section, the governing equations for modelling of atmospheric processes, including processes that occur on global, regional, and local scales at various temporal and spatial resolutions. This helps to shed lights on the global circulation models and reanalysis data which form the cradle of the mesoscale data used in this study. It also gives background on linear and non-linear microscale models, the atmospheric boundary layer and its thermal stratification, and the integration between pressure gradient force and Coriolis force that gives rise to the geostrophic wind type that is downscaled in this study.

- **Chapter 4**: In this section, the models discussed in chapter 3 are summarized and the various approach to downscale them are highlighted, including the strength and weaknesses of the methods.
- **Chapter 5**: This gives background on previous attempts by some authors in coupling mesoscale and microscale models to simulate local wind climate, particularly for wind energy application.
- **Chapter 6**: A background study on some wake models are presented in this section, including their strengths, weaknesses, and on-going research aimed at improving their wake prediction accuracies. This gives pointers on how the wake models used in WindSim simulation works and their key input requirements.
- **Chapter 7**: The general concept of digital terrain modelling and where it fits in wind energy integration is summarized in this section. Also, the various approach and key sources of data for DTM are highlighted.
- **Chapter 8**: This section gives background on the Reynolds averaged Navier-Stokes equation that forms the governing equation of fluid flow used in WindSim simulation. Also, various turbulence closure schemes used in literature to resolve the RANS equation are discussed in details, and the boundary conditions types relative to WindSim simulation. The connection between the turbulence closure schemes and atmospheric stability is also highlighted.
- **Chapter 9**: Some of the major analytical and simulation tools used in this study are discussed, including flowcharts highlighting key steps from beginning to the end. Also included are qualitative discussion on general inputs required for the simulation, including turbine specification, virtual climatology, and steps such as discretization of computational domain preparatory to the CFD simulation.
- **Chapter 10**: This section gives major deliverables and findings in this study, including the wind farm characteristics layout, turbulence and wind shear parameters, wake characteristics, and annual energy production specific to the study site. Some of the discussion in this section related to data and figures presented in Appendix A.3 and in previous literature review sections.
- **Chapter 11**: The central discussion in this section is on the relationship between the findings from this study, the literature review, possible sources of uncertainties, and the limitations of the coupled model.

- **Chapter 12**: This section highlight key findings, and the direction for future studies to compliment this study.
- **Appendix A.1**: A long list of referenced datasets, and results obtained in this work.
- **Bibliography** Appendix A.4.1: A long list of publications, lecture notes, and other sources of information cited for this work based on IEEE referencing system.

Chapter 2

Wind integration and power curves

This chapter marks the onset of literature review with emphasis on the concept of wind integration studies and where power curve fits in the accurate wind forecasts for reliable operation and dispatch of reserve capacity. Section 2.1 focuses on the rationale behind wind integration studies and outline the shortcomings in grid integration of variable renewable energy (VRE) such as wind. Section 2.2 discusses wind power curves, and the various sources of wind data which have been used in literature for the purpose of wind integration studies, including their limitations. Because wind farm is a complex system with several processes which are critical in understanding wind farm design and optimization, Section 2.3 is introduced to give a dynamic picture of a typical wind farm processes, and the corresponding activities that are carried out to minimize impacts (in the case of undesirable ones), or maximize imapcts of the desirable processes.

2.1 Wind integration and variability issues

Wind integration studies (WIS) came into the spotlight of global attention as large amounts of wind power are getting connected to power networks in various jurisdictions. As large-scale wind power projects become interfaced with power systems, the innate variability of wind and its downsides become more pronounced. This necessitates the need for a more informed decision in the planning of power systems to handle more variable resources such as wind, and ultimately meet grid code requirements such as Fault Ride Through (FRT) or Low Voltage Ride Through (LVRT) which have high degree of likelihood in a typical power system. These also have implication on the network protection requirements to assure security of power supply. The behavior of Wind Turbine Generators (WTGs) connected to the grid is largely influenced by the wind flow characteristics, and this means that accurate predictions of wind behaviour is key to taking preventive measures. Although the WTGs are designed with control systems to

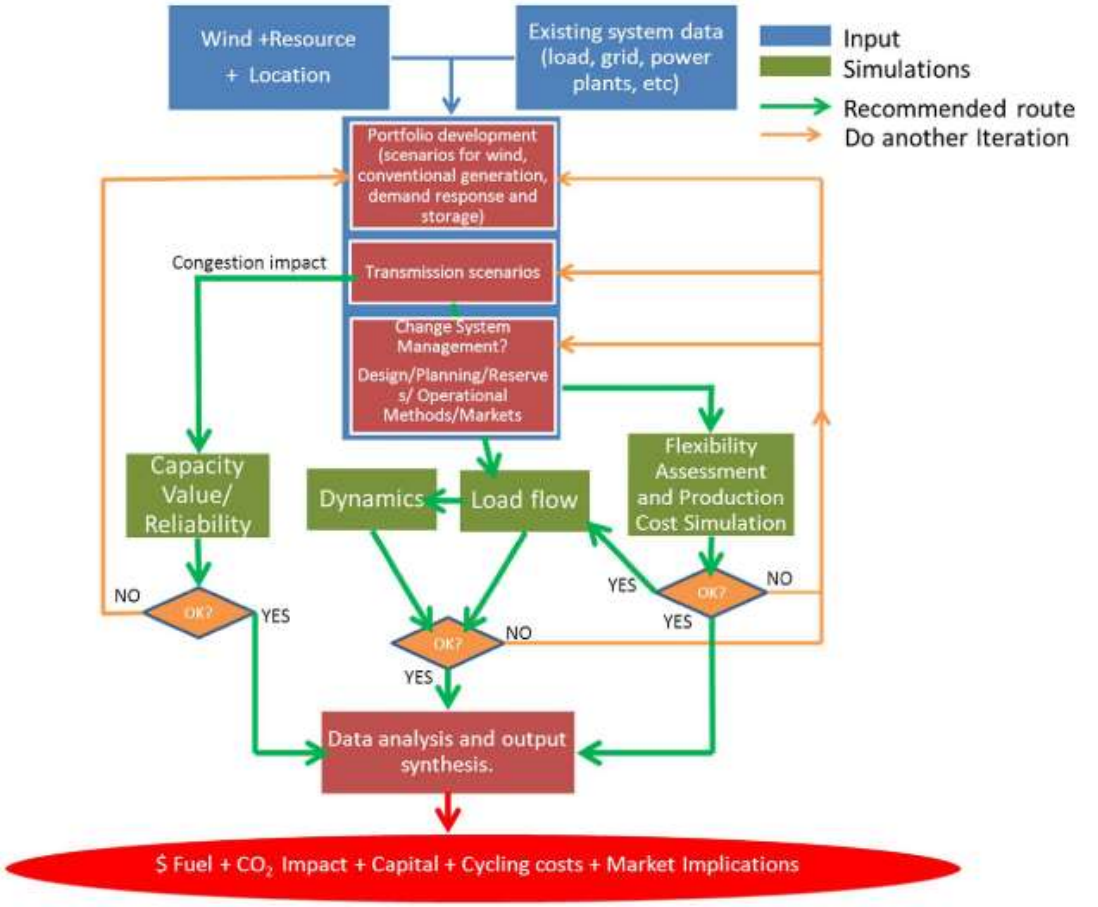

Figure 2.1: Components of wind integration study [5]

self-regulate in the event of faults or changes in operating conditions and provide the inertia to sustain such changes over a short time, the control mechanisms require set-points derived from accurate knowledge of wind resource at the site.

Essentially, wind integration studies simulate a future power system with large-scale penetration of wind power in the range of 5-20% share of electricity supply mix annually [4, 5]. The studies are usually targeted at evaluating the impacts of hooking up WTGs to the grid, particularly on grid variables such as fault level, and/or protection requirements, and scheduling for optimal dispatch in times of good wind resource forecasts.

Wind integration studies is a complicated process involving several approaches and steps including wind resource assessment, existing demand and generation data, scenarios of planned generation, storage, and anticipated demand response. Transmission scenarios including load flow, reliability, and other steps shown in Figure 2.1 [5].

2.2 Power curves and data source

From the foregoing discussion in Section 2.1, Figure 2.1, the key input required at the on-set of wind integration studies include wind resource, site-specific information, and load forecasts. The overall outcome of wind integration studies depends on the accuracy of these input data, hence the need for improved farm level power curves capable of predicting wind farm outputs at different wind speeds and direction. This inform the emphasis placed on deriving directional power curves as well as anisotropic profiles of wind farm variables as conducted in /Autoref.

A review conducted by Dowds et al. (2015) on twelve large-scale and major wind integration studies across the United States and the Europe reveals that the bulk of these studies made use of wind speed data derived from mesoscale numerical weather prediction (NWP) models, which underestimate the need for power balancing and ramping resources (reserves) required to sustain power systems reliability always [4]. The review consists many elements, and of interest to this study is the aspect pertaining to sources of wind data. From the reviewed wind integration studies, three types of data source were used - including historical production data from established wind farm, wind measurement campaigns using anemometers or LIDAR systems at the site of interest, and mesoscale numerical weather prediction (NWP) model such as the WRF model. These data sources offer different degree of uncertainties in terms of quality, spatio-temporal resolution, availability [4], and the associated cost of collection. The proprietary issues with actual wind farm production data and the lack of willingness to disclose them was identified as a key challenge. The progress made by public organizations such as the Department of Energy's National Renewable Energy Laboratory (NREL) in making data publicly available to advance wind integration studies were also discussed.

Historical production data gives a clearer profile of wind farm performance and makes it easier to predict the grid impacts of wind resource variability and wind farm curtailments. It is also useful for evaluating the balancing reserves requirement in the event of poor wind resource. The inherent uncertainties with actual production data include the differing spatio-temporal variation of wind across sites, and the likelihood of curtailment that create gaps in data availability. These uncertainties make it difficult to reproduce production data of one site for use in another site except of course, where information on extent of spatio-temporal variability in weather conditions exist.

Alternatively, empirical wind speed data could be gathered by on-site measurement using

anemometer or LIDAR systems. The data could then be translated into power equivalent. The issue with this type of data are majorly two-fold: The prohibitive cost of data collection, and the challenges with obtaining wind resource data at hub-height. Most on-site wind measurement data that are publicly available are collected at 10 metres height and based on assumptions about stably stratified atmospheric boundary layer (ABL) and surface roughness which are seldom the case. So, it is difficult to accurately estimate wind resource characteristics at hub height using the 10 meters data. Where the wind resource data at hub height is available, the conversion to wind power equivalent by matching with the turbine manufacturer's power curve also introduces some degree of uncertainty. For instance, wind anemometer measures a single point wind speed in space without accounting for spatial variability. However, a WTG is driven by multiple wind speed vectors at its vicinity. In addition, WTGs create shadowing effects, and shed vortices behind rotors. These effects put the WTGs at the subsequent rows in the wake of the preceding turbines. The implication of this in a wind farm with multiple turbines is that some WTGs downstream will receive less wind speed but more wake-induced turbulence leading to reduced output, and shortened life-span. There are also events of wake-wake and wake-terrain interactions further affecting wind farm performance. Another known alternative source of wind speed data is the mesoscale numerical weather prediction (NWP) models. NWP predicts the prevailing weather conditions using the mathematical models of oceans and atmosphere in combination with initial and boundary conditions, and advanced computational resources. Weather models involve non-linear systems of partial differential equations based on the laws of mass, momentum, and energy in three-dimensional coordinates. Most wind integration studies are based on NWP models because it does not require costly on-site measurement campaigns. Similarly, this study is also based on one of the subsets of NWP model known as the Weather Research and Forecast (WRF) model discussed in details in the next section 2.2.

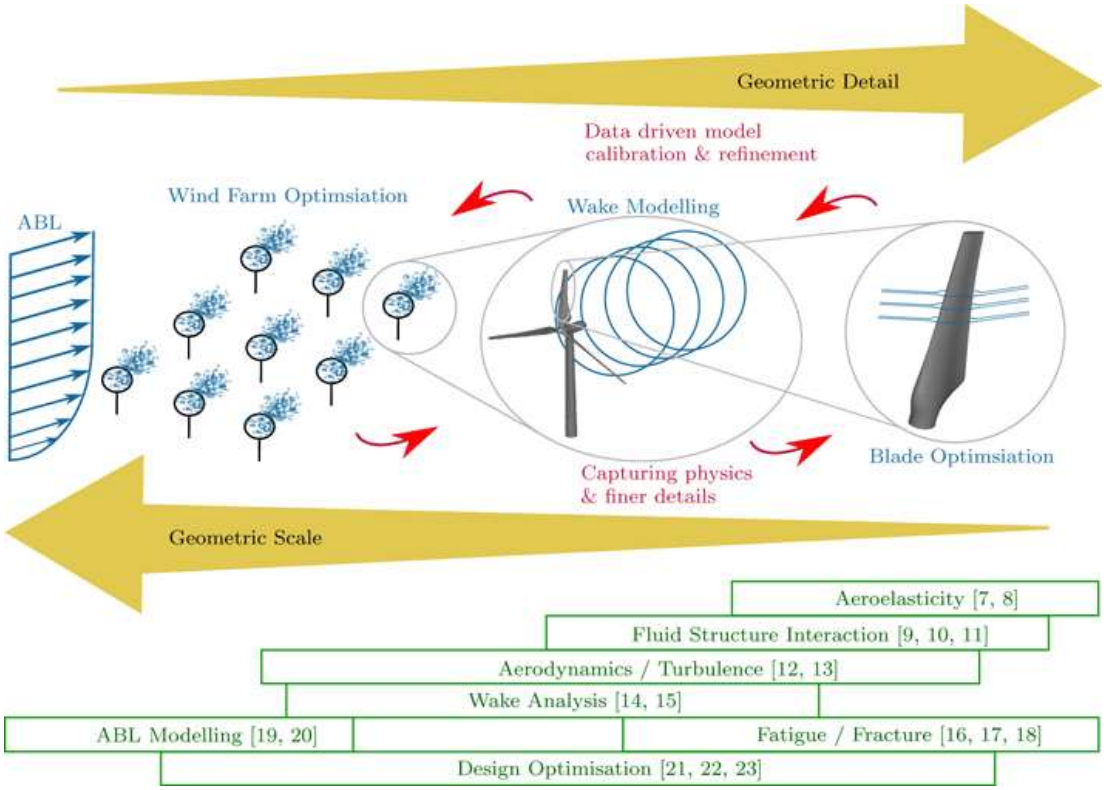

Figure 2.2: Typical wind farm processes and related research activities [6]

2.3 Wind farm dynamics and processes

Wind farms comprise of more than one wind turbine of similar or different specifications and characteristics. It can be thought of as a dynamic system where some processes are occurring spontaneously and/or simultaneously in compliance with the laws of physics. While some of the processes, such as energy production, and varying wind flow regimes, improve wind farm output, others produce undesirable outcomes that affect the overall economics of wind farm. Thus, there are key activities built around these processes (see Figure 2.2) to either improve, avoid, or mitigate their impacts. Subsequent sections and sub-sections will focus on the specific processes, their interactions, and impacts at the scale of a wind farm.

Chapter 3

Atmospheric models

Atmospheric models include the full set of primitive equations which govern atmospheric motions, and its derivatives. Depending on the time scale and resolution, they are applied to either predict the weather or climate.

3.1 Governing equations

This comprises a set of seven equations forming the basic governing equations for other atmospheric models. The seven set of equations are categorized into three momentum equations (momentum transport), a continuity equation (mass transport), a moisture continuity equation (water conservation), a thermodynamic equation (heat transport), and an equation of state (ideal gas law) which relates pressure, volume, and temperature to describe the conditions of atmospheric dynamics. Owing to the multitude of physics involved in atmospheric processes, the primitive (governing) equations are on one hand simplified by ignoring molecular viscosity to ease solution, and on the other hand complimented to capture other significant atmospheric processes such as water formation and transformation, ocean phenomena, or particulate dispersion.

Other atmospheric models derived from the primitive equations use a slightly different combination of the governing equations depending on the location and the purpose of application. Choice of equation sets are informed by location, type of atmospheric processes under study, temporal and spatial scales, and the type of uncertainty to resolve.

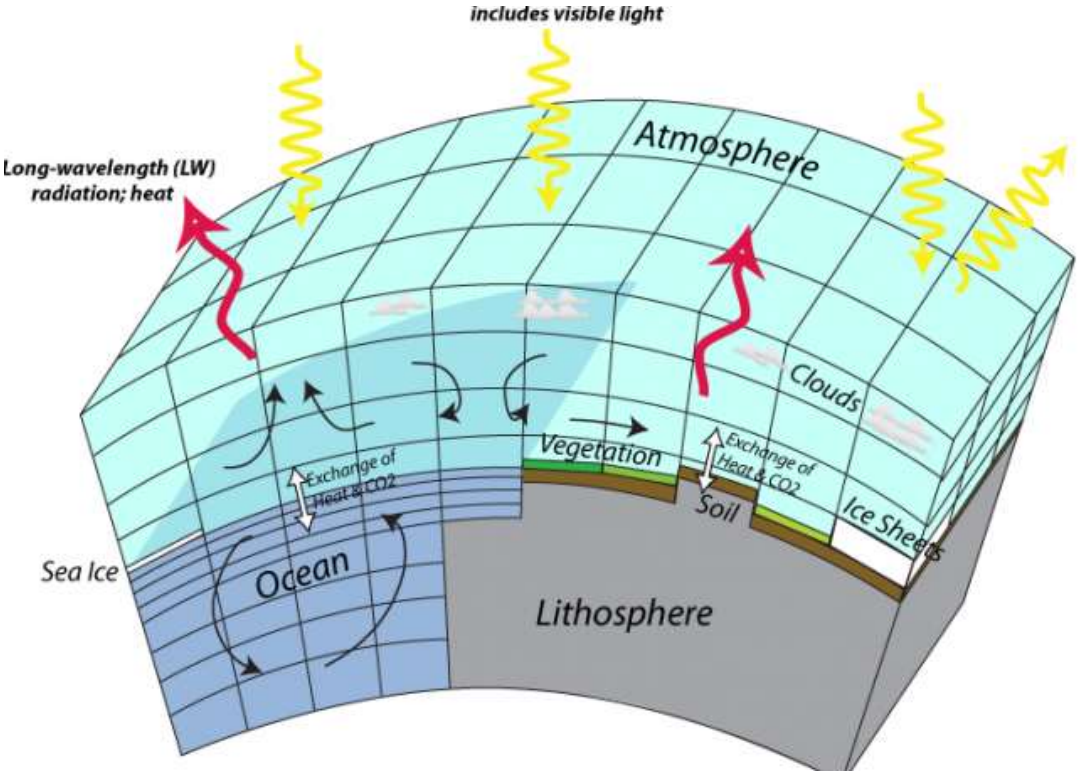

Figure 3.1: A typical representation of a simplified GCM domain [9]

3.2 Global circulation models (GCMs)

GCMs - Global circulation models or General circulation models are regarded as the basis for climate change science and they form important set of tools for understanding weather systems on a global and long term scales [7, 8]. Owing to the large spatial and temporal scales of GCMs, they are not suitable for studying weather behaviour or wind flow on a local scale. So, no evidence is found in literature to show that wind integration studies rely on GCMs for wind resource data. GCMs are characterized by large domain which are discretized by a coarse three-dimensional grid (Figure 3.1). The horizontal grid resolution is usually in the range of 250 to 600 km [9], and therefore not suitable for resolving local features and turbulence at wind farm sites which occur at a much smaller scale and are best studied at higher resolutions.

On the other hand, GCMs have the advantages of global scalability and hence not boundary-conditioned. It is also capable of daily or weekly weather forecast and long-term climate forecasts. According to Hawkins (2012) and Shen et al. (2006), higher resolution GCMs are being deployed driving convergence to inherently higher resolution mesoscale models [7,10,11].

3.3 Mesoscale models

Mesoscale weather models or numerical weather prediction (NWP) models are designed to study weather phenomena and other physical atmospheric processes at a much smaller scale than the synoptic scale GCMs but coarser than microscale [7,12]. Mesoscale models are applied to study weather conditions in the space of a region at a scale of about 20 km to over 200 km horizontal resolution, and within a short temporal scale to predict weather conditions a few days into the future [13,14]. It is not applicable for climate conditions forecasts over decades for instance, but rather performs weather forecasts more accurately. With mesoscale models, physical atmospheric processes such as storm and cloud dynamics, mountains and lake disturbances, and convective phenomena which occur at smaller scales than synoptic within the atmospheric boundary layer (ABL) could be studied [15,16]. Mesoscale model is a generic name for sub-synoptic class of eleven models including The Weather Research and Forecasting (WRF) model which form the basic source of wind speed and direction data used for this study. Other mesoscale models include the UK Met Office Unified Model, Mesoscale Compressible Community (MC2), Eta, SKIRON, The Karlsruhe Atmospheric Mesoscale Model (KAMM), The Fifth-Generation Mesoscale Model (MM5), The Coupled Ocean/Atmosphere Mesoscale Prediction System (COAMPS), The Regional Atmospheric Modelling System (RAMS), The High Resolution Limited Area Model (HIRLAM). In mesoscale models, vertical motions are treated as prognostic variables and therefore non-hydrostatic [7].

WRF model is the most recent mesoscale model developed by the National Center for Atmospheric Research (NCAR) in collaboration with the National Oceanic and Atmospheric Administration (NOAA), the National Centres for Environmental Prediction (NCEP) and the Forecast Systems Laboratory (FSL), the Naval Research Laboratory, the Air Force Weather Agency (AFWA). Oklahoma University, and the Federal Aviation Administration (FAA). The development of the model was conceived in late 1990's and it has a wide range of application in meteorological research and numerical weather prediction at various scales of atmospheric processes from tens of meters to thousands of kilometers [17]. WRF model is designed as a community tool allowing users to make contributions to the improvement in the model physics and parametrization packages. WRF model owes its success stories from being a community tool and having a large collaboration of specialized partners.

The core of WRF model is a complete non-hydrostatic mesoscale model which comprises of two functional parts: advanced data assimilation system which incorporates actual observations

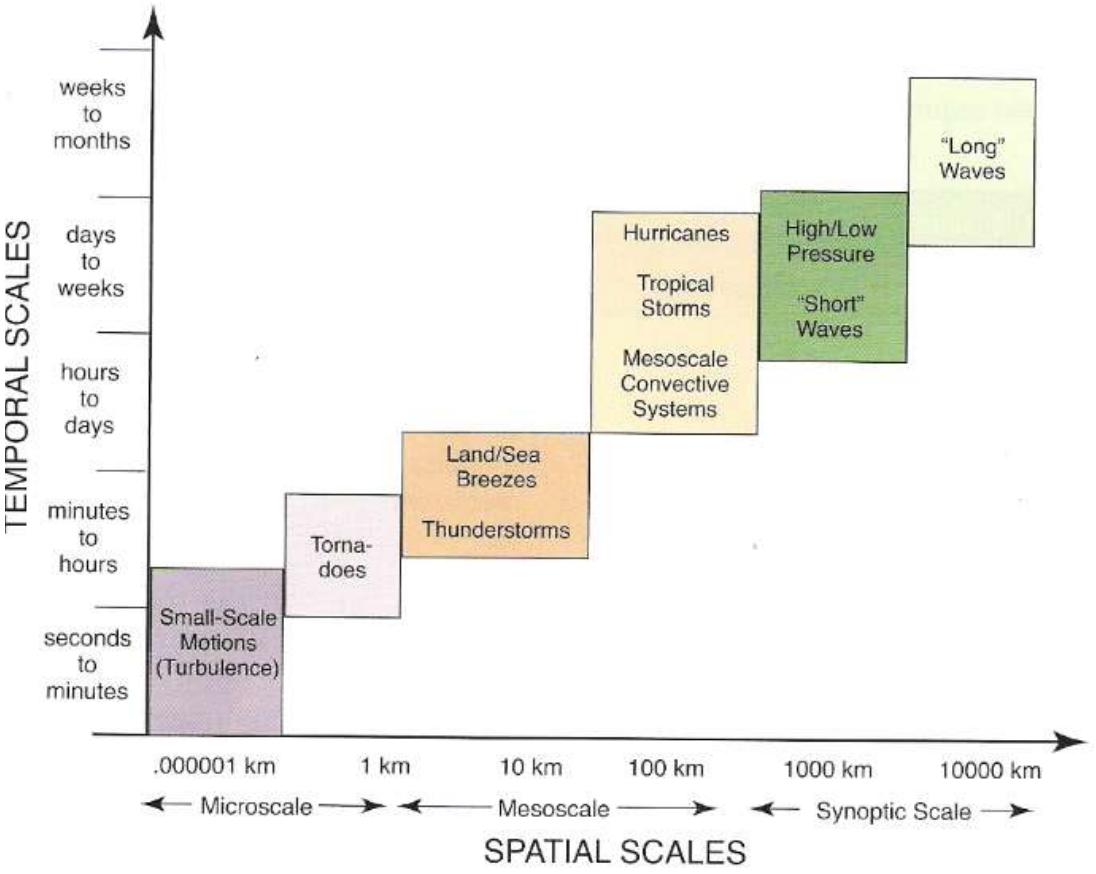

Figure 3.2: Spatio-temporal scales of atmospheric processes [17]

into a gridded model domain of a real system and performs data analysis; and software architecture that handles parallel computing with future growth in mind (extensibility).

In the context of wind energy application, mesoscale models could be applied to map wind resource on a regional scale, and could be coupled with microscale models for micro-siting wind turbine at a specific location of interest. Figure 3.2 shows the atmospheric processes and their classification on time and space scales.

3.4 Microscale models

Microscale models are further steps in increasing the resolution at which atmospheric processes are studied in contrast with macroscale models which give broad or coarse categorization of atmospheric processes. Microscale models provide a more refined scale and detailed revelation

just like the high-resolution effects of a camera. Essentially, they are sets of computational tools which can be classified into linear and non-linear.

3.4.1 Linear models

Linear microscale tools or models evolved from the need to capture the effects of microscale processes with only modest computational resources than the non-linear or CFD approach will normally require. Linear tools approximate steady state and incompressible flow regimes with a set of linear equations for mass and momentum conservation without considering energy conservation. The low-hanging fruits associated with this approach is the ability to run large computational domains at faster speed than CFD. However, linear tools perform poorly with complex terrain because the simplification cannot adequately capture the complex physics of separated flows, and a recirculation bubble developed in the lee of a hilly terrain [17–20].

Both microscale and mesoscale models could be applied as separate approach to understanding same atmospheric systems. The common industry standard for microscale models in literature is the Wind Atlas and Application Program (WAsP), and other linear tools such as WindFarmer etc. could be described as WAsP-like.

3.4.2 Non-linear models

Non-linear microscale models are based on Computational Fluid Dynamics (CFD) which employs computer codes to solve the complete governing equations of fluid flow known as the Navier-Stokes (N-S) equations. Owing to the difficulty in obtaining a complete time varying solution for the overall N-S equations, two simplification approaches: Reynolds averaging and filtering are usually employed to transform the N-S equations. The overall complexity of CFD models depend on the simplification of the governing N-S equations, including the extent of spatial and temporal discretization of the applicable domain, whether the N-S equations are transformed by Reynold averaging or by Large Eddy simulation (filtering) methods to jettison direct simulation of a small-scaled atmospheric process such as turbulence fluctuations, and the method of numerical solution adopted in integrating the N-S equations [7]. The notion of Reynold averaging and large eddy simulation (or filtering) approaches are to minimize computational cost by getting rid of processes that occur at small time and length scales which can only be resolved by expensive computational resources. Both Reynold averaging and LES filtering approaches introduce new unknown terms in the governing N-S equations to

account for the effects of Reynold stress and eddy fluxes attributed to the turbulence fluctuation component of the velocity that are either averaged or filtered [21]. While Reynold averaging requires coupling with turbulence model to give a robust solution, Large eddy simulation (LES) can be applied as an alternative to solve N-S equations numerically but at a higher computational cost. LES involves the solution of the 3D time dependent N-S equations; direct simulation of large eddies; and the handling of smaller turbulence using sub-grid scale model. The limitations of LES is that practical flows with high Reynolds number are computationally expensive to simulate; difficult to specify initial and boundary conditions; and the inherent need to do all simulations in time-dependent three-dimensional domain notwithstanding the stability of the flow or whether it is two-dimensional.

To achieve as much number of equations as there are unknowns (or closure) in Reynold averaged Navier Stokes equations, the additional terms are represented by turbulence models. Common turbulence models include the k-epsilon (k-ε), k-omega (k-Ω), Spalart-Allmaras, and a combination of k-ε/k-Ω models known as the Menter's Shear Stress Transport (SST) turbulence models [22].

In the context of wind energy industry, the strength of microscale CFD models lies in the ability to reveal the details of atmospheric phenomena that occur at small spatio-temporal scale and their cross-interactions or interaction with objects such as turbine rotors, surrounding terrain, etc. Typical CFD models used in this context have fine grid mesh, and the implication is that large computational domains are extremely challenging to simulate. The common approach around this problem is to couple mesoscale and CFD models which have been demonstrated in literature [23–27].

The common turbulence model used is the standard k-epsilon which focuses on the phenomena that give rise to turbulent kinetic energy and its rate of dissipation as relevant in wind energy extraction.

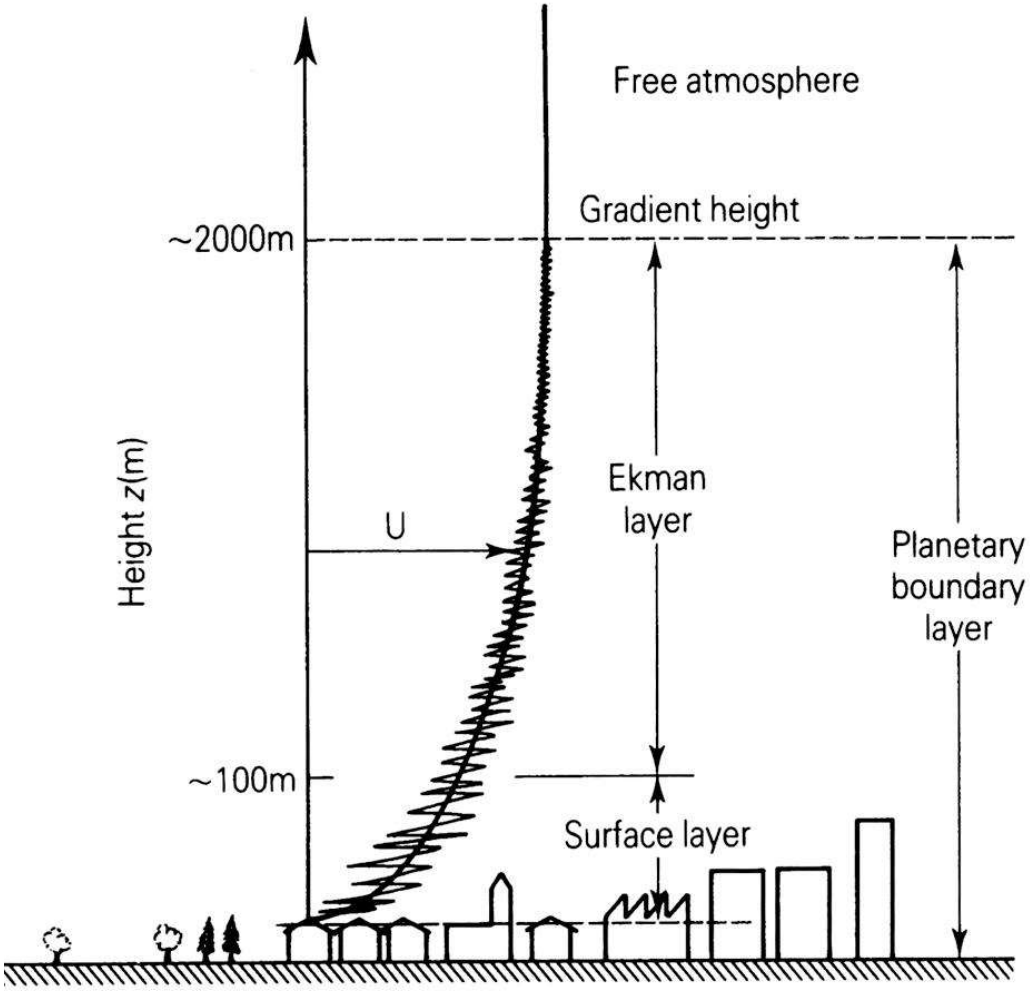

Figure 3.3: Schematic of wind shear over ABL [28]

3.5 Atmospheric boundary layer

The atmospheric boundary layer, also known as the planetary boundary layer is the layer within the lowest atmosphere that is directly influenced by changes in earth's surface conditions within a time scale of at most one hour [27].

The region is characterized by unsteadiness of flow and convective variables including air velocity, moisture, temperature, and vertical turbulence mixing. Temperature inversion and vertical mixing occurs continually at this layer. Because of these interactions, wind flow in ABL is generally weaker than in free atmosphere above ABL. The thickness of ABL is largely determined by the level of surface heating. The more the surface is heated, the thicker the ABL, and vice versa. For instance, the thickness of ABL could be as much as 5km, 1km, and

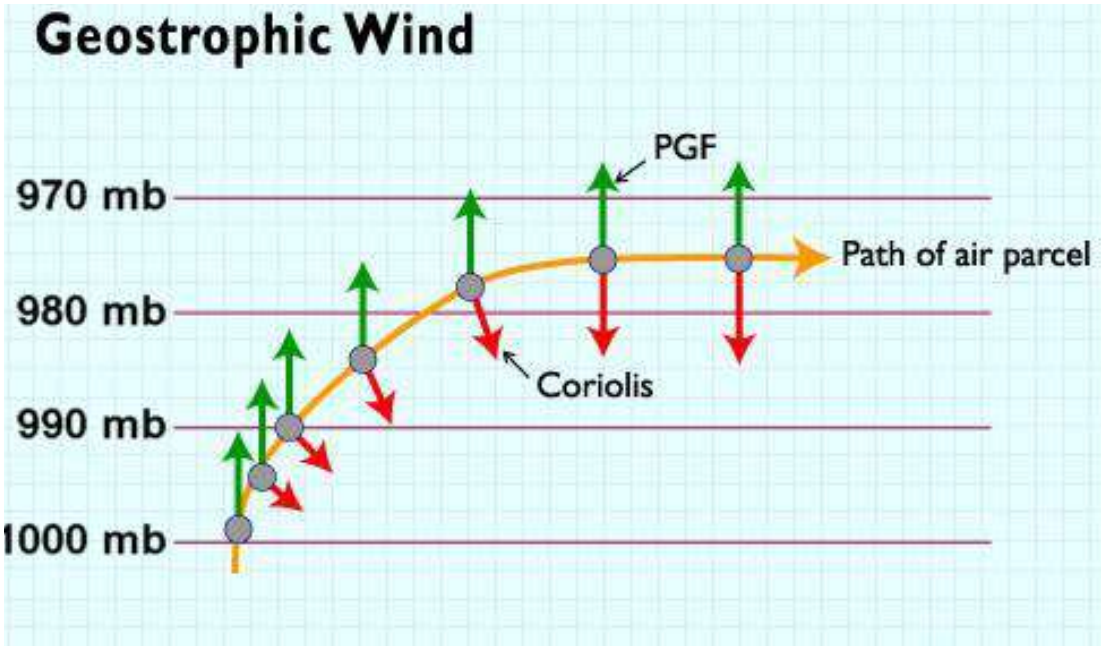

Figure 3.4: Interaction of pressure gradient and Coriolis forces at the ABL [28]

0.5km over desert, urban city or sea surface, and rural locations respectively and could also vary from equator to the poles and over complex terrain. Above the ABL is a free atmosphere where wind flow (known as geostrophic wind) is relatively steady and free from the influence of earth's surface. The geostrophic wind is normally driven by the balance between pressure gradient force and Coriolis force. So, geostrophic wind can be used to evaluate the mean wind speed above the atmospheric boundary layer.

At the surface of the ABL is a no-slip condition which creates mechanical turbulence when wind flows, while the hot air due to solar heating of the ground surface creates convective turbulence [7]. The mechanical and convective turbulence form the defining characteristics of ABL, and distinguish it from the free atmosphere where flow is essentially laminar or transitional. As discussed earlier, unlike in the free atmosphere where turbulence is negligible, the complex turbulence processes at the atmospheric boundary layer cannot be explained nor resolved with mesoscale models. At the ABL, turbulence influences vertical mixing and mean flow, and it is usually simplified through parametrization [29].

The velocity profile of the ABL is usually modelled by a log-law approximation (Equation 3.1), based on the assumption of neutral stability conditions [30], and to simplify computations:

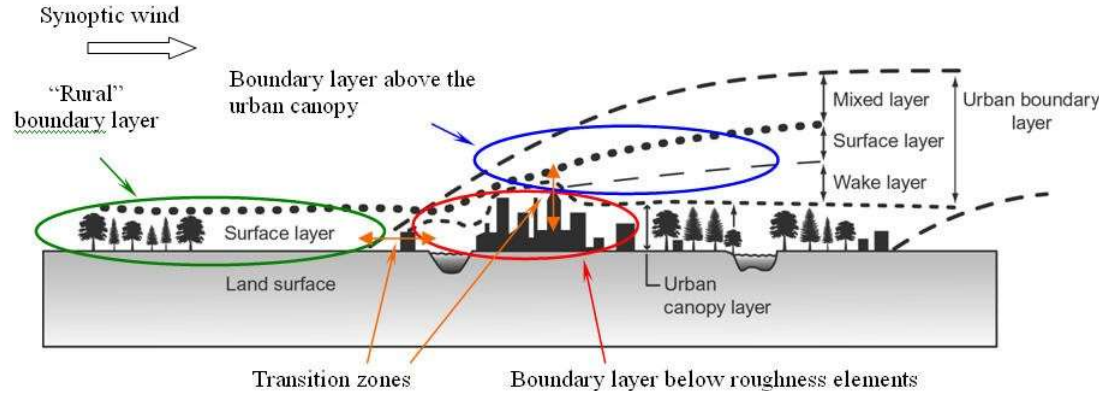

Figure 3.5: Schematic of atmospheric boundary layer over land surface [31, 32]

$$\bar{u}(z) \propto ln\left(\frac{z}{z_0}\right) \tag{3.1}$$

where $\bar{u}(z)$ is the height dependent mean wind speed, z_0 is the terrain roughness length usually 0.001m for rippled sea surface, 0.03m for open farmland with few shrubs, to tens of meters for cities.

In addition to terrain roughness length, the apparent deflection of moving air due to earth's rotation or Coriolis effect could be considered in the ABL model as follows:

$$\bar{u}(z) \propto u^* \frac{ln\left(\frac{z}{z_0} + \Psi\right)}{K} \tag{3.2}$$

The frictional velocity u^* is expressed as $u^* = \sqrt{(\tau_\omega/\rho)}$. Where τ_ω is the shear stress at the wall, $K \approx 0.4$ is von Karman's constant, and Ψ is the stability parameter which is in-turn related to the Coriolis parameter by $\Psi = 34.5fz/u^*$ for a neutral atmosphere, with the Coriolis parameter $f = 2\Omega sin|\lambda|$. Ω is the earth's rotational speed and λ is the latitude.

An alternative equation follows power law approximation expressed as:

$$\bar{u}\,(z) \propto \; z^{\alpha} \tag{3.3}$$

where $\alpha \approx 0.14$ [33] or 0.1-0.25 [34].

Also with a known mean wind speed at hub height u(H) the boundary layer profile can be simply expressed as:

$$\bar{u}\ (z) = \bar{u}\ (H)\left(\frac{z}{H}\right)^{\alpha} \tag{3.4}$$

3.6 Atmospheric stability

Adiabatic lapse rate, the rate of change of air temperature with height in a homogenously mixed and neutral atmosphere, is used as a reference measure for establishing the state of thermal stratification of the ABL. Any deviation from adiabatic lapse rate results in thermal stratification in either unstable, stable, or very stable (inversion) state. The governing equations for stratification frequency N is defined as:

$$N^2 = \alpha.g\left(\frac{dT}{dz} + \Gamma\right) \tag{3.5}$$

For a neutral atmosphere where $\frac{dT}{dz} = -\Gamma$, the stratification frequency vanishes. The thermal expansion coefficient α is variable under high compressibility effects:

$$\alpha = -\frac{1}{\rho}.\left(\frac{d\rho}{dT}\right)|_{constant\ pressure} \tag{3.6}$$

where $\rho = p/RT$ for ideal gas assumption.

Chapter 4

Downscaling of atmospheric models

This chapter is dedicated to summarizing the models introduced in Chapter 3, and the downscaling methodologies including their strengths and weaknesses.

4.1 Downscaling concepts

Many atmospheric models (such as global and mesoscale models) used for climate or weather studies and projections are run at coarse or low resolution in time and space. The implication is that coarse resolution models are unable to resolve important atmospheric processes such as cloud, topography, and turbulence that occur at a local scale and usually smaller than a grid. To surmount this downside, downscaling approaches are employed to obtain weather information and account for small-scaled and short-lived atmospheric and surface processes at a local scale from global or regional scale atmospheric models (Figure 4.1). Downscaling procedure relates the output of coarse resolution models to that of higher resolution models using a dynamical or statistical approach discussed in sections 4.2 and 4.3.

Assessment of local wind conditions by downscaling methods was first published in the studies by Wippermann and Gross (1981) [36]. Heimann (1986) [37] derived a two-dimensional array of wind roses that describes the directional distribution of wind speed on a regional scale. The first study combining downscaling approaches with the output of GCM to study the effects of predicted warming in the seven countries in the Alpine region was first conducted by Frey-Buness et al. (1995) [38]. Furthermore, the method was further refined and its development and application documented [7].

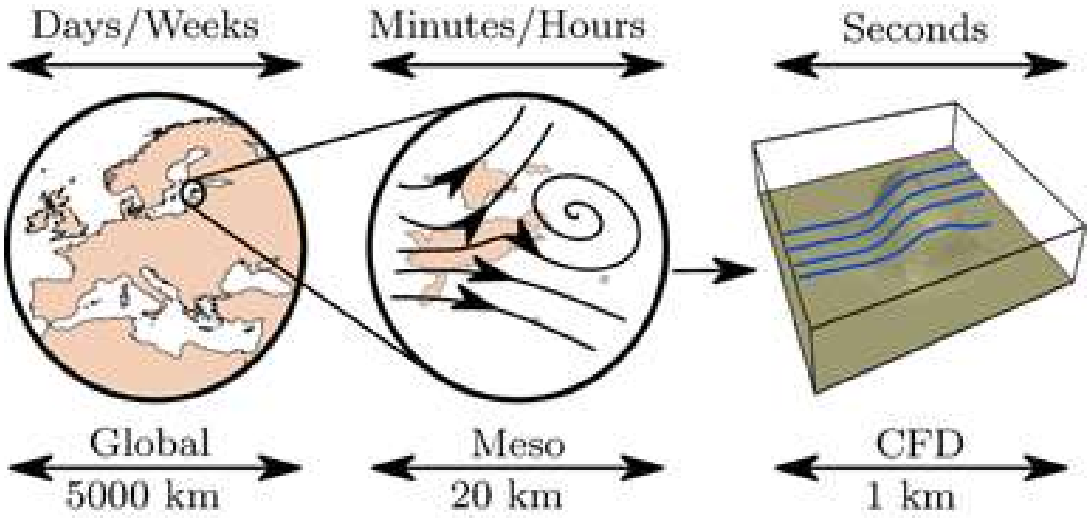

Figure 4.1: Downscaling from global to mesoscale to microscale model [35]

4.2 Dynamical downscaling

In dynamical approach, the output of coarse resolution models is used to simulate local numerical models in higher spatial resolution that is sufficient to capture local atmospheric processes in greater details. This method utilizes a regional climate model (RCM) with higher spatial resolution in the range of 10 to 50 km which feeds on a coarser Global Climate Model (GCM) for boundary condition inputs. Although RCM and GCM are similar in many concepts such as numerical solution method and focus on the physical and dynamical atmospheric processes, they however differ in parameterization due to different resolution. The main advantages of dynamical downscaling include the physical and internal consistency of individual variables in time and space, similar underlying physical principles as a GCM, generates higher resolution and richer datasets for large regions compared to a GCM, no calibration is required [7,35,39–42], and explicitly model changes in atmospheric processes and land cover. The drawbacks include expensive computational resources as high as a GCM, occurrence of artefacts and spurious effects near the boundary of the RCM, presence of RCM biases in output data [43].

4.3 Statistical downscaling

On the other hand, statistical approach establishes empirical relationships between historical variables derived from coarse resolution models and local atmospheric processes such as wind speed. Upon validation, the knowledge of the empirical relationship is then used together with future atmospheric processes from coarse resolution models to predict the corresponding future local processes. In order words, outputs from coarse resolution models are used as predictors to derive variables for local processes such as terrain modified wind speed. Unlike dynamic downscaling approach, statistical downscaling does not require expensive computational resources [40]. In addition, statistical downscaling method has the advantages of flexible choice of statistical methods, and bias correction. The disadvantages include complex calibration, assumption and requirement of stationary statistical relationship in the face of changing climate [39, 40], large amount of inputs such as surface properties, and high frequency details. In addition, it does not present accurate simulation of extreme and convective precipitation, a major concern for tropical regions [39, 43].

Chapter 5

Coupled mesoscale-microscale models

This chapter gives background on previous attempts by some authors in coupling mesoscale and microscale models to simulate local wind climate, particularly for wind energy application.

5.1 Background on coupled mesoscale-microscale models

In practice, microscale-mesoscale model coupling has been used to further downscale models that describe mesoscale processes into microscale models. The motive is to assimilate mesoscale numerical weather prediction data into linear and/or non-linear (CFD) models for wind predictions. This application is largely driven by growth in wind farm development at sites with good wind but complex orography.

Prior to micro-siting, the traditional approach is to obtain long-term wind power resource at the target site. This is usually obtained by launching on-site wind measurement campaigns using meteorological masts with cup anemometers and wind vanes. However, these single point data need to be extrapolated to the points of individual wind turbine to accurately predict site performance. For instance, the met mast for wind resource data collection could be at a height other than turbine hub height, and at locations different from that of individual wind turbines. This necessitates the need to complement the single point met mast climatology with numerical simulations to produce a representative wind flow distribution for the entire site. Traditionally, WAsP-like linear models are used for the prediction using the met mast climatology as input. This approach is common among the bulk of wind farms in operation today.

However, increasing demand for wind turbine deployment has led to exploitation of wind resource at hill crests, mountain tops, and other locations with even more complex orography. Such locations are characterized by rich wind resource but high turbulence that threatens the

life-span of wind turbines. Moreso, the wind flow conditions at these locations involve much more complex physics such as flow separation, terrain interaction, turbulence, wind shear or flow inclination than linear tools could predict accurately. Thus, more sophisticated and nonlinear models in computational fluid dynamics employing Reynold Averaged Navier Stokes (RANS), and large eddy simulation (LES) have gained acceptance in wind energy industry as more robust tools to predict wind resource and the associated flow conditions as discussed in the 2013 edition of EWEA Technology Workshop on Resource Assessment [44]. In addition, concerns about the effects of atmospheric stability or thermal stratification on wind farm outputs draws attention to nonlinear tools which could be tuned to model wind flow under atmospheric boundary layer conditions that may not necessarily be statically neutral but stably stratified. The solution of nonlinear CFD models require specification of boundary and initial conditions which are can be derived from mesoscale model. This forms the basis for coupling mesoscale and microscale models.

Study by Carvalho et al (2013) [45] demonstrates the performance of three different mesoscale-microscale coupling methodologies in predicting wind resources: WRF-WAsP coupling, WRF-WAsP coupling with low resolution terrain data removed, and geostrophic wind extracted above the atmospheric boundary layer where effects of local terrain are negligible. The authors suggest that WRF-WAsP coupling with low resolution terrain data removed gives closer correlation with wind speed measured in-situ [45]. This conclusion suggests that coarse resolution terrain data in mesoscale model has adverse effects on wind resource estimation and therefore direct coupling of mesoscale-microscale models without first screening the mesoscale model of coarse resolution terrain data gives wrong prediction. To assess the performance of WRF and MERRA mesoscale models, Bilal et al (2016) [46] used wind resource data extracted from WRF simulation and MERAA reanalysis data as input to WindSim CFD microscale model. The authors pointed out that the accuracy of microscale modelling results strongly depend on that of mesoscale models which provide the input data and that WRF-WindSim coupled model performed better than MERRA-WindSim [46]. This suggests that WRF-WindSim coupled model could be successfully applied to predict wind flow at wind farm with various degrees of terrain complexity.

Study by Bleeg et al (2015) [47] demonstrates the strengths of coupled models in addressing the challenges with wind resource prediction in complex terrain and suggested that RANS-based model of a stably stratified atmospheric boundary layer could produce reliable wind resource

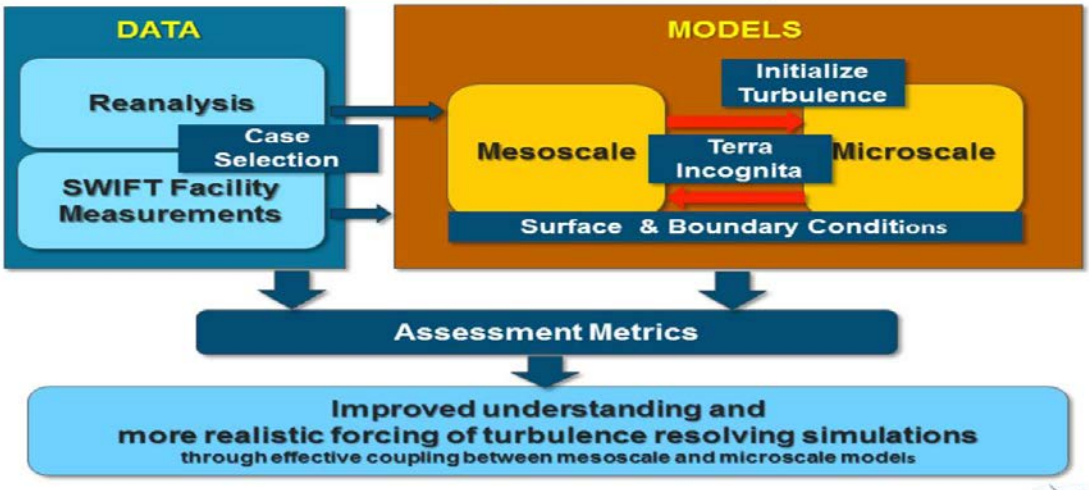

Figure 5.1: Process for coupling mesoscale-microscale models [51]

forecasts.

A caveat in the application of wind speed and wind direction data obtained from hourly-averaged mesoscale is that while they predict long-term variations well, they are poor at shorter-time forecasts. This is because high frequency and sub-hourly variations in wind speed are normally lost whenever mesoscale data is averaged over an hour [7]. In deregulated electricity market, short-term forecasting of wind energy production is strategic in making optimal bids that minimize penalty, optimal use of transmission assets, and managing system frequency. One way to improve the short-term predictability of coupled mesoscale-microscale models is by incorporating machine learning algorithms and categorization approach discussed by Sapronova et al (2016); Sanz Rodrigo et al (2013); and Haque et al (2015) [48–50].

Chapter 6

Wind turbine wake models

In this section, a background study on some wake models are presented including their strengths, weaknesses, and on-going research aimed at improving their wake prediction accuracies. This gives pointers on how the wake models used in WindSim simulation works and their key input requirements.

6.1 Turbine wake and implications

Essentially, wind turbine extracts energy from the mass of air that flows through it leaving some of the air flow properties stripped. The implication of this phenomena is that flow reduces while the turbulence intensity rises at a region behind the turbine rotor. The region where these changes occur is known as the wake of a wind turbine, and the influence exerted by this changes on the overall wind farm performance is known as the wake effects [52, 53]. While turbine wake effects are generally ignored for turbine spacing above 10 rotor diameters, this rule of thumb is however not applicable for large wind farms where many turbines are usually grouped together at shorter distances to optimize land use, cable-related installation costs, and use of limited good wind site. Unlike a small wind farm or single turbine, large wind farms are characterized by a mixture of flow fields experienced by wind turbines operating downstream in the wake of other turbines. At the scale of wind farm, typical wakes losses in the range of 4-15% has been widely reported [54–57], and up to 40% is possible [7].

At farm level, understanding of wake effects is central to wind farm design, layout specifications, and micro-siting decisions. Although, planning permission and landscaping requirements do affect the final layout decision as well. At the level of turbine design, knowledge of wake is key in wind turbine aerodynamics and mitigation of turbine loading.

To accurately predict power production and turbine loading in large wind farms, the effects of turbine wake on wind speed reaching downstream turbines as well as the wake-induced

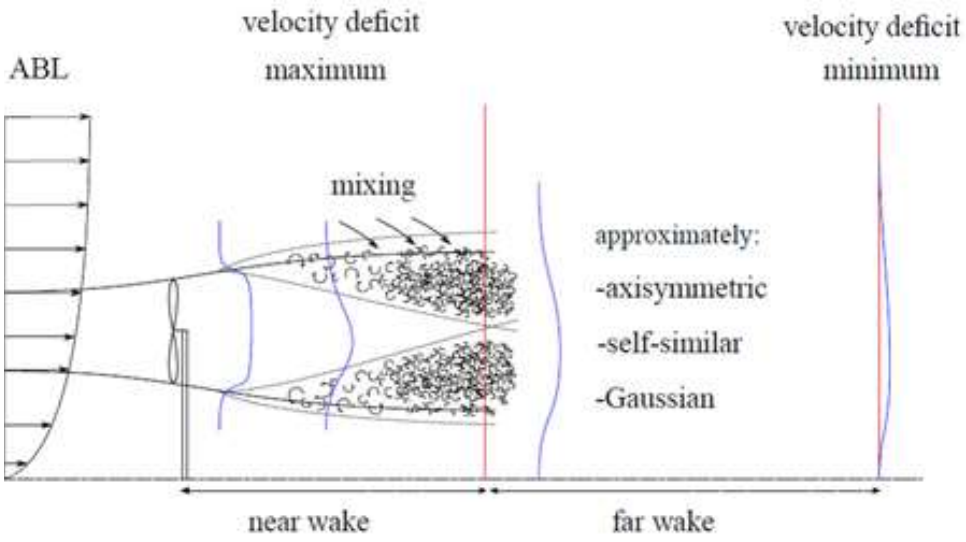

Figure 6.1: Velocity profile in the wake of a wind turbine [30]

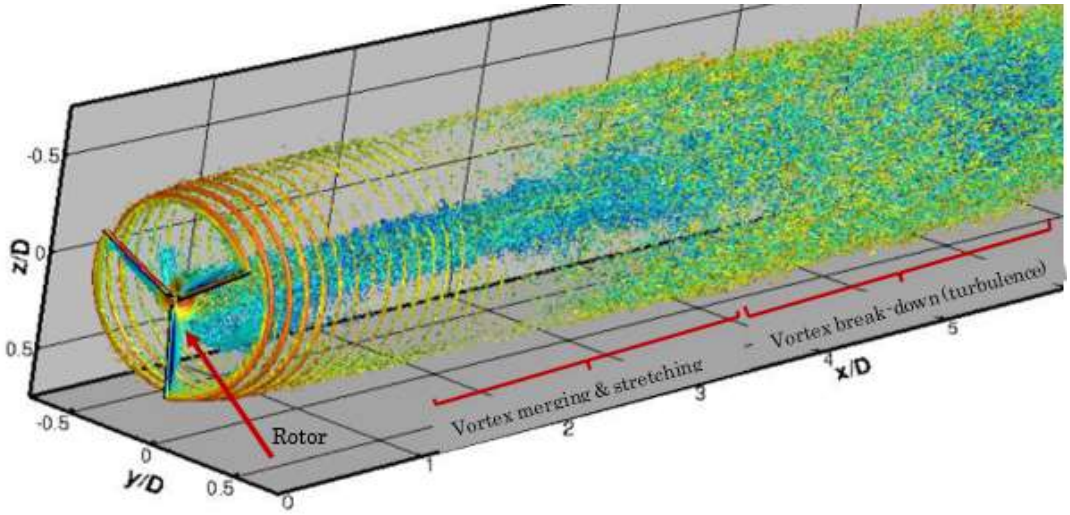

Figure 6.2: 3D turbine wake structure [58]

turbulence on fatigue life of the turbines must be accounted for using wake models. The wake generated by a wind turbine is broadly classified into near wake and far wake. While there is no commonly accepted length definition for the near wake and far wake, near wake is qualitatively defined as the region about one rotor diameter (1D) downstream where the shape of the flow field is defined by turbine geometry as shown in Figure 6.1. Any region of wake outside this zone falls in the category of far wake where wake interference, wake-induced and terrain-induced turbulence mixing are much more important than the rotor geometry. Another attribute of far wake region is that vortices are broken out of the helical structure that originates from the rotor (see Figure 6.2).

Owing to the different characteristics of flow field in the near and far wake (Figure 6.2), distinct modelling approaches have been used in literature as described in the work of Renkema (2007) [52]. Both near wake and far wake phenomena are important for rotor aerodynamics, and both models could be coupled together as discussed by Pirrung et al (2016) [59, 60].

In accounting for wake losses, three approaches have been employed generally. First, a single turbine power curve (regardless of losses) is adopted for the entire wind farm, and the energy estimate is scaled down by a constant wake loss factor from literature, or typically 10% [33]. This approach is quite convenient and the loss factor can be tuned to match historical average of energy output. However, the actual behaviour of wake losses is unevenly distributed across a range of wind speed and therefore a uniform loss factor compromises realistic forecast. Second, an aggregated power curve adjusted for wake losses is determined and employed. Although this approach gives a more realistic account of wake losses across a range of wind speed and over the entire wind farm, there are associated uncertainties in describing a wind farm using a single curve as wake losses are sensitive to wind sector [7, 54].

6.2 Near and far wake models

The near wake behaviour of wind turbines have been studied by some authors [61–63]. The challenges with many wake models in their validation for near wake is that they underestimate the length of near wake phenomena due to inaccurate prediction of turbulence intensity at the rotor tip [64], and hence the wake related energy loss. Near wake is characterized by the interaction of tip, bottom, and span-wise vortices [65], which implies a helical rotational structure and a correlation between tip vortex and near-wake length. This correlation is further confirmed by Sørensen et al (2014) [66] using stability analysis to determine the length of the near wake. The authors found an empirical relationship showing the dependency of near-wake length on thrust, tip speed ratio and the logarithmic of the turbulence intensity [66], and this correlation is lost as the wake progresses further from the rotor [67].

The bulk of the research on near-wake focuses mainly on the nexus between wake, power output, and other physical processes. Where aerofoil data is available, blade element momentum (BEM) approach is often employed for the study of near-wake [67, 68], probably because of the strong influence of wind turbine geometry at this region. On the otherhand, the far-wake studies focus on wake-wake interaction in a clustered wind farm, and the associated reduction

in power output [67]. At this region, the influence of turbine aerodynamics is disregarded and major emphasis is placed on wake evolution, wake interference, and turbulence [67, 69, 70].

The common models that have been used in literature to complement the BEM in describing the near wake include actuator disc models, vortex wake models, and actuator line models. These models differ in accuracies, but they generally help in reducing the computational requirements by not modeling the turbine blades discretely. BEM with actuator disc is the most common and its robustness has been improved over the years to better describe the effects of swirl, and turbine-induced turbulence [64]. However, actuator disk model like some other models still find it difficult to capture the tip vortices neither does it describe the transient flow regime [64]. These shortcomings are ameliorated with actuator line model which extends the disk model and give improved modelling of physical processes underlying the rotor/blade behaviour, including the tip vortices which are seldom captured by other models. However, actuator line model is more computationally expensive because of the resolution of wide range of physical processes, and it is limited to a single point on the turbine surface [64].

To mitigate high computational costs associated with models that capture the underlying physical processes of turbine rotor/blade, other models based on engineering fundamentals are in common use. Typical models that describe wake phenomena are broadly classified into kinematic (or explicit) wake models and field (or implicit) wake models. Kinematic wake models simplify far wake phenomena by considering mass and momentum equations only. On the other hand, field models simulate the mass, momentum, and thermal equations for the entire flow field by solving Reynold's Averaged Navier-Stokes (RANS) equations with turbulence closure using computational fluid dynamics (CFD). The details of these models are presented in Section 6.3 and Section 6.4.

6.3 Engineering (or explicit) models

From the previous discussion in Section 6.2, the complexity inherent in the modelling of the entire physical processes underlying turbine wake led to the development of simplified models using empirical expressions that give engineering estimate of the fundamental parameters of wake evolution, including velocity deficit and turbulence intensity. Some of the engineering models including the Jensen (Park) models are computationally fast, and are intended to model the physics of wake expansion directly without much emphasis on the turbine behaviour such

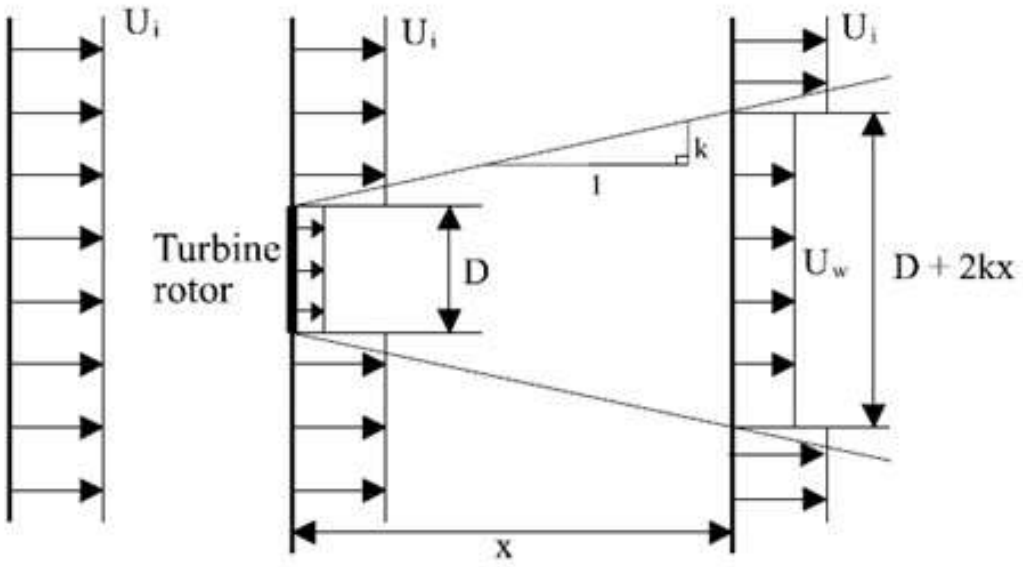

Figure 6.3: Schematic of linear wake expansion (Jensen, 1984; Katic et al., 1986) [71]

as yaw misalignment, partial shadowing, response to variable wind regimes, or interaction with wind field.

6.3.1 Jensen model

The most widely used wake models in wind energy industry since the early 1980s include the Park (N.O Jensen 1986) and modified Park (N.O. Jensen 2005), and Eddy Viscosity model (Ainslie 1988) [70]. The popularity of the Park (N.O. Jensen) also known as Jensen wake models can be attributed to its early development, and as such forms the basis for the development of other wake prediction tools. These group of early wake models have been used as single-turbine wake models to estimate wake between two turbines-with one of the turbines in the wake of another. Jensen model has been found to be a user friendly kinematic wake model, and it describes wake in terms of the velocity deficit, wake decay factor, rotor diameter, and thrust coefficient. The model assumes a linearly expanding wake (analogous to a negative jet) with a starting diameter equal to the rotor's and depends on the downwind distance X usually expressed in rotor diameters (see Figure 6.3). The model also assumes an optimal rotor with induction factor, a = 1/3. Based on these assumptions and the principle of mass conservation, N.O. Jensen derived an explicit expression for asymptotic wind speed.

The parameters in Figure 6.3 are related as follows:

$$X = s.D \tag{6.1}$$

$$D_w = D + 2k.X \tag{6.2}$$

$$\frac{D_w}{D} = 1 + 2.k.s \tag{6.3}$$

$$\frac{U}{U_0} = 1 - \frac{1 - \sqrt{1 - C_T}}{(1 + 2.k.s)^2} \tag{6.4}$$

where U is the downwind velocity; U_0 is the up-stream wind velocity; C_T is the thrust coefficient for wind turbine; s is the normalized separation distance (=X/D); D is the rotor diameter; D_w is the wake diameter; k is the wake decay constant, usually 0.075m and 0.04m are recommended for onshore and offshore wind farms respectively [72]. The higher the value of k, the higher the turbulence, the quicker the wake decay, and the faster the wake expansion.

Where information on site-specific roughness (z_0) is available, decay constant (k) can be estimated more accurately in terms of hub height (H) or ambient turbulence (I_a) as follows [73]:

$$k = \frac{1}{2.ln(\frac{H}{z_0})} \tag{6.5}$$

$$I_a = \frac{1}{ln(\frac{H}{z_0})} \tag{6.6}$$

$$k = \frac{1}{2} I_a \tag{6.7}$$

Equation 6.7 shows the relationship between the decay factor and the turbulence intensity which is in-turn related to atmospheric stability. Common wind farm design tools such as WAsP, WindFarmer and WindPRO can be used to determine the typical single wake flow field predicted by Jensen model (Figure 6.4):

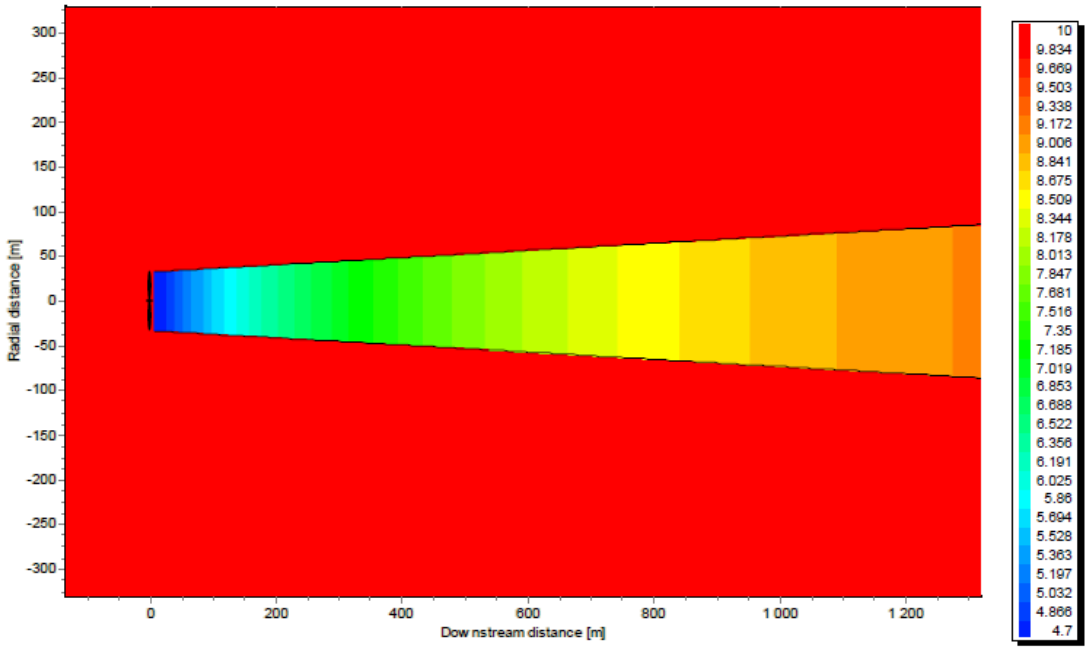

Figure 6.4: Schematic of single wake flow field based on Jensen model [73]

The main drawback with Jensen wake model is the inability to describe near-wake. This is expected because Jensen model was derived based on turbine geometry. However, some studies have been conducted to improve the robustness of Jensen (Park) wake models [70].

6.3.2 Larsen model

The Larsen model is a single wake model developed in 1988 at the Risø DTU National Laboratory by G.C. Larsen. It employs Prandtl turbulent boundary layer equations and Prandtl's mixing length theory to estimate wind flow at the instance of wake and to evaluate the Reynolds stresses in a cylindrical coordinate form [74, 75]. The underlying equations are solved for closed-form solutions of wake width by assuming a self-similar velocity profile, incompressible and stationary flow, and negligible wind shear which implies axisymmetric flow [52]. The Larsen model has been used in the European Wind Turbine Standard II as a reference wake model to determine wind turbine loading due to wake effects [74].

Based on first order approximation, the axial velocity deficit and wake radius are defined:

$$(\Delta U)_1(X,r) = -\frac{U_\infty}{9}\left(C_T A(X_0+X)^{-2}\right)^{\frac{1}{3}}\left[r^{\frac{3}{2}}.\left(3c_1^2 C_T A(X_0+X)\right)^{-\frac{1}{2}} - \left(\frac{35}{2\pi}\right)^{\frac{3}{10}}\left(3c_1^2\right)^{-\frac{1}{5}}\right]^2 \quad (6.8)$$

$$R_w(X) = \left(\frac{35}{2\pi}\right)^{\frac{1}{5}} \left(3c_1^2\right)^{\frac{1}{5}} \left(C_T A (X_0 + X)^{-2}\right)^{\frac{1}{3}} \tag{6.9}$$

where ΔU is the axial velocity deficit; U_∞ is the free-stream (undisturbed) velocity; C_T is the thrust coefficient for wind turbine; A is the swept area; X is the turbine separation distance downwind; and the two unknown constants X_0 and c_1 represent a parameter that relates rotor diameter to rotor position and a parameter related to Prandtl mixing length respectively. The expression for X_0 is as specified in the EWTS II [52], while that of c_1 is as corrected in Larsen [52, 76].

$$X_0 = \frac{9.5D}{\left(\frac{2.R_{9.5}}{D_{eff}}\right)^3 - 1} \tag{6.10}$$

$$c_1 = \left(\frac{D_{eff}}{2}\right)^{\frac{1}{5}} \left(\frac{105}{2.\pi}\right)^{-\frac{1}{2}} \left(C_T A X_0\right)^{-\frac{5}{6}} \tag{6.11}$$

where D is the rotor diameter; D_{eff}, and $R_{9.5}$ are the effective rotor diameter, and wake radius at 9.5 rotor diameters (9.5D) downwind expressed as follows:

$$D_{eff} = D\sqrt{\frac{1 + \sqrt{1 - C_T}}{2\sqrt{1 - C_T}}} \tag{6.12}$$

$$R_{9.5} = 0.5\Big[R_{nb} + min(H, R_{nb})\Big] \tag{6.13}$$

where H is the hub height, and R_{nb} is the wake radius in rotor diameters accounting for blockage effect, and expressed empirically as:

$$R_{nb} = max\Big[1.08D, 1.08D + 2.17D(I_a - 0.05)\Big] \tag{6.14}$$

where I_a is the ambient turbulence intensity. Equation 6.13 fixes the wake radius should it exceeds the hub height.

A typical behaviour of the axial velocity deficit in downwind direction based on Larsen model is shown in Figure 6.5.

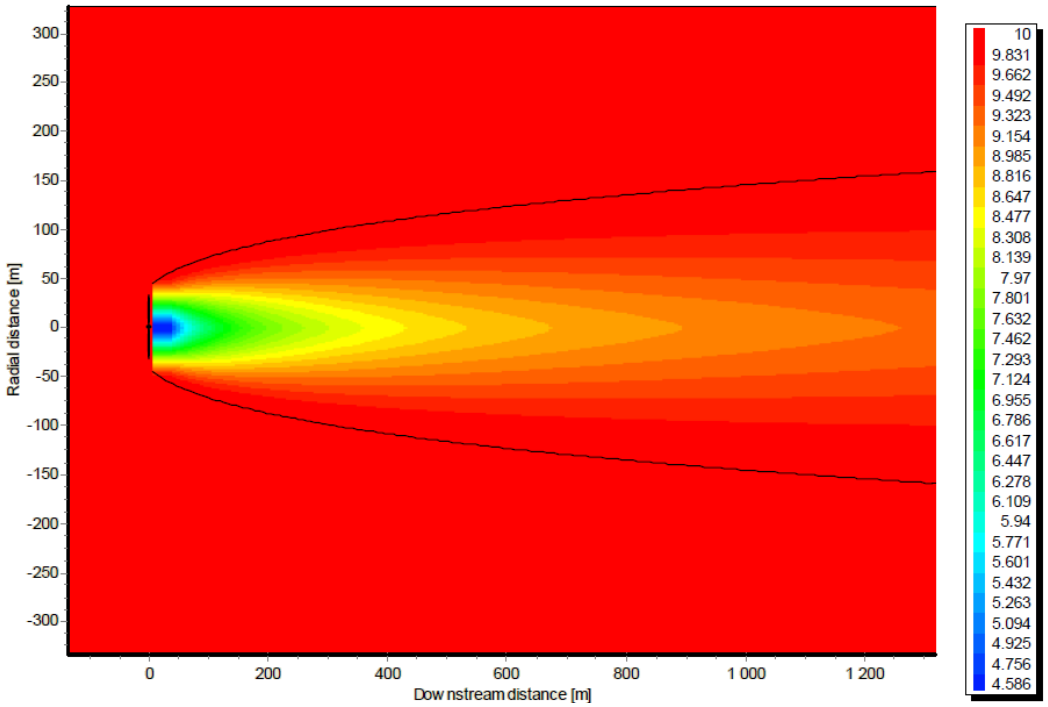

Figure 6.5: Schematic of single wake flow field based on Larsen model [73]

Larsen model has been extensively reviewed and validated for wind farms located in complex terrain by several authors [52, 53, 69, 75–77]. Most of these studies adjudge Larsen model as suitable for far wake rather than near wake. It is included in some commercial and open-source wind design and optimisation tools including WindSim [52], WindPRO [78], and WAsP [79].

6.3.3 Frandsen model

The Frandsen wake model is a more recently developed wake model presented in 2006, and it a reference model to determine effective turbulence intensity for use in wake-induced load calculations as stipulated by the IEC 61400-1 standard [74, 80]. Unlike the Jensen and Larsen models, the Frandsen model which is adopted in the Storpark Analytical Model (SAM) is not intended for single turbine wake but large offshore wind farms. The studies by Charhouni et al. (2016) [81], Frandsen et al. (2004) [82], and Timmers (2017) [73] give detailed accounts of the Frandsen wake model.

In the application of Frandsen for wake prediction, linear rows of equally-spaced wind turbines are placed on rectangular domain representing the site. Then a control volume with cylindrical geometry and constant cross-sectional that matches the wake diameter. The parameters describing the wake are modelled as follows:

$$U_{wake} = \frac{U_\infty}{2}\left(1 \pm \sqrt{1 - 2\frac{A}{A_w}C_T}\right) \tag{6.15}$$

$$D_{wake} = D\Big(\beta + 0.7s\Big) \tag{6.16}$$

$$\beta = \left(\frac{D_{eff}}{D}\right)^2 = \frac{1 + \sqrt{1 - C_T}}{2.\sqrt{1 - C_T}} \tag{6.17}$$

$$a = 1 - \left(\frac{U_r}{U_\infty}\right) \tag{6.18}$$

where U_{wake} is the single wake velocity; D_{wake} is the wake diameter; β is the wake expansion parameter; A is the swept area; A_w is the wake cross-sectional area; U_r is the wind velocity at the rotor; a is the induction factor which determines the sign convention in Equation 6.15 as follows:

$$\pm = \begin{cases} +, & \text{if } a \leq 0.5 \\ -, & \text{if } a > 0.5 \end{cases} \tag{6.19}$$

The validation for offshore application, the purpose of which it was designed, has been studied by Tian et al., (2015) [84] and Tong et al., (2012) [83]. However, Frandsen model is not commonly used probably because of smaller scale of offshore wind farm deployment compared to onshore.

6.3.4 Ishihara model

The engineering wake model of Ishihara et al. was developed based on the data derived from wind tunnel experiment for a Mitsubishi-type wind turbine scaled to 1:100 [85, 86]. Central to the development of this model is the need for a simple, fast and yet robust model that suit both onshore and offshore applications. Unlike other analytical models, Ishihara considers non-constant rate of wake recovery and its dependence on turbulence due to mechanical (rotor) and/or atmospheric (buoyancy) forcings. Similarly, Ishihara model also demonstrates the dependence of wake recovery rate on the turbine's thrust coefficient-the larger the thrust coefficient and/or the turbulence, the quicker the rate of wake recovery. However,

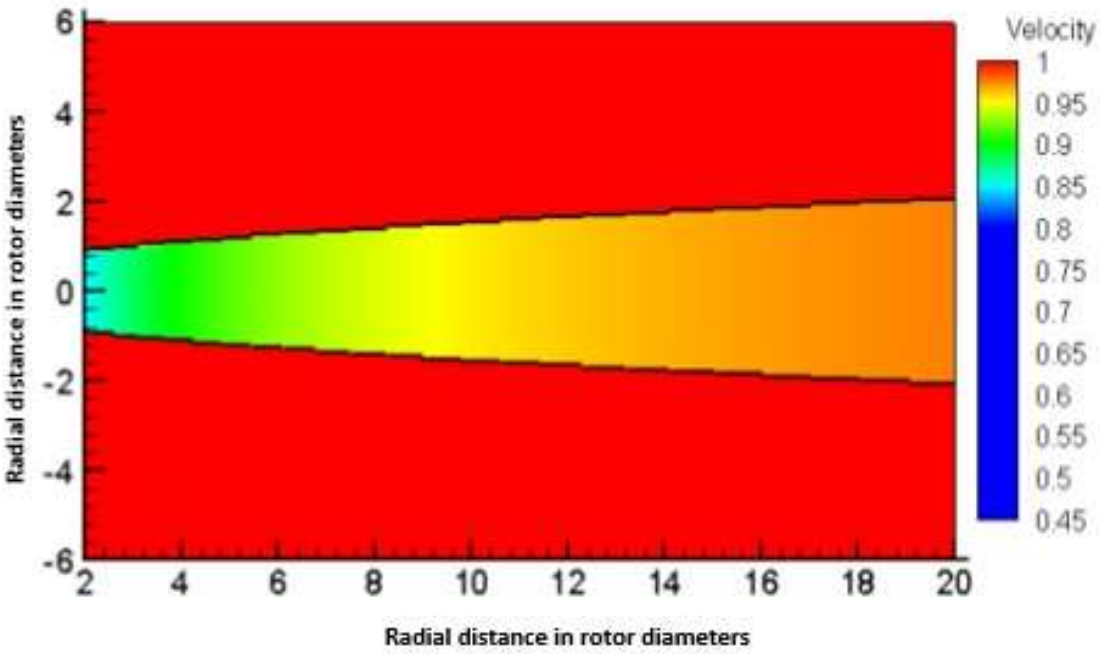

Figure 6.6: Schematic of single wake flow field based on Frandsen model [83]

the dependence differs in both onshore and off-shore environment. In offshore wind farms where ambient turbulence is generally weak, turbine-induced turbulence is more significant. In onshore sites, especially with complex terrain, both turbulence components have significant effects on the rate of wake recovery.

In Ishihara model, the maximum normalized velocity deficit occurring at the center of the wake is a function of thrust coefficient and assumed to follow a Gaussian profile given by:

$$\frac{\Delta U}{D_\infty} = \frac{\sqrt{C_T}}{32}\left(\frac{1.666}{k_1}\right)\left(\frac{x}{D}\right)^{-p} \exp\left(-\frac{r^2}{D_w^2}\right) \tag{6.20}$$

The wake growth or diameter is modelled as:

$$D_w = \frac{k_1 C_{Tj}^{\frac{1}{4}}}{0.883} D^{1-\frac{p}{2}}.x^{\frac{p}{2}} + D \tag{6.21}$$

The parameter p is the combined turbulence intensity given as [85]:

$$p = k_2\left(I_a + I_w\right) \tag{6.22}$$

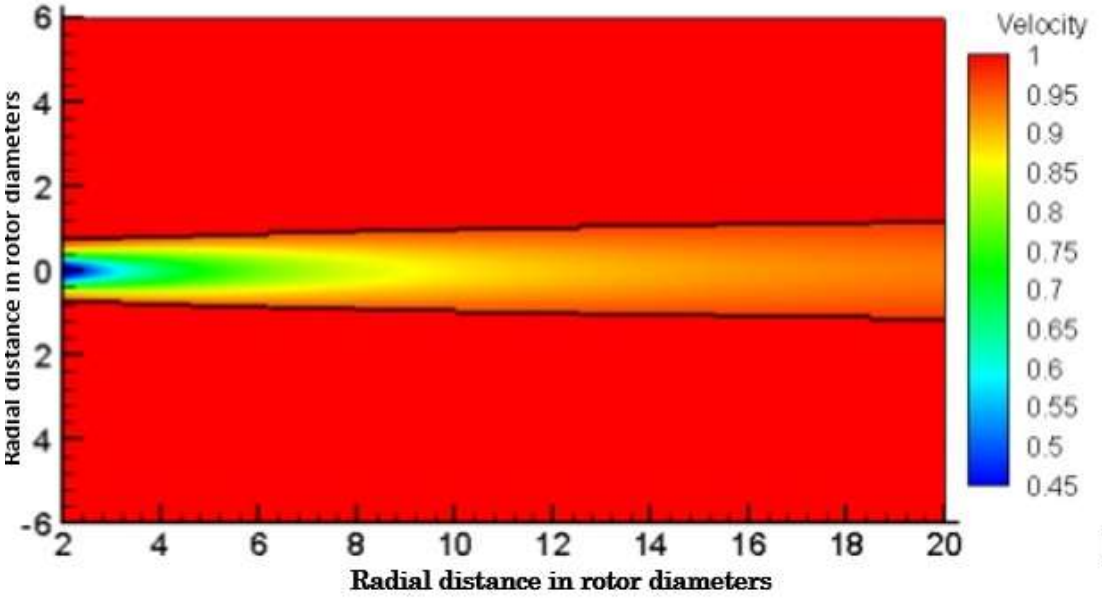

Figure 6.7: Schematic of single wake flow field based on Ishihara model [83]

where I_a is the ambient turbulence, and I_w is the turbine-induced turbulence given by:

$$I_w = \frac{k_3 C_T}{max(I_a, 0.03)}\left(1 - \exp\left[-4\left(\frac{x}{10D}\right)^2\right]\right) \tag{6.23}$$

where k_1, k_2,& k_3 are constants determined experimentally as 0.27, 6.0 & 0.004 respectively [85].

Like Jensen and Larsen models, Ishihara model is also featured in WindSim simulator and it has been used in some validation studies for wind flow in complex terrain [53, 83].

6.4 Field (or implicit) models

The field models present a more detailed description and simulation of the wind flow field. They employ a complete or simplified computational fluid dynamics (CFD) approach either in two- or three-dimensional domain to solve a set of Reynold Averaged Navier-Stokes equation. Field models also includes the use of Large Eddy Simulation (LES) approach. The implication of CFD and LES approaches is that high computational resources is required and slow speed is inevitable. CFD approach is considered to have moderate computational cost compared to more advanced LES based models. However, this cost margin comes with some trade-offs in accuracy-LES gives higher accuracy.

The specific wake models in this category include the Ainslie wake model which uses a parabolic equivalent of RANS known as the thin shear layer approximation together with the continuity equation and field model to determine a full flow field [83]. Some of the commercial wake models, including Fuga and Ellipsys3D are adaptable to both RANS and LES simulation approach depending on the required levels of sophistication and available computational power.

In the Ainslie wake model, the key assumptions include axisymmetric wake (i.e. allows for an equivalent model in 2D cylindrical coordinates); incompressible flow; negligible external forces or pressure gradients; negligible viscous terms, and negligible standard deviation of velocity gradients [87–89]. The velocity deficit is expressed as:

$$\Delta U_i = \frac{1}{U_\infty}\left[\frac{1-U}{exp\left(-3.56\left(\frac{r}{D_w}\right)^2\right)}\right] \tag{6.24}$$

$$D_w = \sqrt{\frac{3.56C_T}{8\Delta U_i(1-0.5\Delta U_i)}} \tag{6.25}$$

where r is the radial distance from centre line of the turbine; U_i is the initial velocity deficit expressed as:

$$\Delta U_i = C_T - 0.05 - \left(16C_T - 0.5\right)\frac{I_a}{10} \tag{6.26}$$

The solution furnishes a wake flow field with Gaussian structure (Figure 6.8).

The implications of some of the foregoing assumptions are that Ainslie model does not fit well in the region, especially at a short distance of below 2 rotor diameters downwind, where the pressure gradients are not negligible. However, Ainslie presents a more realistic flow field with conspicuous layers of wake regions such as vortex merging and stretching, and vortex break-down (due to turbulence) relative to the features in the Figure 6.2.

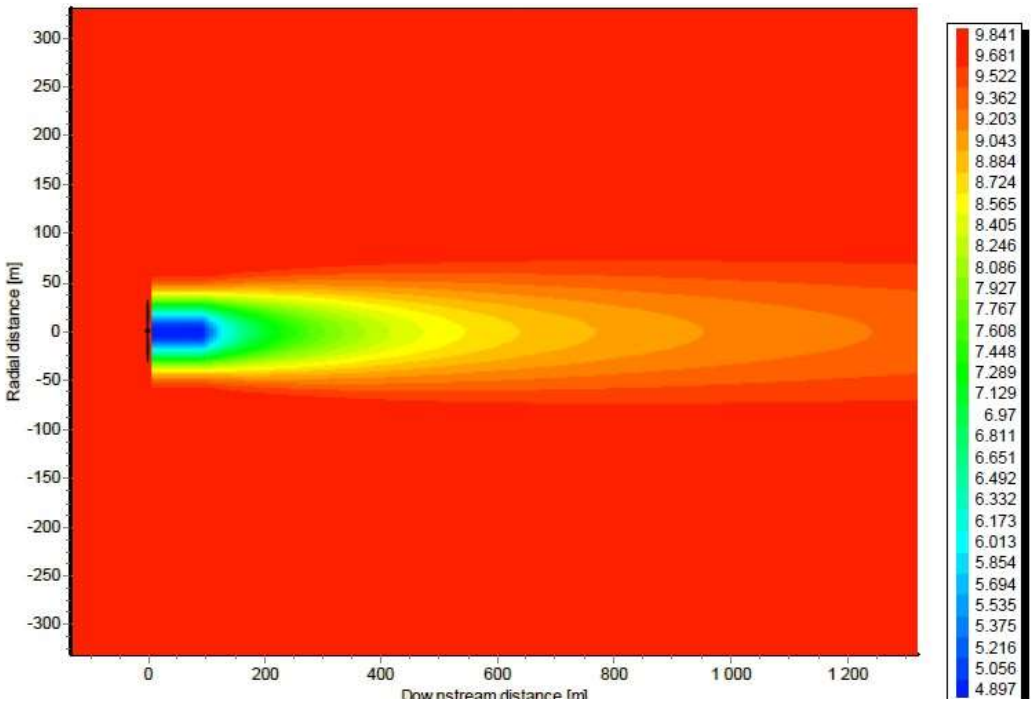

Figure 6.8: Schematic of single wake flow field based on Ainslie model [73]

Chapter 7

Digital terrain modelling

The general concept of digital terrain modelling and where it fits in wind energy integration is summarized in this section. Also, the various approach and key sources of data for digital terrain modelling (DTM) are highlighted.

7.1 Digital terrain modelling(DTM) concepts

Wind flow is influenced by topographic features such as surface roughness and elevation. Therefore, the understanding of the topography by means of digital terrain modelling help to quantify the scale of the phenomena related to topography. Digital terrain modelling may be referred to as a digital mapping of a specific site on the earth's surface. It provides a topographic model of the bare earth/underlying terrain of the earth's surface, and represents the topography in the form of a triangulation network (Figure 7.1). It is also mentioned as important requirements in wind farm planning and design, environmental impact studies, and micro-siting [90–93].

Currently, DTMs are derived from three main sources: ground surveys (borehole records or seismic surveys), photogrammetric data capture (manual or automatic), or digitized cartographic databases [90]. Other seldom used approaches to generating DTMs include radar or laser altimetry, and sonar (for underwater terrain). Details of various data sources and DTM approaches are described in [91, 92]. Other secondary sources from which DTMs have been derived in literature include the Environment Agency, Ordinance Survey Panorama DTM Data, and Global Mapper which feed on the primary databases.

DTM is a 3D model of the topography, and it gives information on the distribution of terrain elevation over the cross-section of the terrain. DTM is a useful basis for defining Zone of Theoretical Visibility Maps, within which there may be a line of sight and not necessarily

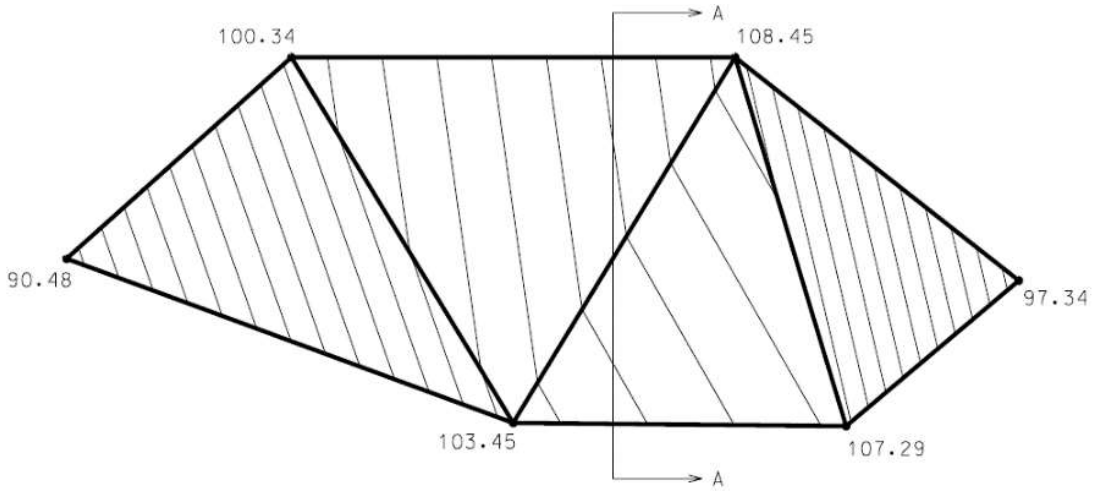

Figure 7.1: Schematic triangulation network for digital terrain modelling [91]

visible proposal due to localized screening effects not captured by the DTM. Production of ZTV is one of the first step in LVIA, helping to inform the selection of study area in which impacts will be considered in more details. ZTV provides such details as: from where wind turbines are most likely to be visible; how many wind turbines are likely to be visible; a means of identifying the extent and pattern of theoretical visibility [93]. DTM also helps in assessment of terrain slope and potential pit locations, and to assess the potential influence of the wind farm development on the wider landscape and visual impacts; also for peat stability and ground assessment in combination with site survey and river information.

7.2 Wind flow over complex terrain

Generally, wind turbine wake characteristics and wind flow field are accelerated when passing over earth's surface with complex terrain features [94]. However, the terrain speedup effect on wake evolution is sometimes neglected or not adequately accounted for. Growth in large wind farm deployment over the years has led to exploration of hilly and remote sites, thereby necessitating the need to account for the impacts of complex terrain both on the energy yield and the loading of wind turbines which become significant, particularly where katabatic wind regime is present due to differential solar heating of different elevation of earth's surface.

Literature has shown that in complex terrain greater than 17° inclination, most wake models fail to predict accurately. Attempts to solve this challenge has led to the introduction of a more complex physics and tools to determine a more realistic wind flow field by solving the

resulting non-linear systems of equations. It has also been established that computational fluid dynamics approach gives a more reliable result [94, 95].

To include effects of terrain, a wind farm modelling tool including WindSim allows for inclusion of site-specific digital terrain model in the simulation, and many studies have been conducted to validate the application of the tool for complex terrain wind farms [96]. Also, the challenges presented by non-availability of on-site wind dataset for most locations where wind farms are desirable means that a tool is needed to take advantage of available wind data set based on forecast from mesoscale models, such as WRF which ought to be downscaled prior to use for local sites. Interestingly, WindSim has the functionalities allowing for downscaling of mesoscale wind dataset and it has been coupled with mesoscale models to study local wind flow conditions [97–100].

Chapter 8

RANS equation and turbulence models

This section gives background on the Reynolds averaged Navier-Stokes equation that forms the governing equation of fluid flow used in WindSim simulation. Also, various turbulence closure schemes used in literature to resolve the RANS equation are discussed in details, and the boundary conditions types relative to WindSim simulation. The connection between the turbulence closure schemes and atmospheric stability is also highlighted.

8.1 Reynolds Averaged Navier-Stokes equations

Generally, Reynolds averaging is an approach usually carried out in fluid dynamics to filter out turbulent fluctuation components from the mean flow velocity by time averaging of the original variable. Given the time-dependent original flow variable $\Phi(t)$ which could be velocity for instance, the variable can be subjected to an averaging procedure over a time T which is enough to filter the fluctuations in $\Phi(t)$.

Essentially, the original variable $\Phi(t)$ is decomposed into a fluctuating and average terms as shown below:

$$\bar{\Phi} \equiv \frac{1}{T}\int_T \Phi(t)\,dt \equiv \Phi - \Phi' \tag{8.1}$$

In wind energy application, the mesoscale and microscale wind field can be described by the steady state incompressible Reynolds averaged Navier-Stokes (RANS) and continuity equations given below:

$$\rho\frac{\partial U_i}{\partial x_i} = 0 \tag{8.2}$$

$$U_j\frac{\partial U_i}{\partial x_j} = -\frac{1}{\rho}\frac{\partial P}{\partial x_i} + \frac{\partial}{\partial x_j}\left(v\left(\frac{\partial U_i}{\partial x_j} + \frac{\partial U_j}{\partial x_i}\right) - \overline{u_i u_j}\right) \tag{8.3}$$

where i = x, y, or z, U_i and U_j are the mean velocity components that arise from the decomposition of velocity variables into mean and fluctuating (turbulent) components, ρ is the density, v is the dynamic viscosity, P is the pressure, and $\overline{u_i u_j}$ is the Reynolds stresses arising from the Reynolds averaging of the continuity and Navier-Stokes equations.

The Reynolds stress term is non-linear and must be modelled to close the set of RANS equations for solution. In attempts to model the Reynolds stress term, different turbulence models have been proposed in literature as described by Karthik (2011) [101].

8.2 Turbulence models and closure schemes

The set of Equation 8.2 and Equation 8.3 are not sufficient to determine the unknown variables U_i, U_j, and P. Therefore, turbulent closure is introduced by relating the turbulent Reynolds stresses term $\overline{u_i u_j}$ to the mean of velocity terms U_i, U_j, using the turbulent viscosity v_T.

$$\overline{u_i u_j} = -v_T \left(\frac{\partial U_i}{\partial x_j} + \frac{\partial U_j}{\partial x_i} \right) + \frac{2}{3} \delta_{ij} k \tag{8.4}$$

where δ_{ij} is the Kronecker delta, a piecewise function of variables i and j such that:

$$\delta_{ij} = \begin{cases} 1, & \text{if } i = j \\ 0, & \text{if } i \neq j \end{cases} \tag{8.5}$$

Furthermore, the turbulent kinetic energy k and its dissipation rate ε are related to the turbulent (eddy) kinematic viscosity v_T using any of the k-ε turbulence models [101], a family of two equation eddy viscosity models suitable for flows at high Reynolds numbers.

$$v_T = c_\mu \frac{k^2}{\varepsilon} \tag{8.6}$$

$$\frac{\partial}{\partial x_i} \left(\rho U_i k \right) = \frac{\partial}{\partial x_i} \left(\rho \frac{v_T}{\sigma_k} \frac{\partial k}{\partial x_i} \right) + \rho . (P_k - \varepsilon) \tag{8.7}$$

$$\frac{\partial}{\partial x_i} \left(\rho U_i \varepsilon \right) = \frac{\partial}{\partial x_i} \left(\rho \frac{v_T}{\sigma_\varepsilon} \frac{\partial \varepsilon}{\partial x_i} \right) + \rho . \frac{\varepsilon}{k} (C_{\varepsilon 1} P_k - C_{\varepsilon 2} . \varepsilon) \tag{8.8}$$

The turbulent kinetic energy production term P_k is defined by:

$$P_k = \upsilon_T \left(\frac{\partial U_i}{\partial x_j} + \frac{\partial U_j}{\partial x_i} \right) \frac{\partial U_i}{\partial x_j} \tag{8.9}$$

Generally, two equation turbulence models are widely used in flow related engineering problems and there is ongoing effort to improve upon them. The essential features of two equation models are the extra transport equations/variables which represent both the energy in and the scale of the turbulence, and therefore account for history effects such as convection and diffusion of turbulence. One of the transported variables known as the turbulent kinetic energy (k) determines the energy in the turbulence or turbulent mixing tendencies, while the other determines the time- or length-scale of the turbulence, depending on the variant of two equation model. The length-scale is known as the turbulent dissipation (epsilon, ε), while the time-scale is known as the specific turbulence dissipation rate (omega, ω). These scale variants define the two main forms of two equation model: k-ε, and k-ω models.

The two equation eddy viscosity models include the broad group of k-ε, and k-ω models, and their derivatives obtained by imposing model constraints to curtail the tendency of over-prediction associated with two equation models. Common constraints that have been used in literature include Kato-Launder, Yap correction (near wall), and Durbin's realizability constraints as explained in [102]. The variety of the k-ε turbulence models are determined by the values of the model constants, and the additional term added to the left-hand side of Equation 8.8.

8.2.1 Standard k-epsilon model

The landmark standard k-epsilon model appeared in 1972 from the work of Jones and Launder [103], and was formulated by Launder and Sharma for low Reynolds number flow [104]. The values of the model constants are shown in Table 8.1 [105, 106].

The indicated constants have been tuned only to fit specific basic flow cases where shear layer is in local equilibrium, the ABL is neutrally stratified, grid turbulence is decaying, and the boundary layer is described by logarithmic velocity profile. Therefore, the standard k-ε model is not a general description of all flow conditions and has high uncertainties in predicting turbulence under non-neutral stratification of the ABL [105].

While the standard k-ε model is relatively straight forward to implement and leads to convergence easily at about 100 iterations, it requires wall functions implementation, and predicts poorly for flows involving separation, rotation or swirl (eddies), mixture of laminar and turbulence conditions [101] which are prevalent in complex terrains.

8.2.2 Modified k-epsilon model

To improve the fitness of the standard k-ε model, some of the model constants have been reviewed to c_μ=0.0324 and σ_ε=1.85, while others remain unchanged [105, 107, 108].

8.2.3 RNG k-epsilon model

For moderately and highly complex flows, Karthik (2011) recommends the use of Renormalization Group (RNG) k-ε turbulence model and Reynolds Stress Model respectively, with the later requiring high computational power [101]. The RNG k-ε turbulence model is derived using a statistical approach known as renormalization group method. It modifies the epsilon, ε Equation 8.8 by adding term (R) [108] to account for the effects of multi-scale motions including swirl, overcoming the defective single scale motion captured by the standard k-ε turbulence model. The additional term R is given by:

$$R = -\frac{\rho.c_\mu.\eta^3\left(1-{}^{\eta}/_{\eta_0}\right)}{1+\beta.\eta^3}\,\frac{\varepsilon^2}{k} \tag{8.10}$$

η_0=4.38, β=0.012, $\eta = SK/\varepsilon$, and $S^2 = 2.S_{ij}S_{ij}$. Other parameters are constants (Table 8.1).

Other literature give contentious perspective on the performance of RNG k-ε model over standard k-ε model for flow with vortex, but suggest its suitability for indoor air simulation [109, 110].

8.2.4 Standard k-epsilon model (with Yap correction)

Another variation of the standard k-ε model contains Yap corrections, i.e. with additional source term S_ε added to epsilon Equation 8.8 as follows [111]:

$$\rho.\frac{\partial}{\partial x_i}\left(U_i\varepsilon\right) = \frac{\partial}{\partial x_i}\left(\frac{\upsilon_T}{\sigma_\varepsilon}\frac{\partial\varepsilon}{\partial x_i}\right) + C_{\varepsilon 1}\frac{\varepsilon}{k}P_k - \rho.C_{\varepsilon 2}\frac{\varepsilon^2}{k} + \rho.S_\epsilon \tag{8.11}$$

The source term is expressed as:

Table 8.1: Empirical constants for the k-ε turbulence models [105, 106, 112]

Model	c_μ	σ_k	σ_ε	$C_{\varepsilon 1}$	$C_{\varepsilon 2}$
Standard k-ε	0.09	1.00	1.30	1.44	1.92
Standard k-ε (Yap)	0.09	1.00	1.31	1.44	1.92
Modified k-ε	0.0324	1.00	1.85	1.44	1.92
$RNG\ k-\varepsilon$	0.085	1.393	1.393	1.42	1.68
$RNG\ k-\varepsilon$	0.0845	0.71	0.71	1.42	1.68

$$S_\varepsilon \equiv 0.83\frac{\varepsilon^2}{k}\left(\frac{k^{1.5}}{\varepsilon l_e}-1\right)\left(\frac{k^{1.5}}{\varepsilon l_e}\right)^2 \tag{8.12}$$

where $l_\varepsilon \equiv {c_\mu}^{-0.75}\ k.y_n$ and y_n is the normal distance to the nearest wall.

The empirical constants for the turbulent closure schemes are summarized in Table 8.1.

8.2.5 The k-omega models

The k-omega model is probably the first two-equation model by Kolmogorov (1942) [113]. Unlike the k-epsilon models, the k-omega models use time-scale or frequency and performs well in the outer layer (near wall) and it depends on the smallness of vertical grid spacing near the wall (the finer the better near wall).

$$v_T = f_\mu.c_\mu\frac{k}{\omega} \tag{8.13}$$

$$\frac{\partial}{\partial x_i}(\rho U_i k) = \frac{\partial}{\partial x_i}\left(\rho\frac{v_T}{\sigma_k}\frac{\partial k}{\partial x_i}\right) + \rho(P_k-\varepsilon) \tag{8.14}$$

$$\frac{\partial}{\partial x_i}(\rho U_i\omega) = \frac{\partial}{\partial x_i}\left(\rho\frac{v_T}{\sigma_\omega}\frac{\partial \omega}{\partial x_i}\right) + \rho\omega.(f_1.C_{\omega 1}\frac{1}{k}P_k - f_2.C_{\omega 2}\omega) \tag{8.15}$$

$$\varepsilon = C_\mu.\omega.k \tag{8.16}$$

Similarly, the turbulent kinetic energy production term P_k is defined by:

$$P_k = v_T \left(\frac{\partial U_i}{\partial x_j} + \frac{\partial U_j}{\partial x_i} \right) \frac{\partial U_i}{\partial x_j} \tag{8.17}$$

where $f_\mu, f_1, and f_2$ are low Reynolds damping functions expressed as:

$$f_\mu = \frac{\frac{1}{40} + \frac{R_T}{R_K}}{1 + \frac{R_T}{R_K}} \tag{8.18}$$

$$f_1 = \frac{\frac{1}{f_\mu}\left(0.1 + \frac{R_T}{R_W}\right)}{1 + \frac{R_T}{R_W}} \tag{8.19}$$

$$f_2 = \frac{\frac{5}{18} + \left(\frac{R_T}{R_B}\right)^4}{1 + \left(\frac{R_T}{R_B}\right)^4} \tag{8.20}$$

$$Turbulent\ Reynolds\ number,\ R_T = \frac{k}{\omega.v} \tag{8.21}$$

where $\sigma_k = 2.0, \sigma_\omega = 2.0, C_\mu = 1.0, C_\mu = 0.09, C_{\omega 1} = 5/9, C_{\omega 2} = 3/40.$

Usually, k-omega models are favoured over k-epsilon models where flow is detached or separated from boundary layer, not fully turbulent, and recirculated (strong eddies). The commonly used k-omega models in literature include Wilcox's, Wilcox's modified, and SST k-omega models, and their near-wall derivatives. The Wilcox k-omega model (1988) has been employed in PHOENICS CFD tool which forms the root of many other CFD solvers, including WindSim CFD. The main reason for its application is the myriad number of its validation studies, and its extension for near-wall turbulence studies at a low Reynolds number. However, the main drawback is that it is affected by free stream pressure boundary conditions which causes over-prediction.

8.3 Boundary and initial conditions

The solution of the RANS equations for a domain require BCs to be specified for all perimeters of the domain, and for the solid surfaces within the domain. BCs are therefore specified for inlet/outlet boundaries, wall boundaries, and free-stream or entrainment boundaries.

Generally, the procedure for setting up the inlet boundary conditions CFD simulation involves estimates of inlet turbulence intensity either by measurement or from historical experimental experience. Common estimates in literature include 5-20%, 1-5%, and <1% for high, medium, and low turbulence scenarios respectively [102].

For the k-omega and k-epsilon models, different boundary conditions are specified for the turbulence variables at the three sections of the domain: wall, inlet, and free-stream as discussed below.

8.3.1 Free-stream boundary conditions

The free-stream boundary conditions are cell-centered BCs usually with a zero (outlet) or fixed value (non-outlet), and employs fixed pressure condition. The five velocity, pressure, and density variables in the flow field are set to the initial values [114], and the free-stream values for the turbulence variables k, ω, and ε are prescribed:

$$\begin{aligned} u_{initial} &= M_\infty \, cos\alpha.cos\beta \\ v_{initial} &= -M_\infty \, sin\beta \\ w_{initial} &= M_\infty \, sin\alpha.cos\beta \\ P_{initial} &= \frac{\rho_{initial}(a_{initial})^2}{\gamma} \\ \rho_{initial} &= 1.0 \end{aligned} \tag{8.22}$$

$a_{initial}$=1.0, a constant for free-stream sound speed.

Where ambient stream is taken to be turbulence-free, the values of k, and ε can be set to negligible, and the corresponding value of ω can be obtained from Equation 8.15. Literature has also shown that an omega ω value of zero in the free-stream has the implication of over-estimating the spreading rates of free-shear layers by over 20%, which confirms the

sensitivity of k-ω model to the free-stream value of ω. To curtail this sensitivity issues, Speziale et al.(1992) [115] and Menter (1992) [116] have suggested adding cross-diffusion source terms in the omega (ω) equation. On the other hand, there is no evidence in literature to suggest similar effects of free-stream conditions on the k-ε model.

8.3.2 Inlet boundary conditions

Like the k-ε models where values of the turbulence variables k and ε are specified at inlets, the values of k and ω are also specified as the inlet BCs for k-ω models. However, exact values of k, ω, and ε for the approaching turbulence are not known. Because the exact nature of the approaching turbulence is seldom known, the turbulence variables are estimated based on mere guess with high uncertainties. To get around the challenges of direct estimation of turbulence variables k, ω, and ε, other variables such as turbulence intensity I and turbulent length scale l or eddy viscosity ratio ($\frac{\upsilon}{\upsilon_T}$) are used as proxies and related to the primitive turbulence variables k, ω, and ε as follows:

$$Turbulent\ kinetic\ energy,\quad k = \frac{3}{2}.(U.I)^2 \tag{8.23}$$

$$Dissipation\ rate\ from\ turbulence\ length\ scale\ l,\quad \varepsilon = c_\mu \frac{k^{3/2}}{l},\quad or \tag{8.24}$$

$$for\ CFD\ codes\ (e.g.\ Phoenics,\ Fluent,\ etc.)\ that\ use\ mixing\ length\ l_m,\quad \varepsilon = {c_\mu}^{3/4} \frac{k^{3/2}}{l_m} \tag{8.25}$$

$$Dissipation\ rate\ from\ eddy\ viscosity\ ratio,\quad \varepsilon = c_\mu \frac{\rho.k^2}{\upsilon}.\left(\frac{\upsilon_T}{\upsilon}\right)^{-1} \tag{8.26}$$

$$Specific\ dissipation\ rate\ from\ turbulence\ length\ scale,\quad \omega = \frac{\sqrt{k}}{l} \tag{8.27}$$

$$Specific\ dissipation\ rate\ from\ eddy\ viscosity\ ratio,\quad \omega = {c_\mu}^{-1/4}.\frac{\sqrt{k}}{l} \tag{8.28}$$

where $U = \sqrt{{U_x}^2 + {U_y}^2 + {U_z}^2}$ is the mean inlet velocity, v is the molecular dynamic viscosity, $I \equiv \frac{u'}{U}$ where $u' = \sqrt{\frac{1}{3}({u\prime_x}^2 + {u\prime_y}^2 + {u\prime_z}^2)} = \sqrt{\frac{2}{3}k}$ is the root-mean-square of the fluctuating part of turbulent velocity, $l_m \approx 0.1h$, where h is a characteristic length dimension at the inlet or the boundary layer depth, and $c_\mu = 0.09$ is the usual turbulence model constant. As indicated earlier, the turbulent intensity I takes a value within 5-20%, 1-5%, and <1% for high, medium, and low turbulence respectively.

8.3.3 Wall boundary conditions

For k-ε and k-ω models, wall functions boundary conditions (BCs) are required, particularly along the ground [105]. Hence, the need for accurate digital terrain model.

By imposing particular relations at a normal distance y_n above the ground at the first grid point, where y_n is the default mixing length or the size of the default eddies proxied by domain width, and assuming the turbulence in local equilibrium state, the turbulence model variables are expressed as:

$$k = \frac{U_T^2}{\sqrt{c_\mu}} \tag{8.29}$$

$$\omega = \frac{U_T}{\sqrt{c_\mu . K . y_n}} \tag{8.30}$$

$$\varepsilon = \frac{U_T^3}{K . y_n} \tag{8.31}$$

The resultant frictional velocity U_T is expressed as $U_T = \sqrt{\tau_w / \rho}$. Where τ_w is the shear stress at the wall, $K = 0.4$ is von Karman's constant. Equations 17-18 are imposed inlet conditions with assumed log-law wind speed profile, which implies neutral stability of ABL.

8.4 Atmospheric stability

Owing to the uncertainties posed by the log-law wind speed profile (or neutral stability of ABL) in weak shear layers, analytical profiles for two-equation eddy viscosity models based on the Monin-Obukhov similarity theory have been developed and verified for the turbulence variables k, ε, and ω [117].

$$k = \frac{U_T^2}{\sqrt{c_\mu}}\left(1 - \frac{z}{h}\right)^2 \tag{8.32}$$

$$\varepsilon = \frac{U_T^3}{K}\left(\frac{1}{z} + \frac{4}{L}\right) \tag{8.33}$$

$$\omega = \frac{U_T}{\sqrt{c_\mu . K}}\left(\frac{1}{z^{0.5}} + \frac{2}{L^{0.5}}\right) \tag{8.34}$$

Monin-Obukhov (M-O) similarity theory is a globally accepted theory for the evaluation of the vertical profile of mean flow within the atmospheric surface layer (ASL) based on the stability length, L which corresponds to the vertical height at which the wind shear-induced turbulent kinetic energy equals the buoyant-induced turbulent kinetic energy [112]. The M–O similarity theory is therefore a way of capturing the contributions (to the overall turbulence) of mechanical turbulence due to wind shear instabilities, the buoyant (thermal) turbulence due to heated air instabilities, and buoyant suppression of turbulence (stable air).

Monin-Obukhov length, L is employed to express the non-dimensional stability class of the atmospheric boundary layer as follows:

$$\zeta = \frac{z}{L} = -\frac{\kappa . z . g . \left(\frac{H_{s,0}}{\rho_a c_p}\right)}{u_*^3 . \theta} \tag{8.35}$$

$\zeta = 0$ (neutrally stratified ABL)

$\zeta > 0$ (stably stratified ABL)

$\zeta < 0$ (unstably stratified ABL)

where $h = 0.4\sqrt{\frac{U_T L}{f}}$ is the earlier defined boundary layer depth, f is the Coriolis parameter, and L is the Monin-Obukhov length ($L \approx 10^4$ for a neutrally stratified atmosphere) [105].

The analytical profile for the turbulence kinetic energy, k expressed in Equation 8.23 therefore accounts for the combined effects of the ABL-specific physical processes such as the stability (buoyancy forces and heat transport) and Coriolis force which are usually ignored in some flow problems and solvers for simplification [118].

8.5 WindSim as a RANS solver

WindSim is a PHOENICS based computational fluid dynamics (CFD) simulator for forecasting wind fields and pollution dispersion at a local scale. The Parabolic Hyperbolic or Elliptic Numerical Integration (PHOENICS) is a general purpose CFD tool for quantitative study of fluid flow in process equipment, human system, buildings, engines, river, solid surface, among others [96]. It consists of a main computation program and a satellite program for tasks definition, and a subroutine that allows users to specify the sequence of coding [118, 119]. The main program contains the governing equations for conservation of mass, momentum, energy, and chemical species, and are solved by a finite-domain approach [120, 121]. It simulates changes in temperature, chemical and/or physical composition, and the associated stresses in the solids. PHOENICS presents distinct modules for performing functions such as problem definition, simulation, and presentation [119]. Problem definition is accomplished by specifying the geometry (shape, size, and position) of the domain, materials or fluid involved, the processes involved (e.g. turbulence, temperature, solid stresses), discretization of computational grid, and non-physical or numerical parameters that influence the convergence and accuracy of the simulation. The main advantages of PHOENICS over other CFD tools is the flexibility with which these problem definition tasks could be accomplished. It is open source with a high-level input language known as PIL which is reputed for its robustness, and requires no compilation. The flexibility of adding user defined subroutines makes PHOENICS an invaluable tool in the simulation of flow in the atmospheric boundary layer.

Generally, the CFD simulation of the lower parts of the atmospheric boundary layer within 0 to 200 meters is crucial to the accurate predictions of the atmospheric surface layer (ASL) processes. The challenges with obtaining accurate CFD simulation at the ASL usually arise when the wall function roughness term is defined by an equivalent sand-grain roughness (not aerodynamic roughness) without satisfying additional requirements. Blocken et al. (2007) [122] identified four basic requirements that should be satisfied in both upstream and downstream sections of the domain, and these include:

1. A sufficiently fine vertical grid resolution close to the bottom of the computational domain (with the height of first cell below 1 metre for a case with sand-grain roughness);
2. A horizontally uniform flow in the upstream and downstream sections of the domain in the ABL. The implication of this requirement is the integration of terrain roughness information into the simulation to forestall streamwise flow gradients in the upstream and downstream sections of the domain. This is usually done by using wall functions, based on aerodynamic roughness length z_0;
3. Sufficient vertical grid spacing. The first vertical grid spacing y_p (height between the bottom of the domain and the ground- or wall-adjacent cell) should exceed the physical roughness length k_s of the terrain. This essentially avoids blocking effects and unphysical acceleration;
4. Knowledge of the relationship linking the sand-grain roughness length z_s and the corresponding aerodynamic roughness length z_0.

Chapter 9

Methodology

Some of the major analytical and simulation tools used in this study are discussed, including flowcharts highlighting key steps from beginning to the end. Also included are qualitative discussion on general inputs required for the simulation, including turbine specification, virtual climatology, and steps such as discretization of computational domain preparatory to the CFD simulation.

9.1 WindSim modular platform and functionalities

WindSim simulation tool employs CFD approach to solve Reynolds averaged Navier-Stokes equations associated with the non-linear physics of wind flow over complex aerodynamic and environmental conditions. It simulates wind field (speed, direction, turbulence) subject to the given conditions of the terrain, and couples the results with long-term wind resource data measured or predicted from mesoscale models using statistical routines. The turbulence prediction functionality makes it a suitable tool in estimating turbine loads. It evaluates different wind farm layouts and assesses the trade-offs between AEP and turbine loads based on the solution of wind fields.

The user-friendliness of WindSim stemmed from the modular approach to simulation including description of steps and the progression of work flow; the add-on 'WindSim Express' which enables first time users to quickly set up CFD models which could be subsequently exported to main WindSim environment for a customized simulation. One essential prerequisite to using WindSim simulator is to first digitize the terrain over which wind flow is to be simulated. The extent, elevation, and roughness lengths for the terrain are defined in this process. The simplified flow chart in Figure 9.1 presents the steps in WindSim simulation at a glance.

WindSim model simulates the atmospheric flow at steady-state conditions. The model solution is obtained by incorporating a set of boundary and initial conditions derivable from the source

of wind resource data to be analyzed. In this project, a standard k-epsilon turbulence model is adopted in WindSim to achieve a closure for the undetermined Reynolds stresses associated with the Navier-Stokes equations after averaging or filtering.

To curtail divergence issues in WindSim simulation, some functionalities are activated either individually or collectively. This approach serves to avoid too many number of iteration to achieve convergence. The Terrain module has two main smoothing types- Bi-linear, and Gaussian smoothing. The smoothing routines essentially filter noisy or high frequency terrain points while preserving the main features associated with terrain discontinuity (such as ridges, etc.). Bi-linear smoothing procedure smoothens the terrain linearly in a 2D or x-y plane. On the other hand, the Gaussian smoothing routine smoothens the terrain at the surface and therefore it tends to give more smoothing than the bilinear routine. However, the WindSim guide indicates that the application of smoothing types should be done with care, and only where wind field solution is met with divergence which may be caused by sudden inclination changes between cells in the computational domain. Areas with likelihood of sudden inclination changes are identified as the extremities of mountain features such as sharp peaks or narrow valleys which are seldom required for wind farm siting. Therefore, such areas could be smoothened to get around divergence. Smoothing routine is quality-checked by inspecting the second order derivatives (a measure of the smoothness).

The simulation in WindSim forms the main task of the second stage in the downscaling (Figure 9.2) of UK regional WRF mesoscale model recently developed by a PhD researcher at the Institute for Energy Systems, The University of Edinburgh [7]. The UK WRF mesoscale model was developed by a higher resolution (3 km) reanalysis of the Weather Research and Forecasting (WRF) model developed by the National Center for Atmospheric Research.

9.2 Mapping of case study site - Braes of Doune wind farm

In this study, the case study site is the Braes of Doune wind farm located at approximately 25 kilometers North West of Stirling in Scotland, United Kingdom. The wind farm commissioned in 2006 has 36 units of Vestas V80-2 MW turbines installed, totalling 72 MW capacity. It is surrounded by complex terrain and therefore a good candidate for this study. The Ordinance Survey (OS) map for the United Kingdom is used to map out the site based on 7km × 7km dimension, about 50 square kilometer total area (Figure 9.3).

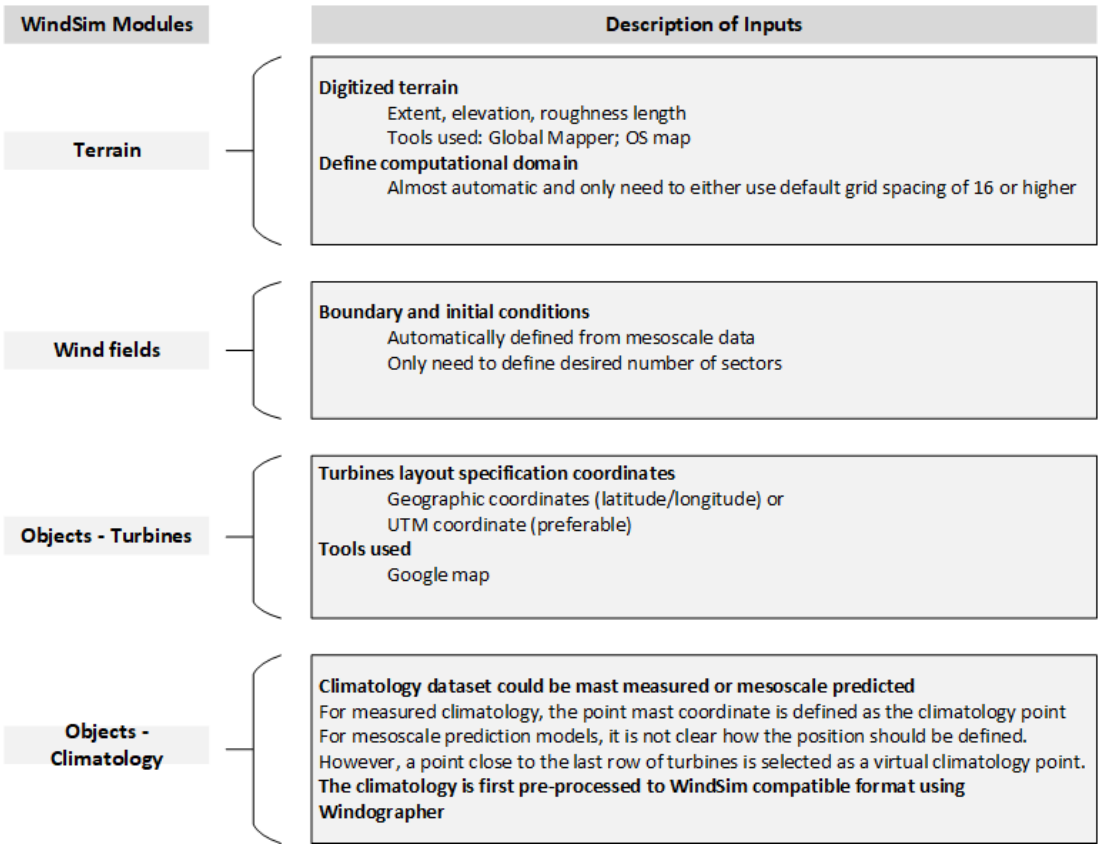

Figure 9.1: WindSim modular platform and the required inputs

9.3 Determine digital terrain model (DTM)

To incorporate site specific terrain information into WindSim model, a 7km × 7km digital terrain model containing terrain elevation, and roughness lengths is developed for Braes of Doune wind farm with the area coordinates in Table 9.1 and the wind farm coverage (Figure 9.4). Global Mapper is used to evaluate the orography of the site and to define the layout-considering forest, roughness length, and topography. The coordinate system is Universal Transverse Mercator (UTM), zone: 30, datum WGS84. The elevation data is obtained from online sources-ASTER GDEM v2 worldwide elevation data of 1 arc-second corresponding to 30 metres resolution. The roughness length is obtained from CORINE Land Cover Europe 2006 version with 100 metres resolution. OS map is used to identify the features and the selected coordinates for the wind farm coverage. The truncated versions of the resulting terrain elevation and roughness length contained in the digital terrain model is shown in Appendix Section A.2.3 and Section A.2.4 respectively.

The resulting map of the digital terrain models in terms of elevation, roughness length,

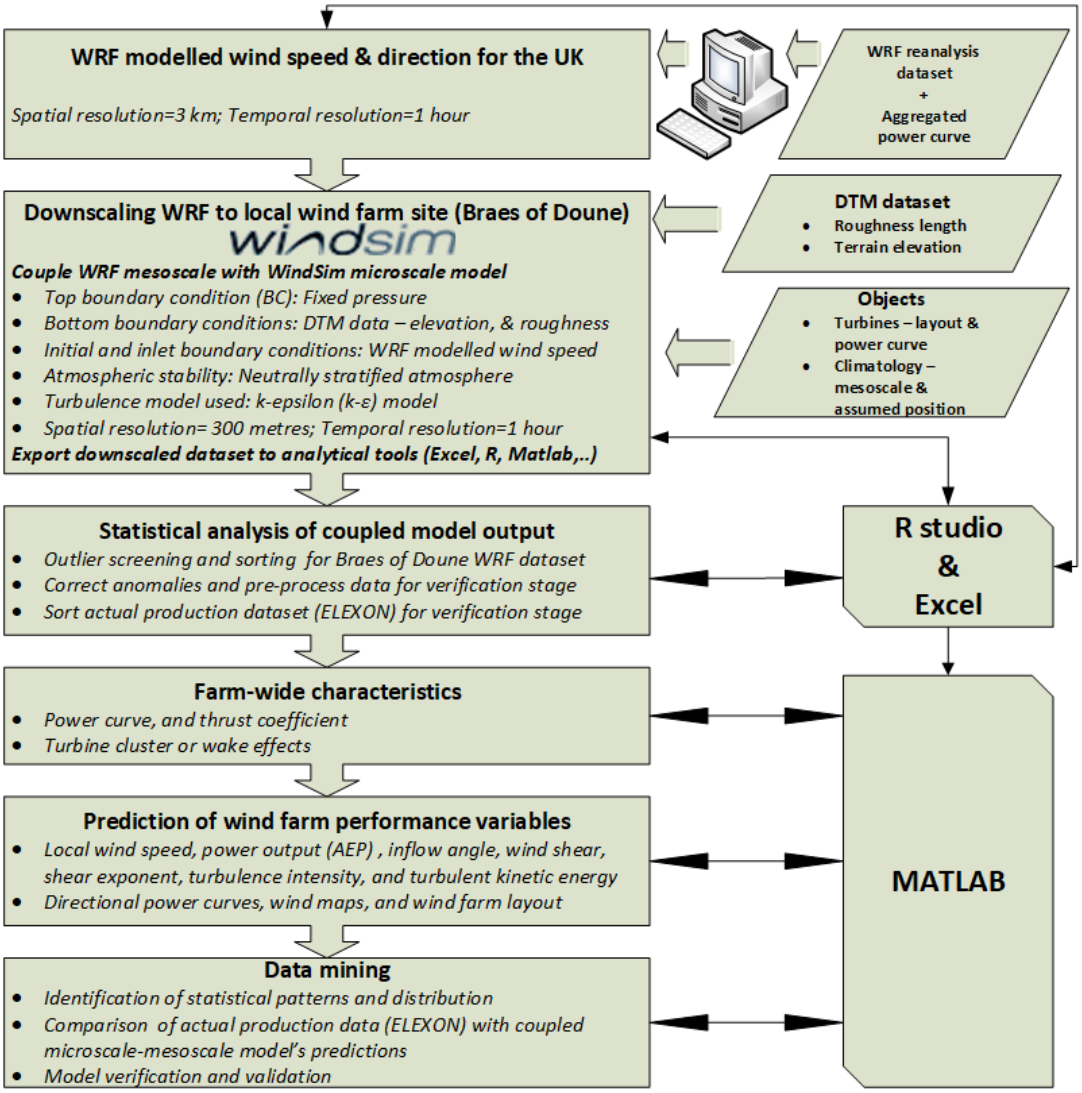

Figure 9.2: Approach for the spatial refinement of the UK WRF mesoscale to a local site

Table 9.1: Extent of digital terrain model based on UTM/30/WGS84

	Min [m]	Max [m]	Extension [m]	Resolution terrain data [m]
Easting [m]	428764.0	439198.3	10434.3	38.0
Northing [m]	6231421.5	6242081.5	10660.0	38.0

inclination angle, and logarithmic roughness are shown in Figure 9.5 and Figure 9.6. The terrain elevation and roughness length maps are derived from the digital terrain model data (obtained from Global Mapper) supplied to WindSim terrain module at the onset of the CFD simulation.

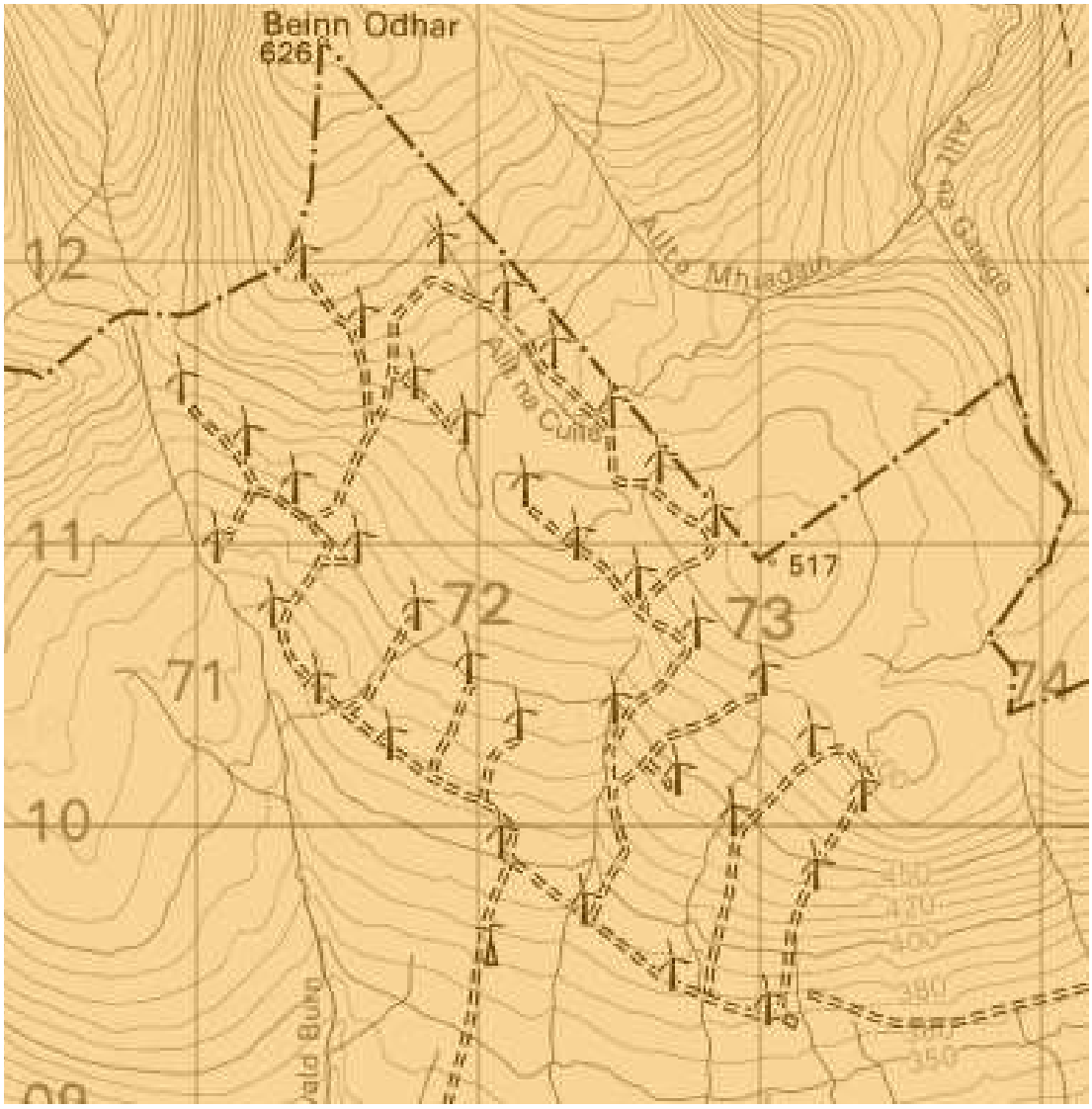

Figure 9.3: Wind farm site (7km × 7km)

The degree of terrain complexity at the site depends on the variation in elevation and logarithmic roughness length. The complexity in elevation is defined by the angle of inclination- which is a first order derivative of inclination.

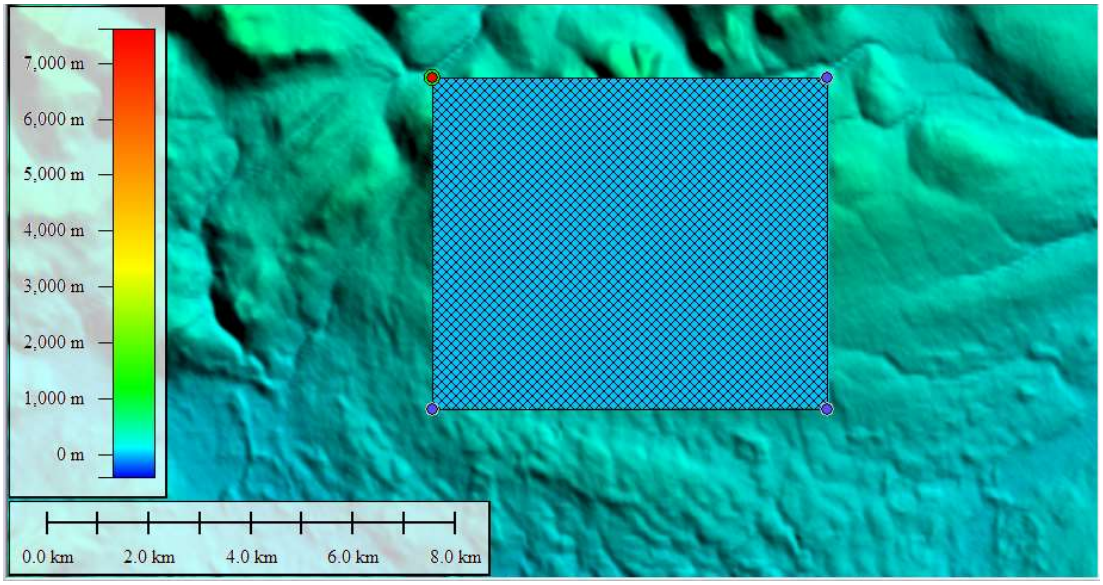

Figure 9.4: Extent of digital terrain model based on UTM/30/WGS84

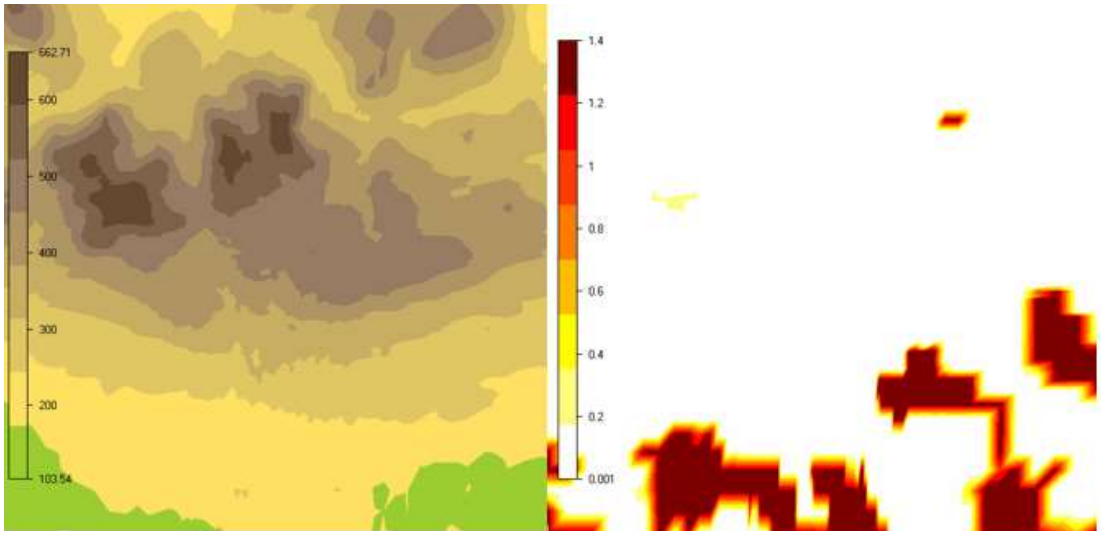

Figure 9.5: Terrain elevation (m) (left) and roughness length (m) (right)

9.4 Turbine specification

The Braes of Doune wind farm consists of 36 Vestas V80 2MW wind turbine with characteristic curve showing the warranted power curve and the thrust coefficient (Figure 9.7). From the technical specification sheet, detailed information on the turbine geometry and operating conditions are specified (see Appendix A.2, Section A.2.2).

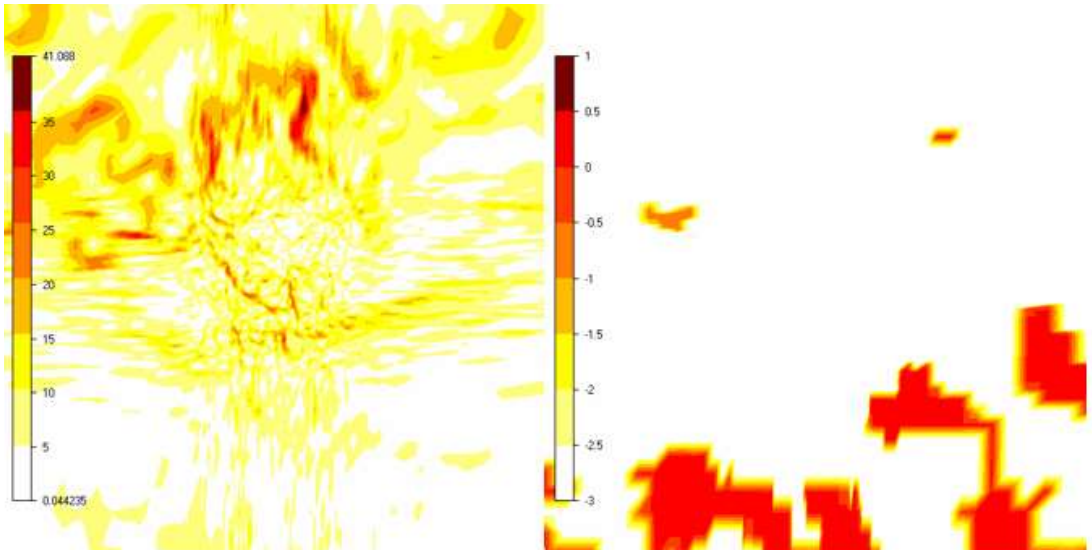

Figure 9.6: Terrain inclination angle (deg.) (left) and log-roughness (right)

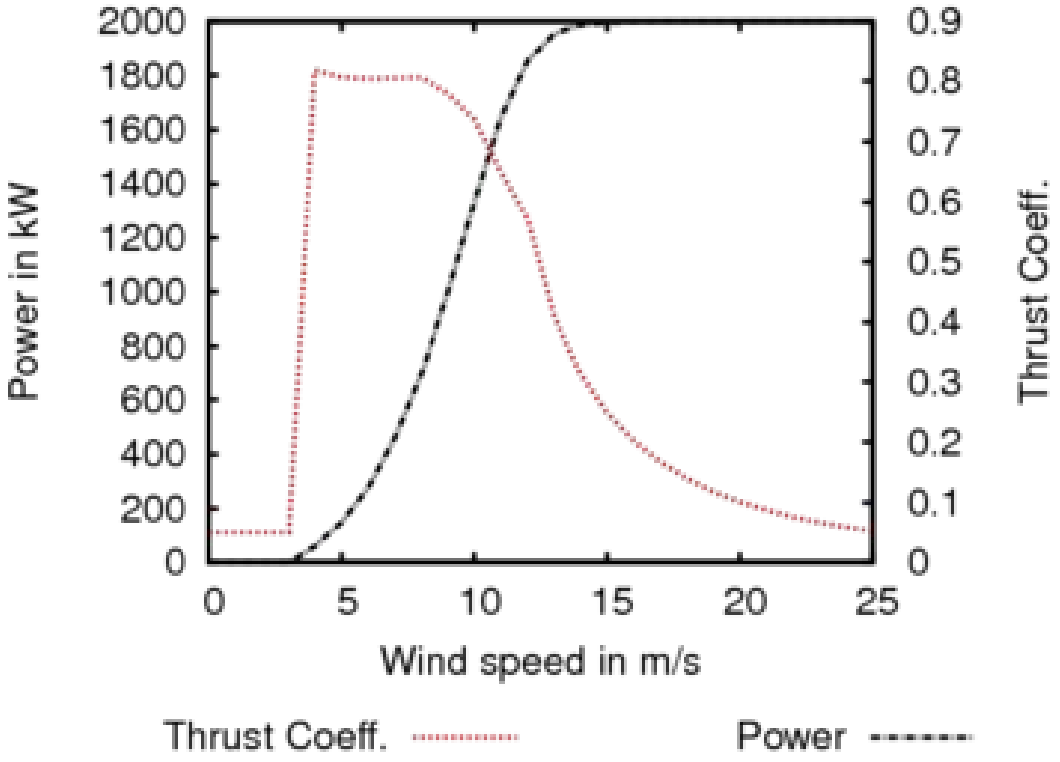

Figure 9.7: Wind turbine characteristics power curve and trust coefficient

9.5 Coupling WRF mesoscale-WindSim CFD model

In this study, a site-specific wind dataset for Braes of Doune wind farm is extracted from a 3-kilometer resolution and 11 years (2000-2010) simulated wind dataset obtained from WRF

Table 9.2: Grid spacing and number of cells

	Easting	Northing	z	Total
Grid spacing [m]	44.6-414.2	45.4-442.1	Variable	-
Number of cells	93	96	56	499968

mesoscale model for the entire regions of the United Kingdom [7].

To use the mesoscale data to drive the WindSim CFD simulation, a quality check is first conducted to remove suspect data and/or missing values using the R code created (Appendix Section A.2.4). The WRF dataset is pre-processed in Windographer to estimate the wind statistics of the site as wind rose. The average wind speed distribution is divided into 50 intervals (bins) and 12 equally-spaced directional sectors (0°, 30°, 60°,..,330°). The Windographer tool is also used to create a WindSim-compatible climatology file in 'tws' format for coupling with WindSim CFD model. The wind dataset is then downscaled using WindSim CFD tool to assess localized effects on wind flow field which mesoscale model do not capture.

The CFD solver and modular functionalities of WindSim makes it suitable for this study because it allows for consideration of different wake models, and inclusion of orography and surface roughness.

The annual energy production with and without wake consideration is determined for Braes of Doune wind farm considering a neutrally stratified atmosphere, terrain, and wake effects.

9.5.1 Discretization of computational domain

To apply the computational fluid dynamics (CFD) approach, the wind farm is modelled as a three-dimensional finite volume and then discretized into 499968 cells with variable resolution in the vertical and horizontal planes. The ground level of the 3D model is defined by the elevation and roughness length specified in the DTM (see Appendix Section A.2.3).

The grid is defined with an extent of 6 km above the highest elevation point in the terrain. The horizontal grid is then refined towards the centre within the area occupied by turbine clusters while the vertical grid is refined towards the ground as shown in Figure 9.8. The distribution of grid spacing and the cells across vertical and horizontal plane is shown in Table 9.2.

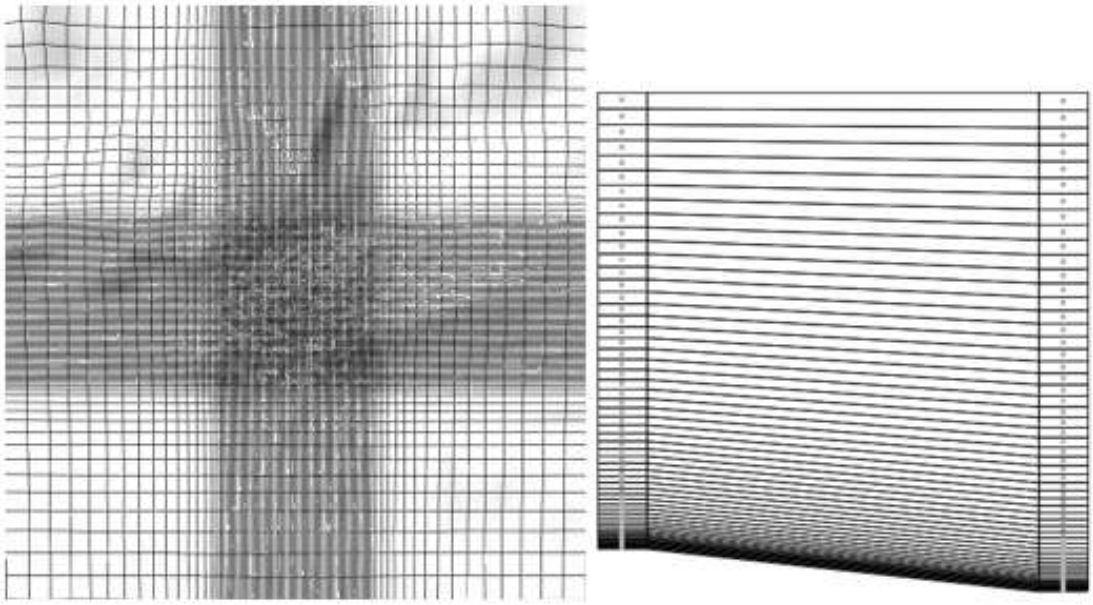

Figure 9.8: Horizontal grid resolution (left) and vertical grid resolution (right)

Table 9.3: Turbulence closure, initial and boundary condition settings

Pre-simulation conditions and criteria	Settings
Height of boundary layer [m]	500.0
Speed above boundary layer [m/s]	10.0
Boundary condition at the top (assumed free-stream BC)	Fixed pressure
Boundary condition at the bottom (wall or ground)	Roughness (DTM)
Initial and inlet boundary conditions	WRF modelled wind speed
Potential temperature	No
Turbulence model	Standard k–epsilon (k-ϵ)
Solver	GCV
Maximum iterations setting	100
Convergence limit for iteration	0.005

9.5.2 Initial and boundary conditions

To develop the wind field and velocity maps for each sector of each turbine and the entire wind farm (see Appendix A.2), Reynolds averaged Navier-Stokes equations applied to the computational domain are numerically solved in WindSim CFD tool based on the boundary and initial conditions, and convergence criteria in Table 9.3.

Table 9.4: Simulation time, number of iterations and convergence status

Sectors	Run time	Iterations	Status
000	00:25:40	90	C
030	00:24:49	87	C
060	00:25:20	92	C
090	00:25:47	89	C
120	00:28:56	83	C
150	00:28:55	89	C
180	00:26:11	90	C
210	00:28:36	97	C
240	00:25:06	85	C
270	00:25:32	90	C
300	00:29:10	81	C
330	00:32:30	98	C

9.5.3 Convergence criteria

A total of 12 simulations are performed, each for 30° spaced sector. The duration and the corresponding actual number of iterations are presented in Table 9.4. The status indicates that all the numerical simulations converged, giving more confidence on the solutions.

The convergence of the wind field evaluation is further evaluated by inspection of the spot and residual values of the velocity components (U1, V1, W1), the turbulent kinetic energy (KE) and its dissipation rate (EP) presented in Appendix Section A.2.8. The scaling of the variables is done according to the range of values obtained during the simulation for each sector. The simulation terminates when the solution falls below the set convergence limit of 0.005.

9.5.4 Turbine micro-siting and wind resource map

The Universal Transverse Mercator (UTM) co-ordinates system of 36 wind turbines at Braes of Doune wind farm are defined and used to set up the turbine layout (see Appendix A.2). The overall and directional wind resource maps are then determined for each sector at 60m turbine hub height.

9.6 Determine directional and aggregated farm-level power curves

The refined dataset downscaled to each turbine site is used to estimate the turbine's contribution to the overall wind farm power output or annual energy production. The refined dataset has wind speed and direction corrected to each turbine location. The implication is that both wind speed and direction varies when mesoscale dataset is downscaled to turbine hub height. This explains the dependency of wind farm performance not only on wind speed but also the direction. In other words, the wind flow swerved probably due to earth rotation and Coriolis effects reviewed in the literature Section 3.5.

To determine the farm-level power curves for each wind turbine therefore, directional effects are taken into cognizance by sorting the both WRF and microscale datasets by sectors, where each sector represents a range from its nominal value up to +29.9°. For example, 0° sector represents the direction within 0-29.9, 30° for 30-59.9, and so on. The R (statistical package) and MATLAB codes developed for the directional, aggregate power curves are presented in Appendix Section A.2.4 and Section A.2.5.

Chapter 10

Simulation and verification

This section gives major deliverables and findings in this study, including the wind farm characteristics layout, turbulence and wind shear parameters, wake characteristics, and annual energy production specific to the study site. Some of the discussion in this section related to data and figures presented in Appendix A.3 and in previous literature review sections.

10.1 3D layout for Braes of Doune wind farm

The result of CFD simulation in WindSim shows the 3D model of the wind farm in terms of terrain elevation and roughness length giving the visual impression of the site terrain in Figure 10.1.

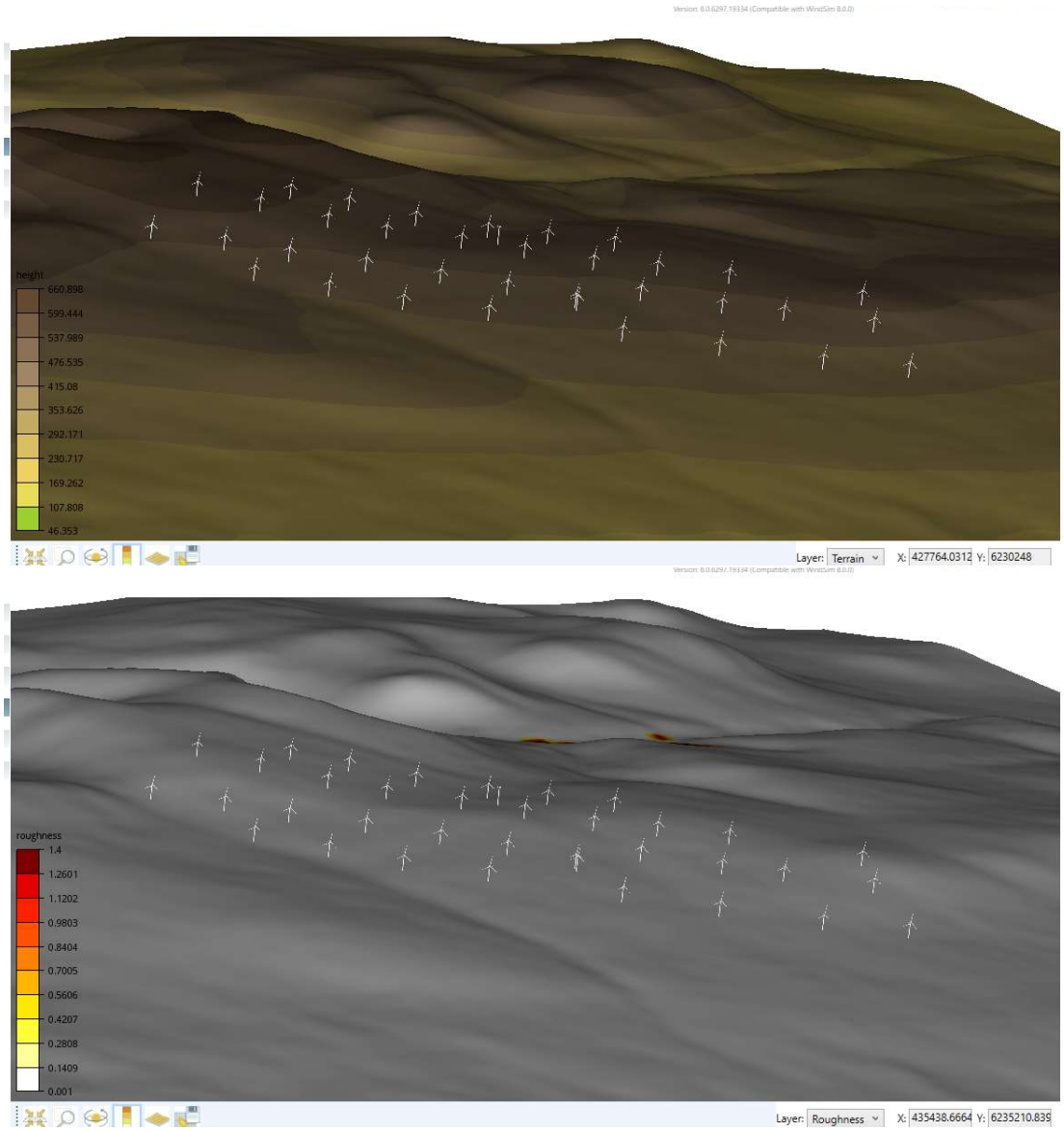

Figure 10.1: 3D layout. Upper: Terrain elevation (m); Lower: Roughness length (m)

10.2 Estimated wind resource characteristics

The statistical analyses of the simulated wind dataset give the distribution and the characteristics of wind resource over different sectors in Appendix Section A.3.9 and Section A.3.10, and the overall site wind rose and frequency distribution are presented in Figure 10.2. In addition, Table 10.2 shows the directional attributes of the local wind climate at the site of Braes of Doune wind farm.

Table 10.1: Summary of WRF climatology

Assumed position	Easting=434208.9 Northing=6237318.0 z(agl.)=60.0
Avg. wind speed, & Weibull k, A	$\bar{U}$=7.53 k=2.15 A=8.55 m/s
Period, & No. of records	01/01/2000 01:00 - 31/12/2010 23:00 96179

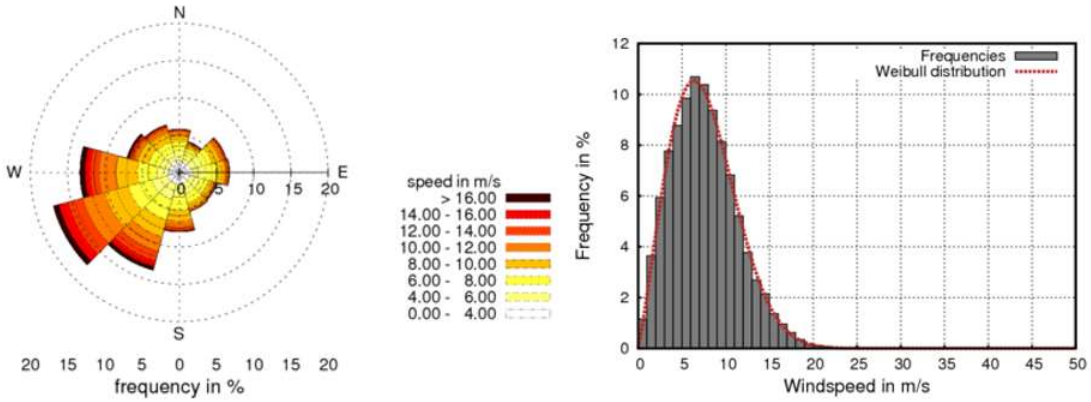

Figure 10.2: Site wind rose (left) and frequency distribution with Weibull fitting (right)

Table 10.2: Average wind speed, frequency and Weibull parameters per sector

Sectors	1	2	3	4	5	6	7	8	9	10	11	12
Average wind speed (m/s)	6.33	5.81	6.46	6.04	5.87	5.85	6.97	8.53	9.15	8.88	7.38	6.81
Frequency (%)	5.79	4.28	6.56	6.73	5.22	5.36	7.95	13.52	17.47	13.3	7.25	6.57
Weibull scale, k	2.11	1.89	2.19	2.3	2.19	2.23	2.29	2.31	2.62	2.49	2.22	2.23
Weibull scale, A (m/s)	7.16	6.59	7.35	6.86	6.64	6.59	7.87	9.58	10.38	10.07	8.51	7.89

10.3 Wind resource map, and anisotropic profiles of site variables

To visualize the variability of wind resource across the site, a wind resource map is presented in Figure 10.3 showing average wind speed at 60m hub height. It can be seen that the hilly spots located North of the wind farm have higher average wind speed due to speed-up effects and differential solar heating of higher terrain elevation. While such spot is a usually a good site for wind energy exploitation, it may also be a potential hot spot for high turbulence depending on the direction of wind flow field. Appendix Section A.3.17 and Section A.3.18 show that the

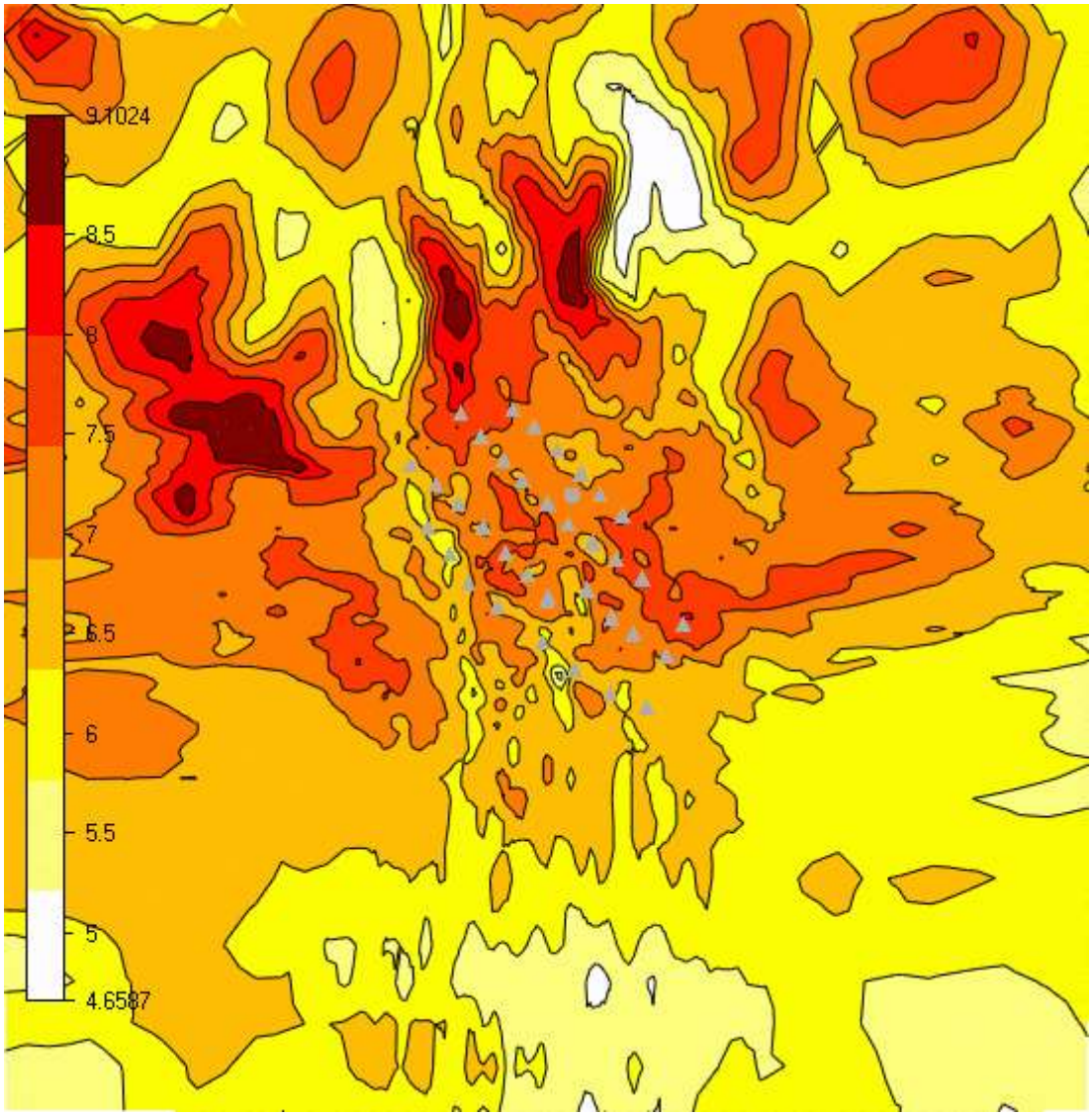

Figure 10.3: Wind resource map with average wind speed (m/s) at 60 m hub height

distribution of turbulence intensity and wind shear respectively also depend on the direction, and that a high wind site may not necessarily have high turbulence strength or shear because these phenomena dependent on local terrain effects and the thermal stratification of the atmosphere.

Therefore, wind resource map combined with the turbulence intensity and wind shear maps and the design turbulence intensity parameter for wind turbine could help inform decision in micrositing to ensure long service life for the turbine. This is also emphasized in the IEC 61400-1 recommended practice for wind turbine micrositing.

While this study can draw conclusion on the local terrain effects, the impact of thermal

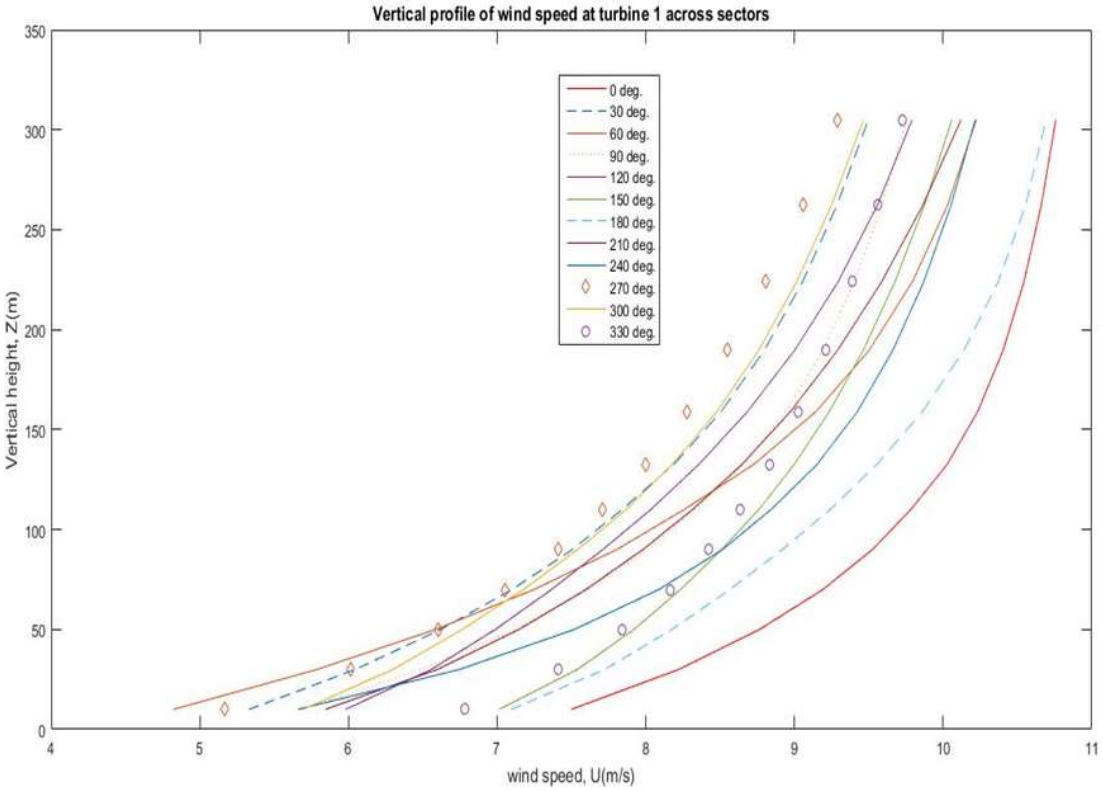

Figure 10.4: Vertical profile of velocity for different sectors

stratification which is characterized by Monin-Obukhov Length (MOL) is not investigated. However, the literature has highlighted strong relationship between wind speed, turbulence and stability, thus vertical profiles for these proxies are presented in Figure 10.4 and Figure 10.5, and vertical profiles for other variables, including the inflow angle, wind shear, turbulent kinetic energy are presented in Appendix A.3. Furthermore, the variation of turbulence intensity with wind speed is shown in the Appendix Section A.3.7.

The velocity profile compares to the logarithmic wind profile for neutral atmosphere in the atmospheric boundary layer discussed in the literature Section 3.5. Figure 10.4 shows that the vertical velocity profile is highly dependent on wind direction, and the steepest profile corresponds to 270° and 300° sectors where small changes in height results in larger changes in wind speed. Figure 10.5 indicates that turbulence intensity decreases with height for all sectors. The directional dependencies of the vertical profiles could also be attributed to terrain effects at the site, because incoming wind from different directions see different terrains. In other words, terrain effect is masked in the directional vertical profiles and may therefore be used to explain terrain impacts. For instance, 0° and 30° sectors (i.e. north-easterly direction)

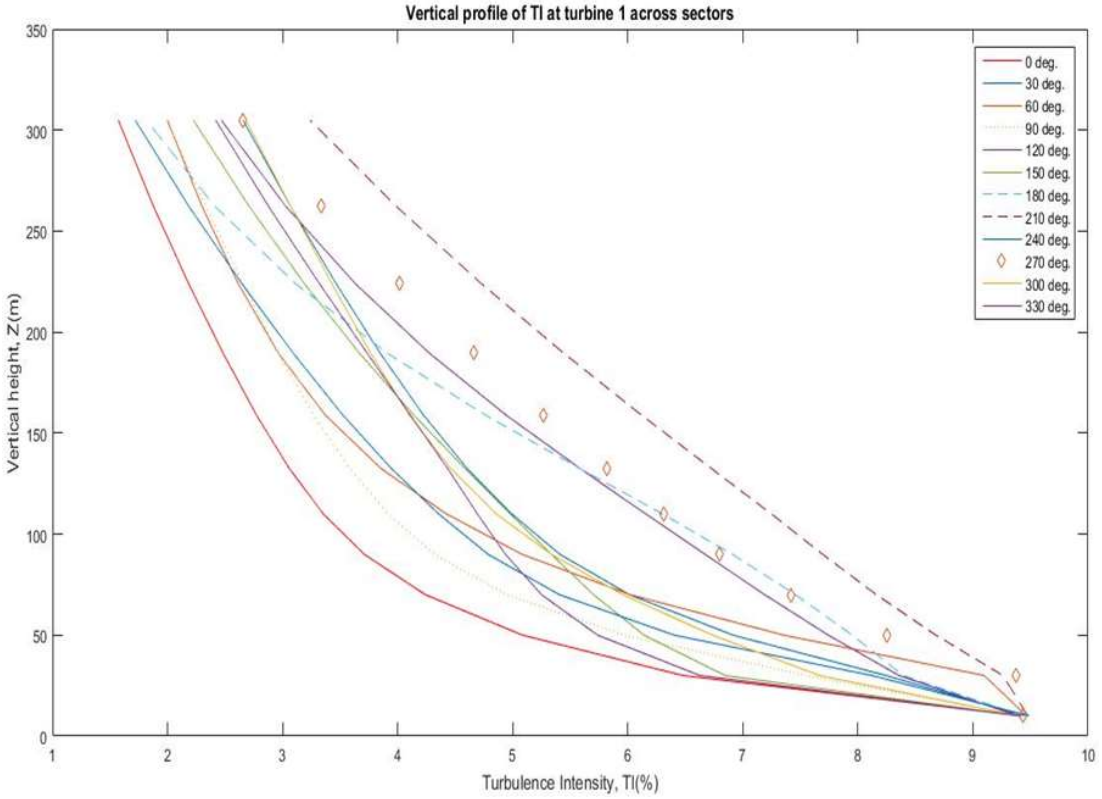

Figure 10.5: Vertical profile of TI for different sectors

could be regarded as having more impacts of terrain effect such as wind speed-up, while 270° and 300° sectors (i.e. south-westerly direction) see lowest speed-up.

Other important farm effect is the wake due to wind turbine clusters. This is an important consideration in large wind farms where regulatory requirements and limited land availability usually compel wind farm developers to localize wind turbines and optimize the use of land space. This usually comes with trade-offs between land use and reduced farm output due to wake losses ranging from 4-40% as documented in the literature section 6.0. To identify the wake model that better account for wake losses at the study site, the three wake models in WindSim are assessed at various effective range downwind of the rotor. The key input data for wake prediction are summarized in Appendix Section A.3.14.

The wake models by Jensen, Larsen, and Ishihara are tested for selected rotor diameters downwind and the results presented in Appendix Section A.3.16 suggest that Jensen and Ishihara models predict similar wake loss while Larsen model under-predicts at same rotor diameters ranging from 5 to 20. A caveat in judging the performance of these models based on this analysis is that while WindSim apparently relies on the specified WRF virtual climatology,

site layout and turbine characteristics to determine the free-stream wind speed, hub height, rotor diameter, roughness length, radial and downwind spacing required as wake model inputs, it is not clear how other inputs such as turbulence intensity and induction factor are inferred. Moreso, these input parameters could present uncertainties. However, all the wake models show the expected trend of predicting higher wake loss as the downwind distance increases because they are far-wake models as adjudged in literature Section 6.2.

The resulting wake loss calculated using Jensen model with effective range of 3-20 rotor diameters and the corresponding impact on the energy yield is presented in Table 10.3. The indicated wake loss, 13.3% is the derived by combining the wake loss attributed to individual turbine using the sum of square method. The choice of Jensen is based on the results of the wake model test and the effective range is chosen to cover the turbine spacing at the Braes of Doune wind farm which is around 4 and 8 rotor diameters for crosswind and downwind respectively.

10.4 Estimated annual energy production

The annual energy production (AEP) is determined for individual wind turbines at the site, and then aggregated together for the entire wind farm. The power curve used for AEP calculation is corrected for wind density at the vicinity of the wind farm. The Braes of Doune wind farm is at elevation of 472m above mean sea level (see Appendix Section A.3.13), and the corresponding wind density is 1.192 kg/m^2 determined from the characteristic wind density curve at the Braes of Doune wind farm given in Appendix Section A.3.11. The calculation of the aggregate is based on the wind farm area zoned according to their average wind speed adjusted for wake loss and terrain effect (see Appendix Section A.3.15). The four zones are characterized by full load hours, FLH (which depends on the hours the average wind speed for a zone occurs in one year or the frequency distribution of wind speed), and the zone area, A. To calculate the total AEP for the wind farm, the products of these zone characteristics are summed up and then multiplied by the total installed capacity (C_i) as expressed below.

$$AEP\left(\frac{Wh}{yr}\right) = C_i\left(\frac{W}{m^2}\right) \times \sum_{all\ zones} FLH\left(\frac{hr}{yr}\right).A\left(m^2\right) \tag{10.1}$$

Table 10.3: Estimated wind farm output with and without wake effect

Turbine model [Vestas]	Hub height [m]	Number of turbines	Installed capacity [MW]	Gross AEP [GWh/y]	Average wind speed [m/s]	Wake losses [%]	AEP with wake losses [GWh/y]	Full load hours	Capacity factor [%]
V80_2MW	60.0	36	72.0	199.4	7.0	13.3	172.8	2400.2	27.4

The installed capacity, C_i used for the Braes of Doune wind farm is 1.44 MW/km^2 based on 50 km^2 site area. The gross AEP is the energy calculation with no wake loss considered.

The summary of energy calculation and the input parameters are presented in Table 10.3.

10.5 Directional power curves from coupled model versus WRF

The directional dependency of wind farm performance is investigated to establish statistical patterns that could be compared with that of actual production data, and ultimately derive an aggregate power curve that faithfully model the actual wind farm output. The power prediction by the coupled model compared to WRF and the manufacturer's power curves for each sector are presented below for glance comparison. The Figure 10.6 to Figure 10.8 are based on a 11-year dataset from 2000 to 2010 for WRF and Coupled model only. The warranted power curve is based on manufacturer's specificied power curve for V80 2MW Vestas model.

It is seen that the directional WRF and the directional power curves from downscaled dataset behave differently, while that of manufacture's compares closely to WRF. This is expected because the UK WRF datasets was derived by fitting WRF mesoscale model to the aggregated manufacture's (warranted) power curve in the earlier work by Hawkins [7]. The new directional power curves developed in this work show two operating regions in a fashion that seemed like a 'hysteresis loop' between the cut-in and cut-out regions. Typically, conventional hysteresis effect in wind turbines are usually triggered by events of gusty wind and controller failures, and it usually occurs at the tail end of cut-out region. However, it is not clear if the downscaled model has been able to capture the conventional hysteresis but what is immediately apparent with the observed pattern is that at any given wind speed, all the turbines do not operate in the same mode due to their geographical spread, and some are tripped-off probably by control actions which react against events, including wind storm, that are programmed for turbine shut-down especially with pitch-regulated wind turbines. The setting used in WindSim

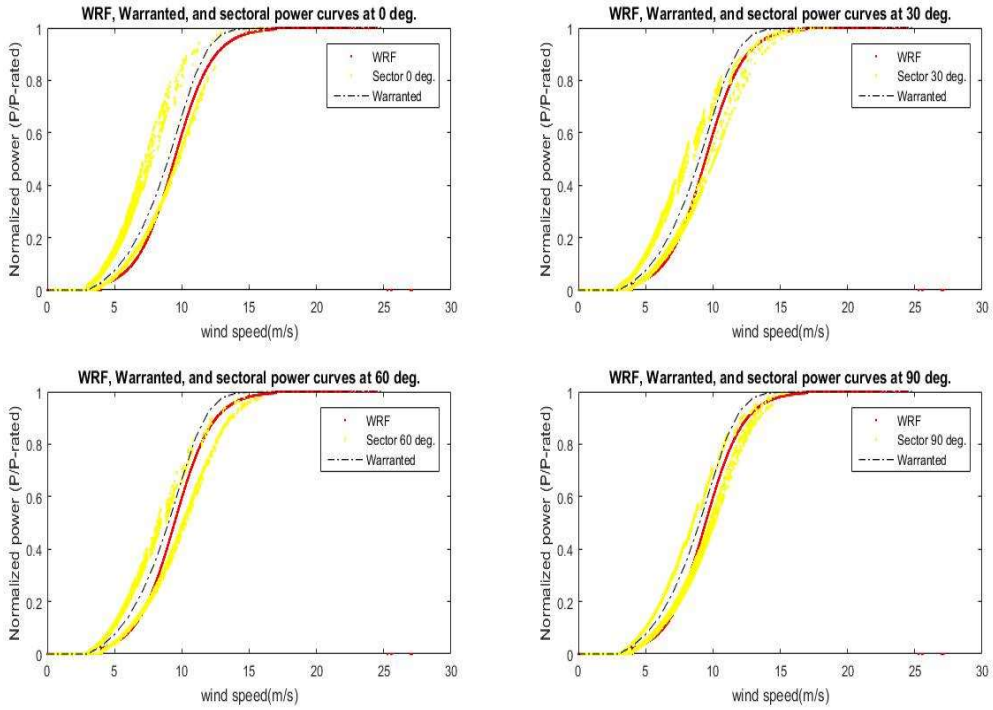

Figure 10.6: Directional power curves comparison for 0 – 90° sectors

simulation for density correction is 'pitch-regulated WEC' which means the power curve of the wind turbines is corrected to site-specific wind density. The warranted power curve comes with a standard air density which does not match that of the site.

10.6 Directional power curves versus actual production

Furthermore, the coupled model is compared with actual production data from ELEXON over a period of 2 years (2009-2010). Same length of data is extracted from the model dataset and matched with the ELEXON dataset, and some gaps are found in the ELEXON dataset. To resolve, parts of the model dataset are screened out in excel to obtain a match with ELEXON's. The WRF wind speed and direction is assumed true for ELEXON while the model uses the refined wind speed. Another way to test these dataset is to use the wind speed and direction of the refined model as a basis for comparing the predicted output and the actual production, and this is recommended for future investigation.

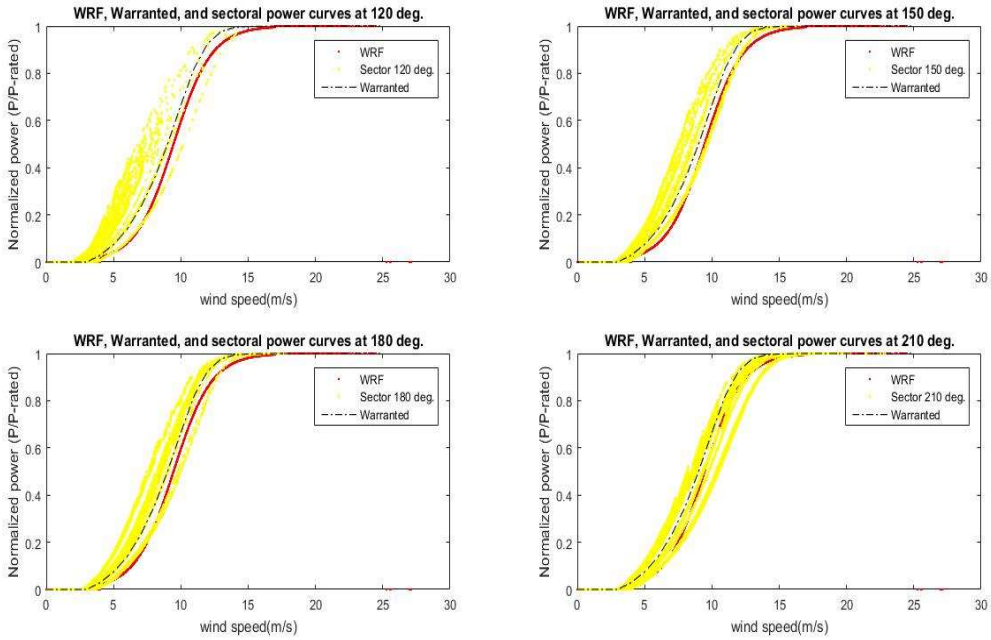

Figure 10.7: Directional power curves comparison for 120 – 210° sectors

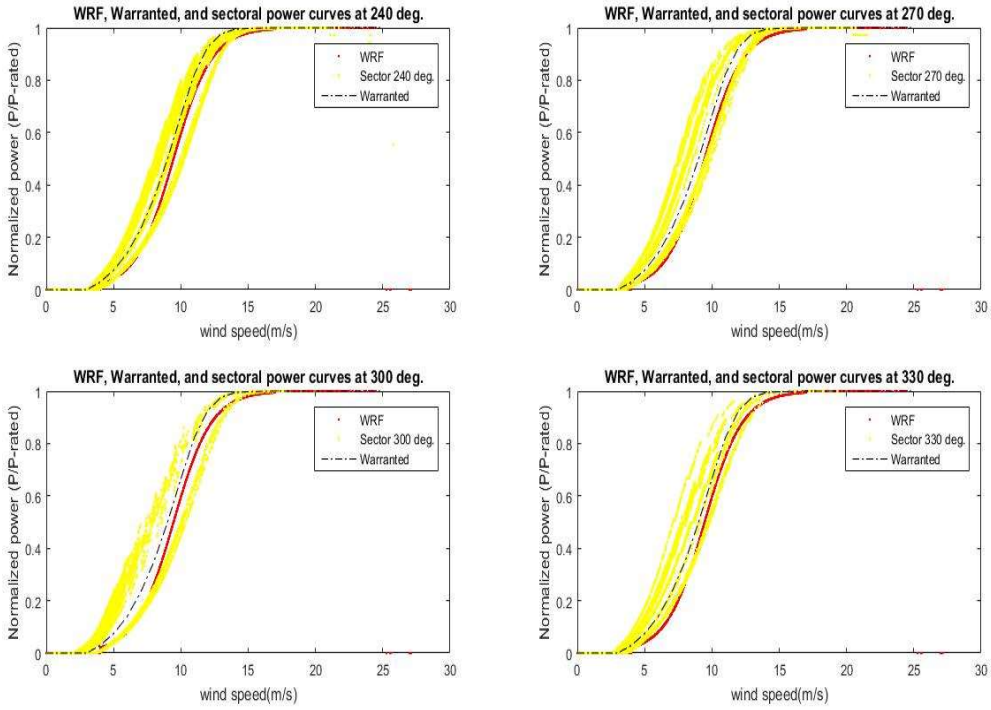

Figure 10.8: Directional power curves comparison for 240 – 330° sectors

Both datasets are sorted by sectors to assess directional effects, and the resulting power curves are presented in Figure 10.9 to Figure 10.11 for all 12 sectors, where 0-29.99 is the range for sector 0° and so on.

Similar split is noted in the power curves based on the 2-year model dataset as it is the case for the 11-year dataset. The model appears to predict actual production well in the sectors from 180° to 270° or south–westerly direction, confirming the patterns of wind rose presented in Appendix Figure A.3.10. The frequency distribution of WRF wind speed presented in Appendix Section A.3.12 also shows similar pattern.

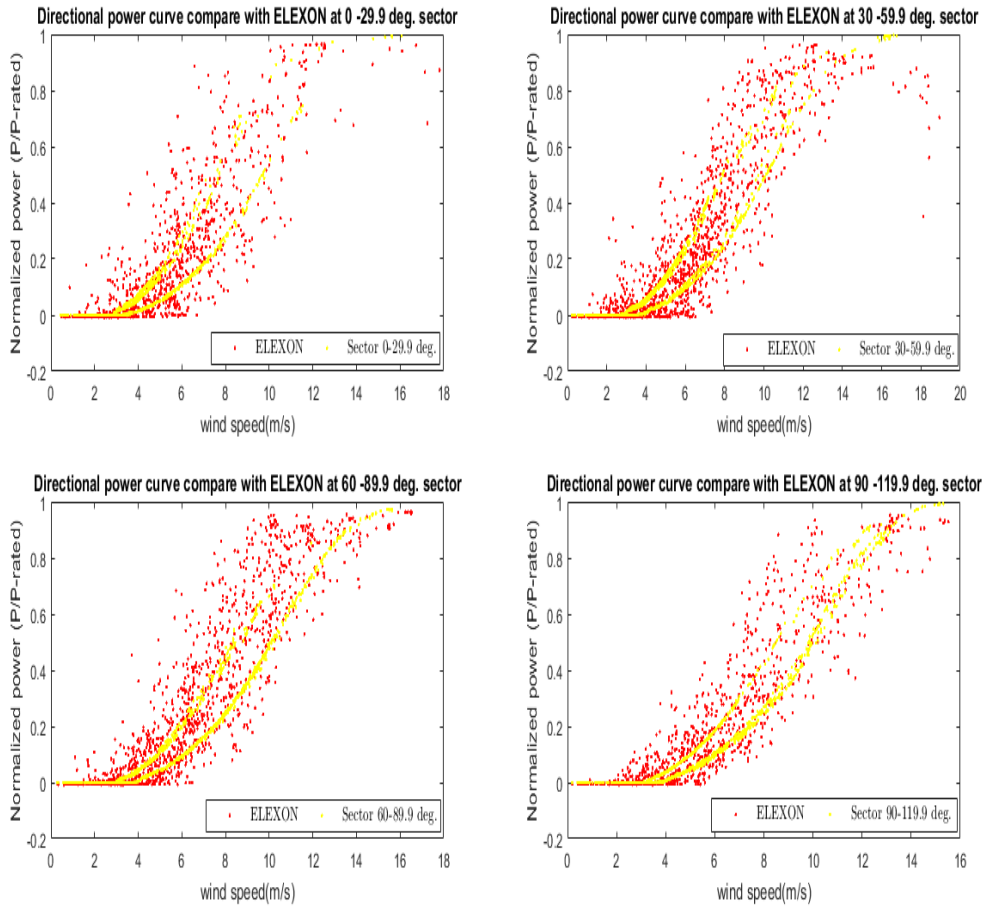

Figure 10.9: Directional power curves for 0 – 120° sectors - coupled model vs ELEXON

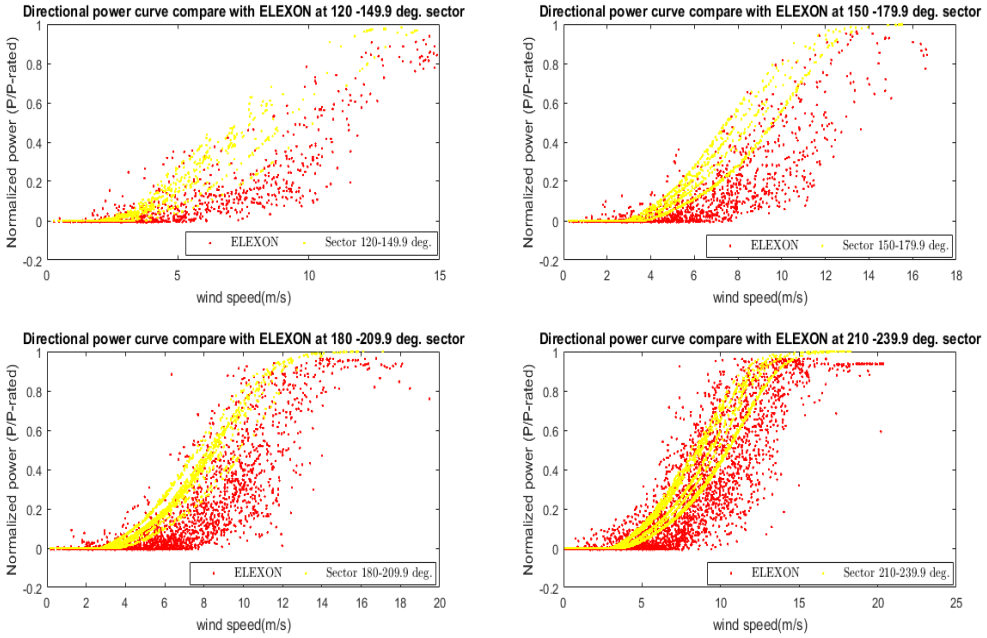

Figure 10.10: Directional power curves for 120 – 240° sectors - coupled model vs ELEXON

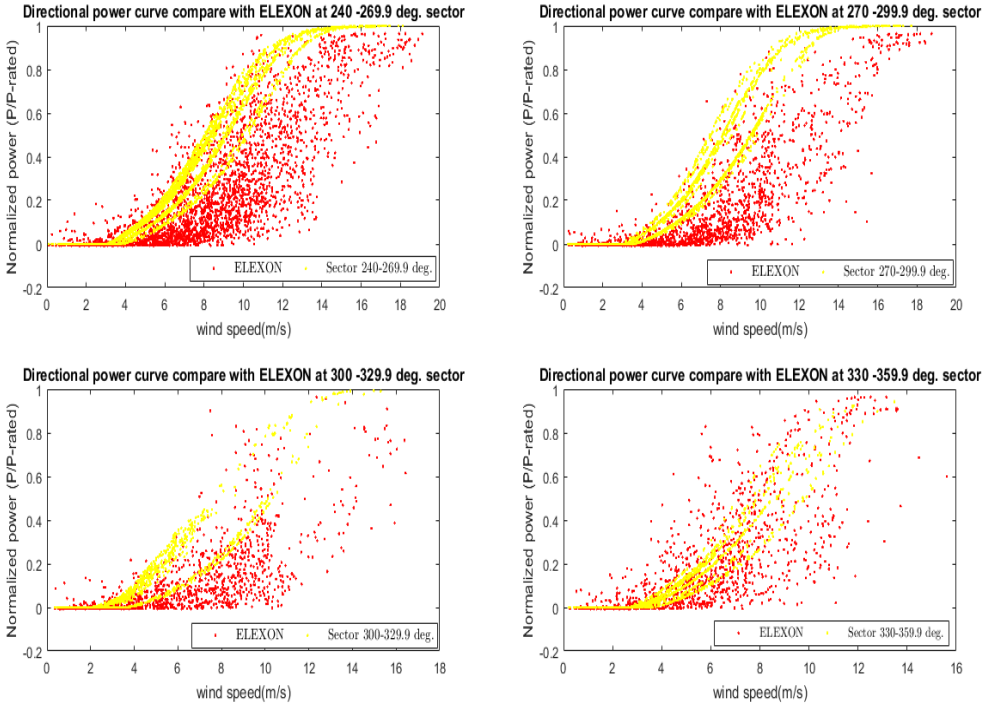

Figure 10.11: Directional power curves for 240 – 360° sectors - coupled model vs ELEXON

10.7 Overall farm-level power curve against actual production

The power curve derived from the 2-year model dataset with all sectors is presented in Figure 10.12. Again, the predicted model ('yellow') shows two separate regions, and fits within the production data and does not over-predicts actual production within the operating wind speed. However, it appears to slightly overpredicts at high wind speed approaching cut-out.

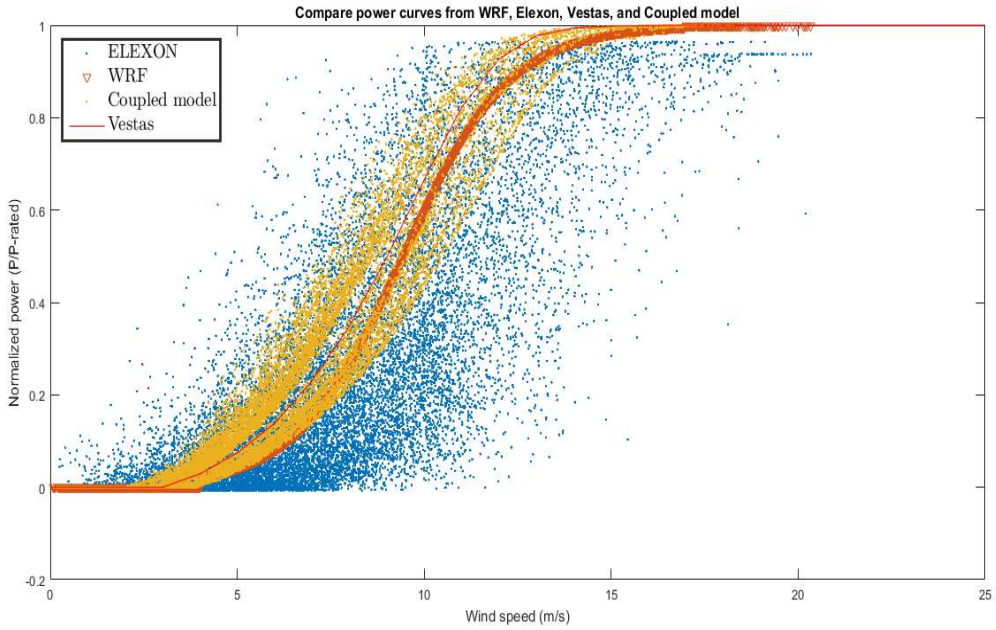

Figure 10.12: Directional power curves for 210 – 330° sector - coupled model vs ELEXON

10.8 Performance of coupled models using RMSE criteria

The goal is to use the resulting models for predictions, therefore it is necessary to assess the model performance compared to actual power production data for Braes of Doune wind farm obtained from ELEXON company. For forecasting purposes, the Root Mean Square Error (RMSE) which computes the variance of the residuals, is the most commonly used criteria becauses it gives an absolute measure of fit rather than a relative measure of fit. The lower the value of RMSE, the better the model predicts the actual power production data.

To assess the model predictive power, root mean square error (RMSE) is calculated by solving Equation 10.2 in the MATLAB code in Appendix Section A.2.5.

$$RMSE_{model} = \sqrt{\frac{1}{N} \sum_{all\ hours} (P_{elexon_{norm}} - P_{model_{norm}})^2} \tag{10.2}$$

$$RMSE_{WRF} = \sqrt{\frac{1}{N} \sum_{all\ hours} (P_{elexon_{norm}} - P_{WRF_{norm}})^2} \tag{10.3}$$

where $P_{elexon_{norm}}$, $P_{model_{norm}}$, and $P_{WRF_{norm}}$ are normalized power for ELEXON, model, and WRF outputs respectively, expressed as follows:

$$P_{elexon_{norm}} = \frac{P_{elexon}}{P_{rated}} \tag{10.4}$$

$$P_{model_{norm}} = \frac{P_{model}}{P_{rated}} \tag{10.5}$$

$$P_{WRF_{norm}} = \frac{P_{WRF}}{P_{rated}} \tag{10.6}$$

where P_{rated} = 2 MW is the rated power of a reference Vestas wind turbine at Braes of Doune wind farm. The normalized power outputs have no units.

The RMSE forecast error when the coupled model developed in this work is used to predict the 2009-2010 actual production data (from ELEXON) for the Braes of Doune wind farm is 28.21%. This shows a large improvement compared to RMSE error of 685.98% when the WRF model is used to predict the actual output from ELEXON. In a related work by Timmers (2017) [73], the MATLAB-based model developed by the author gave RMSE errors in the range of 37.9-122.6%, and RMSE errors of 50.3-303% for WRF model over 60° to 1° sectors respectively as shown in Table 10.4. The MATLAB-based model considers wake losses but ignores the site's complex terrain effects.

Attempts at computing the RMSE and mean bias error (MBE) per sector proved abortive due to the difference in length of sectoral dataset between the coupled model developed in this work, and the ELEXON. Therefore, the compuataion of RMSE for the coupled model and WRF predictions are based on aggregate of all sectors and not on per sector basis as computed by Timmers 2017 [73]. While this accounts, in part, for the deviations shown in Table 10.4, it is obvious that the coupled model predicts the power output better than any previous models

Table 10.4: Comparison of RMSE errors

Timmers (2017) [73]	Sector	$RMSE_{MATLABmodel}$ (wake effect)	$RMSE_{WRFmodel}$
	1°	122.6%	303.0%
	60°	37.9%	50.3%
This work	Sector	$RMSE_{Coupledmodel}$ (wake & terrain)	$RMSE_{WRFmodel}$
	Aggregate (all 12 sectors)	28.21%	685.98%

investigated in literature. Although the computed RMSE error of 28.21% gives confidence in the predictive power of the coupled model, the error should be further evaluated by sector to account for directional effects. It is also expected that directional effect will not have much impact on the overall output since wind turbines are equipped with control mechanisms that yaw them towards the wind, except the yaw misaligns due to excessive loading or misaligned deliberately out of high wind speed. If the aggregate RMSE for all the 12 sectors is assumed to be evenly distributed by sector, the average gives the equivalent RMSE of about 57% and 2.4% for WRF and coupled models respectively. However, while it is obvious that RMSE is not evenly distributed across sectors as confirmed by Timmers result in Table 10.4, it is suspected that sectoral or directional RMSEs could be added together to form an aggregate RMSE.

Chapter 11

Discussion

The central discussion in this section is on the relationship between the findings from this study, the literature review, possible sources of uncertainties, and the limitations of the coupled model.

11.1 Findings and implications

The WindSim tool has been used in this study to serve the dual purpose of modelling effects due to the orography and roughness of terrain and wind turbine wake. This has been difficult to accomplish in linear tools which are designed with wind farm on simple terrains in mind. The task is fulfilled in WindSim and a new dataset adjusted for terrain effects such as speed ups, and turbine wake is obtained. Furthermore, the limits of WindSim tool is complimented with MATLAB, Excel and R studio packages to analyze the dataset derived from coupled mesoscale-microscale model in WindSim. This is done to obtain graphical results for the vertical profiles of wind farm variables such as local wind speed, wind shear, inflow angle, shear exponent, turbulence intensity, turbulence kinetic energy, and the statistical patterns of the dataset compared to actual production.

The results of the statistical distribution reveals that the popular Weibull and Rayleigh distribution functions do not fit the wind speed at Braes of Doune wind farm. The probability distribution functions that come close to best fit are the generalized extreme value (GEV) and Kernel distributions as shown in Appendix Figure A.4.3b and Figure A.4.4b, and similarly for the WRF model in Appendix Figure A.4.3a and Figure A.4.4a. This is probably due to the multi-modal wind speed regime at Braes of Doune wind farm. The PDF-type that mimics the repeated peaks is the Kernel distribution. This could be indicative of extreme wind events at Braes of Doune wind farm. The implications of these observed statistical patterns are two fold:

- Wind speed regime at the site is not continuous but discrete. So, continuous PDF is no good match;
- Wind farm power output needs a more robust distribution function. GEV does not predict the tail well.

This work demonstrates that WindSim simulation, complimented by other packages gives rich amount of dataset, and statistical information for making informed decision about micro-siting, forecast of local wind regimes, and accurate power predictions which are central to wind integration and grid operations. Since this work relies on WRF dataset, WindSim microscale model, including the wake and turbulence models, and different external sources of terrain and roughness information, these could potentially pose uncertainties in the reliability of the model. This study has been able to partially validate WindSim, other sources of uncertainties are not validated in this work. Therefore, this model could be improved for site-specific predictions by accounting for the uncertainties.

Chapter 12

Conclusions

This section highlight key findings, and the direction for future studies to compliment this study.

12.1 Concluding remarks

In this study, WRF mesoscale model is successfully coupled with WindSim microscale model to generate a refined wind resource datasets with high resolution suitable for predicting local wind regimes, feasibility studies, and ultimately the production forecasts. The model works by using WRF wind speed dataset as inlet boundary conditions (BCs), fixed pressure as top boundary condition, and the terrain roughness and elevation as the bottom boundary condition to solve the Reynold-averaged Navier-Stokes equations 8.2 and 8.3 for each cell in the discretized wind farm domain (Figure 9.8). To obtain as many equations as the unknowns, the k-ε turbulence model (Equation 8.4 - 8.9) is used for closure, and the atmosphere is assumed neutrally stratified. In other work in the literature, bottom boundary conditions have been assumed using sand-grain roughness without meeting the additional requirements discussed in § 8.5, thus leading to increased uncertainties. To fill this gap, a digital terrain model is developed in this work with detailed information on aerodynamic roughness for the entire terrain section of the Braes of Doune wind farm. So, WindSim CFD presents a better approach of specifying the wall or ground boundary conditions by incorporating the actual aerodynamic roughness that interacts with local wind regime.

To conclude, the results of this work could be used in feasibility studies for siting wind farm on a moderately complex terrain, the type presented in the 3D layout in Figure 10.1 by supplying a trusted sources of terrain elevation and roughness data with high resolution below 100 metres equivalent. Also, the wind farm production forecasts could be assessed for future operational planning with a root-mean square error (RMSE) of 28.21%.

12.2 Future work

As outlined in the discussion, there are opportunities for improvement in the robustness of the coupled model. One aspect is to use other sources of terrain elevation and roughness data to derive the DTM as WindSim input. Also, the need for deeper understanding of the types of boundary conditions and turbulence models used in deriving the WRF dataset will help to improve this work. Literature sources indicates that types of turbulence closure model used in mesoscale model does affect the choice of closure scheme for micro-scale modelling. This aspect needs to be investigated further in future work. Also, WindSim includes three wake models which are investigated in this study, consideration of other wake models especially the actuator disc coupled models could be useful in modelling the aspect of wake–terrain interactions. Interactions with WindSim experts shows that this could be done in WindSim to model the wind turbine rotor as an actuator disc. However, this is not attempted in this work. In addition, this model could be improved by validating against different sources of terrain data; using other forms of turbulence models; non-neutral atmospheric conditions; and by modeling the rotor as actuator disc and further downscale to higher resolution in tens of meters to capture terrain-wake interaction effects bearing in mind the implication on high computational costs.

Appendix A.1

Appendix to Chapter 1

A.1.1 Global wind power landscape and energy mix

Note: Compound Annual Growth Rate (CAGR) - The growth rate over multiple years based on compunded installed capacity of onshore and offshore wind power, $CAGR = (IC/IC_0)^{1/n} - 1$ where IC is the cummulative installed capacity at nth period, IC_0 is the cummulative installed capacity at the beginning of the period, n is the period (in years). CAGR is expressed as a percentage.

Figure A.1.1: Global installed and projected capacities of wind power (MW) [123]

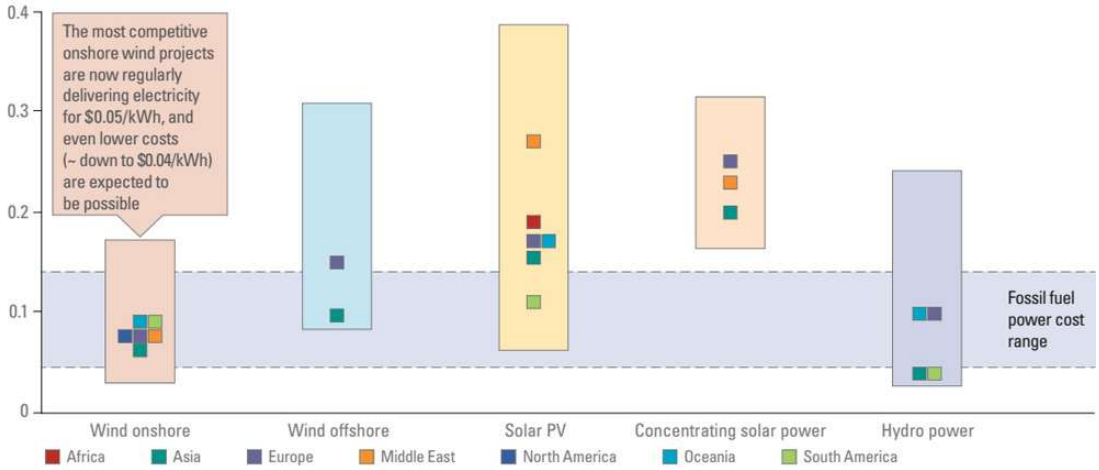

Note: Regional LCOE estimates for renewables are weighted averages in $2014 USD/kWh$.

Figure A.1.2: Levelized cost of energy (LCOE) for wind power compared to other technologies [123]

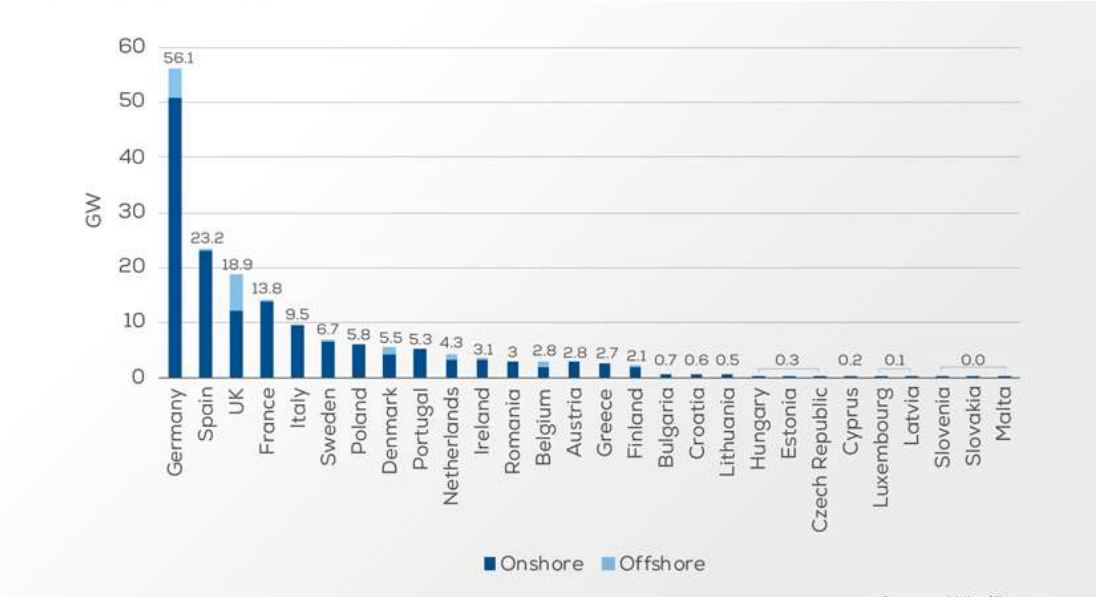

About 60% of UK installed wind power capacity is onshore, meeting over 8% of UK annual power demand. Cummulative onshore and offshore wind power capacity (18.9 GW) meets 13.5% of UK annual power demand. In 2017, UK holds over 3% of global installed wind power capacity.

Figure A.1.3: Cummulative installed wind power capacity in Europe [124]

Appendix A.2

Appendix to Chapter 9

A.2.1 Turbine layout at Braes of Doune wind farm

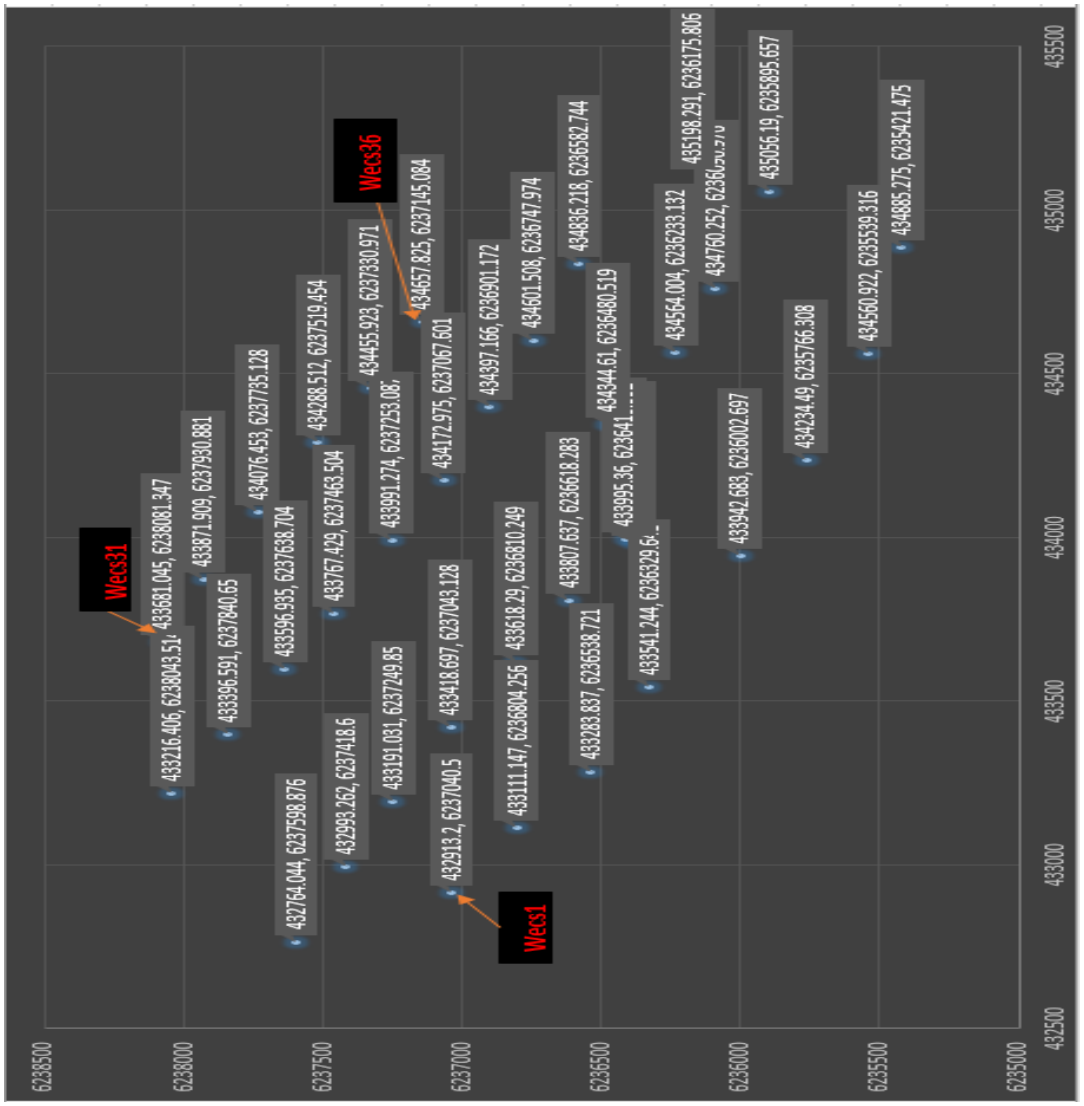

Figure A.2.1: Turbine layout co-ordinates based on UTM system

A.2.2 Technical specification sheet for Vestas wind turbine

V80-2.0 MW
Facts and figures

POWER REGULATION pitch regulated with variable speed

OPERATING DATA

Rated power	2,000 kW
Cut-in wind speed	4.0 m/s
Rated wind speed	16 m/s
Cut-out wind speed	25 m/s
Wind class	IEC IA and IEC IIA
Operating temperature range	-20°C to 40°C low temperature turbine: -30°C to 40°C

ROTOR

Rotor diameter	80 m
Swept area	5,027 m²
Operating temperature range	-20°C to 40°C low temperature turbine: -30°C to 40°C

ROTOR

Rotor diameter	80 m
Swept area	5,027 m²
Air brake	full blade feathering with 3 pitch cylinders

ELECTRICAL

Frequency	50/60 Hz
Generator type	4-pole doubly fed generator, slip rings

GEARBOX

Type	one planetary stage and two helical stages

SOUND POWER

4 m/s 94.0
5 m/s 99.3
6 m/s 103.0
7 m/s 104.5
8 m/s 105.2

Mode 0, 10 m above ground, hub height 80 m, air density 1,225 kg/m³

TOWER

Type	tubular steel tower
Hub heights	60 m, 67 m and 78 m (IEC IA) 60 m, 67 m, 80 m and 100 m (IEC IIA) 100 m (DIBt)

BLADE DIMENSIONS

Length	39 m
Max. chord	3.5 m

NACELLE DIMENSIONS

Height for transport	4 m
Height installed (incl. CoolerTop®)	5.4 m
Length	10.4 m
Width	3.4 m

NACELLE DIMENSIONS

Height for transport	4 m
Height installed (incl. CoolerTop®)	5.4 m
Length	10.4 m
Width	3.4 m

HUB DIMENSIONS

Max. diameter	3.3 m
Max. width	4 m
Length	4.2 m

Max. weight per unit for transportation	70 metric tonnes

Figure A.2.2: Specification sheet for Vestas V80 wind turbine

A.2.3 Digital terrain model for Braes of Doune wind farm

```
WindSim version    : 470

area name          : WindExpress27062017

#nodes nxp nyp     :          328         344

co-ordinate system :            3

ext. xmin xmax     : 427764.044 440194.356
ext. ymin ymax     : 6230231.992 6243270.515
ext. zmin zmax     :         20.6       664.4

extgeo. minx maxx  : -4.168188 -3.964252
extgeo. miny maxy  : 56.211522 56.330375

Horizontal datum   : WGS84
Projection         : UTM
Zone               : 30
Source terrain     : ASTER GDEM v2 Worldwide Elevation Data (1 arc-second Resolution)

Source roughness   : CORINE Land Cover Europe 2006 (100 m Resolution)

HEIGHT             :
         1
        64.41       63.284       72.289        73.23       71.878       69.901       61.915       57.358       53.405       56.007
       66.957       65.177       64.598       65.301       64.761       61.731       55.846       52.881       53.431       54.683
       58.334       57.281       59.684       63.309       69.099       66.125       62.043       62.521       58.489       53.648
       45.105       46.061       40.263       46.034       55.499       71.793       64.062       45.774       32.696       20.966
       20.596       23.425       26.719       33.367       41.206       49.392       50.301       53.578       56.746       58.616
        62.23       64.386       65.334       66.421       68.301       69.893       71.936       72.941       73.651       73.238
       72.226       69.619       70.057        74.25       75.417        80.56       80.385       76.418       74.968       73.212
       71.977       71.994       76.743       80.309       79.681       78.992       83.437       87.958       90.134       86.222
         77.6       73.073       72.768       75.256       75.285       76.299       83.816       92.161      103.843      102.268

ROUGHNESS          :
         1
  0.0010000000 0.0010000000 0.0010000000 0.0010000000 0.0010000000 0.0010000000 0.0010000000 0.0010000000 0.0010000000 0.0010000000
  0.0010000000 0.0010000000 0.0010000000 0.0010000000 0.0010000000 0.0010000000 0.0010000000 0.0010000000 0.0010000000 0.0010000000
  0.0010000000 0.0010000000 0.0010000000 0.0010000000 0.0010000000 0.0010000000 0.0010000000 0.0010000000 0.0010000000 0.0010000000
  0.0010000000 0.0010000000 0.0010000000 0.0010000000 0.0010000000 0.0010000000 0.0010000000 0.0010000000 0.0010000000 0.0010000000
  0.0010000000        0.389          1.4        1.313        0.065 0.0010000000 0.0010000000 0.0010000000 0.0010000000 0.0010000000
  0.0010000000 0.0010000000 0.0010000000 0.0010000000 0.0010000000 0.0010000000 0.0010000000 0.0010000000 0.0010000000 0.0010000000
  0.0010000000 0.0010000000 0.0010000000 0.0010000000 0.0010000000 0.0010000000 0.0010000000 0.0010000000 0.0010000000 0.0010000000
  0.0010000000 0.0010000000 0.0010000000 0.0010000000 0.0010000000 0.0010000000 0.0010000000 0.0010000000 0.0010000000 0.0010000000
  0.0010000000 0.0010000000 0.0010000000 0.0010000000 0.0010000000 0.0010000000 0.0010000000 0.0010000000 0.0010000000 0.0010000000
  0.0010000000 0.0010000000 0.0010000000 0.0010000000 0.0010000000 0.0010000000 0.0010000000 0.0010000000 0.0010000000 0.0010000000
  0.0010000000 0.0010000000 0.0010000000 0.0010000000 0.0010000000 0.0010000000        0.265        0.922        0.843        0.038
  0.0010000000 0.0010000000 0.0010000000 0.0010000000 0.0010000000 0.0010000000 0.0010000000 0.0010000000 0.0010000000 0.0010000000
  0.0010000000 0.0010000000 0.0010000000 0.0010000000 0.0010000000 0.0010000000 0.0010000000 0.0010000000 0.0010000000 0.0010000000
        0.326        0.446        0.427        0.255 0.0010000000 0.0010000000 0.0010000000 0.0010000000 0.0010000000 0.0010000000
  0.0010000000 0.0010000000 0.0010000000         0.42          1.4          1.4          1.4          1.4          1.4          1.4
          1.4          1.4          1.4          1.4        1.234 0.0010000000 0.0010000000 0.0010000000 0.0010000000 0.0010000000
  0.0010000000 0.0010000000 0.0010000000 0.0010000000 0.0010000000 0.0010000000 0.0010000000 0.0010000000 0.0010000000 0.0010000000
  0.0010000000 0.0010000000 0.0010000000 0.0010000000 0.0010000000 0.0010000000        1.048          1.4          1.4          1.4
          1.4        1.106 0.0010000000 0.0010000000 0.0010000000 0.0010000000 0.0010000000 0.0010000000 0.0010000000 0.0010000000
  0.0010000000 0.0010000000 0.0010000000 0.0010000000 0.0010000000 0.0010000000 0.0010000000 0.0010000000 0.0010000000 0.0010000000
  0.0010000000 0.0010000000 0.0010000000 0.0010000000 0.0010000000 0.0010000000 0.0010000000        0.421        0.721 0.0010000000
  0.0010000000 0.0010000000 0.0010000000 0.0010000000 0.0010000000 0.0010000000 0.0010000000 0.0010000000 0.0010000000 0.0010000000
  0.0010000000 0.0010000000 0.0010000000 0.0010000000 0.0010000000 0.0010000000 0.0010000000 0.0010000000 0.0010000000 0.0010000000
  0.0010000000 0.0010000000 0.0010000000 0.0010000000 0.0010000000 0.0010000000 0.0010000000 0.0010000000 0.0010000000 0.0010000000
  0.0010000000 0.0010000000 0.0010000000 0.0010000000 0.0010000000 0.0010000000 0.0010000000 0.0010000000 0.0010000000 0.0010000000
  0.0010000000 0.0010000000 0.0010000000 0.0010000000 0.0010000000 0.0010000000 0.0010000000 0.0010000000 0.0010000000 0.0010000000
  0.0010000000 0.0010000000 0.0010000000 0.0010000000 0.0010000000 0.0010000000 0.0010000000 0.0010000000 0.0010000000 0.0010000000
  0.0010000000 0.0010000000 0.0010000000 0.0010000000 0.0010000000 0.0010000000 0.0010000000 0.0010000000        0.979        1.239
        1.145        1.163        1.181        1.006 0.0010000000 0.0010000000 0.0010000000 0.0010000000 0.0010000000 0.0010000000
  0.0010000000        0.422          1.4          1.4          1.4        0.181 0.0010000000 0.0010000000 0.0010000000 0.0010000000
```

Figure A.2.3: Terrain elevation and roughness length

A.2.4 R codes for cleaning WRF and ELEXON datasets

```
R code for cleaning the entire wrf dataset from 2000 - 2010.
outlier screening for braes of doune wrf dataset
Abdulmutalib yussuff
Friday, july 28, 2017

1.      load library
library("ggplot2", lib.loc="~/r/win-library/3.4")
2.      import data files
setwd("c:/users/abdul2/desktop/resources/my work/rstudio")
data.raw<-read.csv(file="tsdata_braesofdunecsv.csv",header=true)
view(data.raw)
3.      assign compatible column names
new.names<-c("date_time","direction_deg.","windspeed_mps", "power_norm")
4.      check new names
cbind(names(data.raw),new.names)
##                                  new.names
## [1,] "datetime..yyyy.mm.dd..hr.00." "date_time"
## [2,] "direction..deg.."             "direction_deg."
## [3,] "speed..m.s."                  "windspeed_mps"
## [4,] "power_norm"                   "power_norm"
5.      replace columns name
names(data.raw)<-new.names
6.      new data set to work with
data <- data.raw
view(data)
summary(data)
##   date_time         direction_deg.  windspeed_mps      power_norm
##  length:96419       min.   :  0.0   min.   : 0.0421   min.   :0.0000
##  class :character   1st qu.:133.0   1st qu.: 4.7580   1st qu.:0.0349
##  mode  :character   median :221.0   median : 7.1957   median :0.1684
##                     mean   :200.7   mean   : 7.5339   mean   :0.3177
##                     3rd qu.:265.0   3rd qu.: 9.9030   3rd qu.:0.5785
##                     max.   :359.0   max.   :27.1288   max.   :1.0000
##                     na's   :216     na's   :216       na's   :216
search for missing values
check<-function(data){}
7.      count na (total missing values)
nas<-sum(is.na(data))
print(paste("missing values:", nas))
## [1] "missing values: 648"
8.      count incomplete dataset
ok<-complete.cases(data)
```

```
R code for cleaning the elexon and wrf dataset from 2009 - 2010.
R code for sorting elexon and wrf datasets
Abdulmutalib yussuff
August 12, 2017

13.     import elexon_wrf dataset and do summary statistics
setwd("c:/users/abdul2/desktop/resources/my work/rstudio")
elexon_wrf<-read.csv(file="elexon_and_wrf.csv",header=true)
view(elexon_wrf)
summary (elexon_wrf)
##  period.start          elexon             wrf
##  length:17520       min.   :-0.00818   min.   :0.0000
##  class :character   1st qu.: 0.01676   1st qu.:0.0292
##  mode  :character   median : 0.12486   median :0.1411
##                     mean   : 0.23395   mean   :0.2862
##                     3rd qu.: 0.36743   3rd qu.:0.5065
##                     max.   : 0.96480   max.   :1.0000
##                     na's   :243        na's   :243
14.     check for missing values
check<-function(elexon_wrf){}
15.     count na (total missing values)
nas<-sum(is.na(elexon_wrf))
print(paste("missing values:", nas))
## [1] "missing values: 486"
16.     count incomplete records (rows containing missing values)
ok<-complete.cases(elexon_wrf)
sum(ok)
## [1] 17277
print(paste("incomplete records:", sum(!ok)))
## [1] "incomplete records: 243"
17.     show incomplete records (if less than 100 nas).
if(nas > 0 & nas <= 100) print( elexon_wrf[which(! complete.cases(elexon_wrf)),
18.     if more than 100, show column-wise distribution of nas.
if (nas > 1) hist(which(is.na(elexon_wrf), arr.ind=true)[,2], xlab="column", fre

remove missing values using 'na.omit' function {stats package} to create a clean
19.     apply the removed function to compare the elexon_wrf dataset frames.
nrow.orig<-nrow(elexon_wrf)[1] # record the dimensions of the elexon_wrf (before
elexon_wrf<-na.omit(elexon_wrf) # omit rows containing missing values
nrow.new<-dim(elexon_wrf)[1] # record the new dimensions of the elexon_wrf (afte
remove(nrow.orig, nrow.new) # check how many records have been removed
summary(elexon_wrf)
```

Figure A.2.4: R codes for pre-processing and cleaning of WRF and ELEXON datasets

A.2.5 MATLAB code for WRF and coupled model data mining

See detailed codes in Github: R and MATLAB CODES DEVELOPED FOR THIS PROJECT

A.2.6 2D velocity map for each sector (0° - 330°) in coupled model

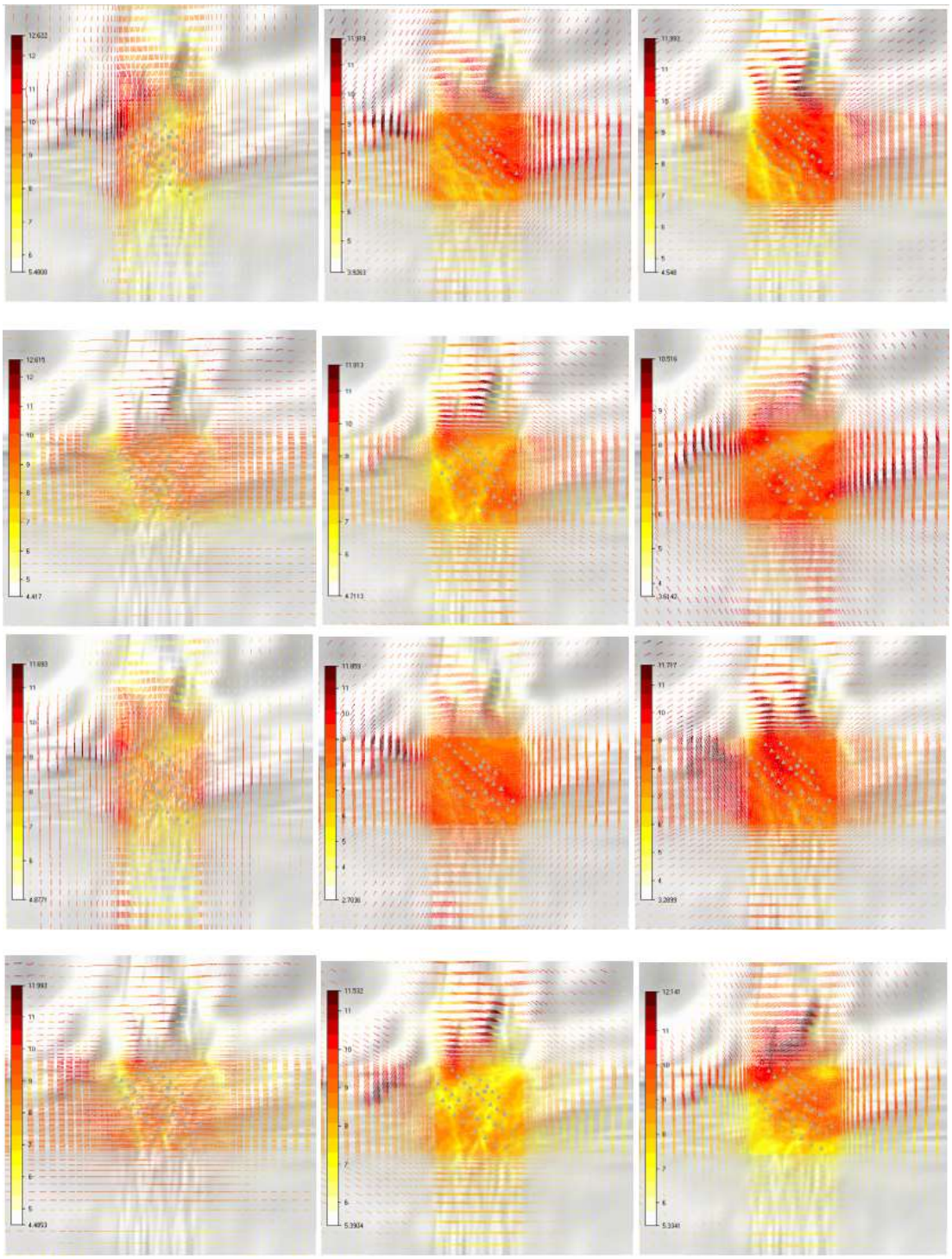

Figure A.2.5: 2D velocity map per sector

A.2.7 Distribution of missing values by column

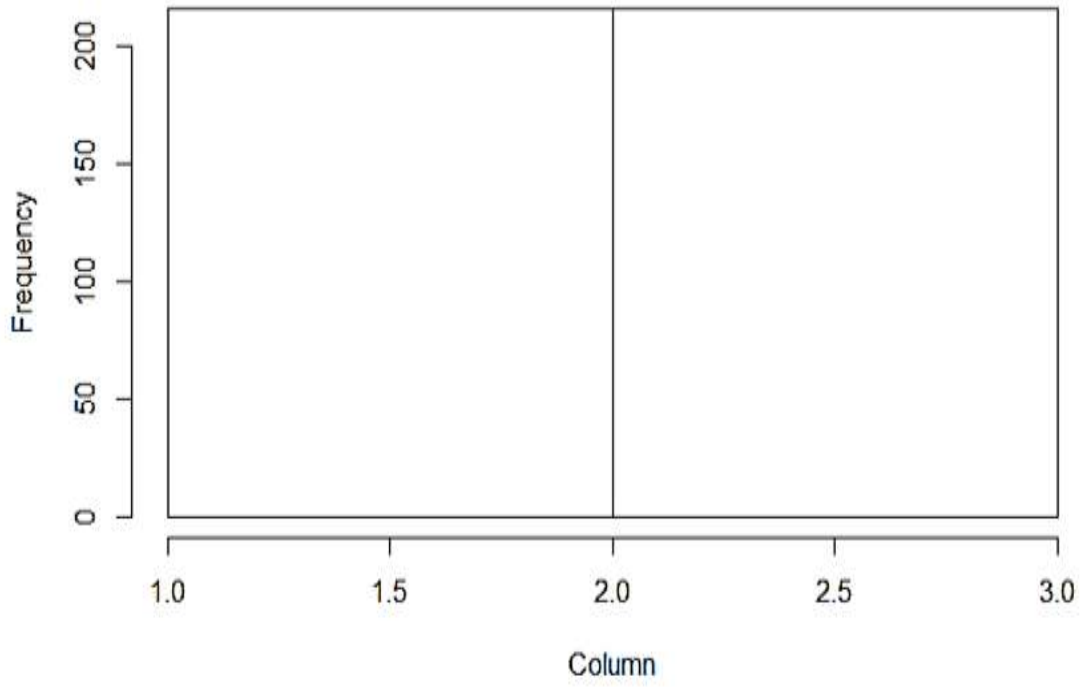

Figure A.2.6: Column-wise distribution of missing values in WRF dataset

A.2.8 Simulation convergence parameters for each wind field sector

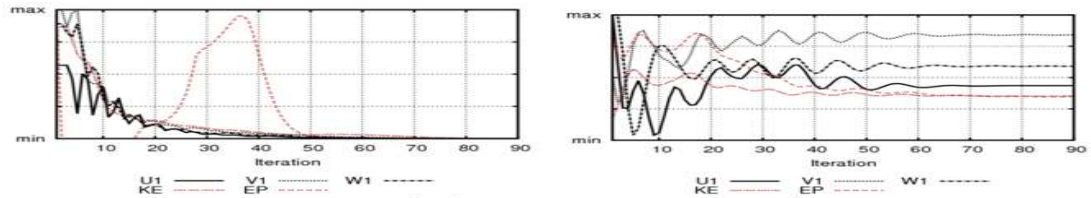

Figure 5.1 Residuals (left) and spot values (right) for sector 000

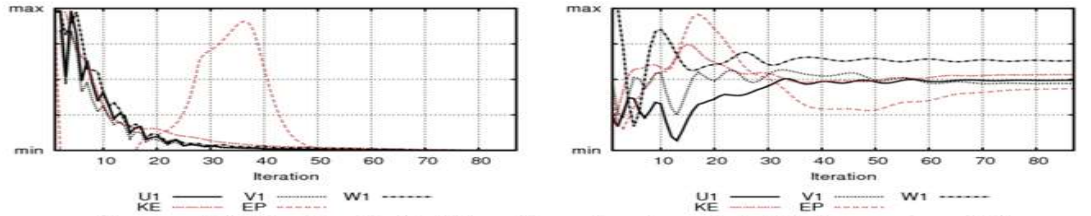

Figure 5.2 Residuals (left) and spot values (right) for sector 030

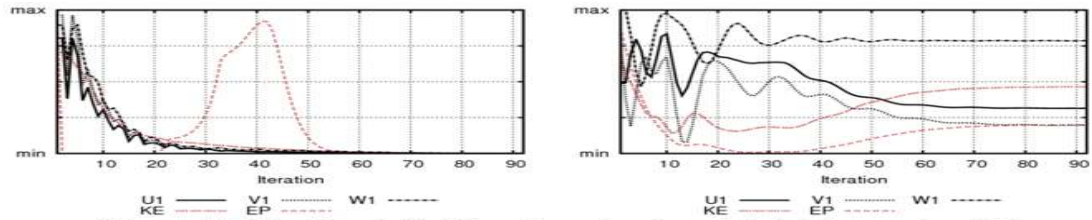

Figure 5.3 Residuals (left) and spot values (right) for sector 060

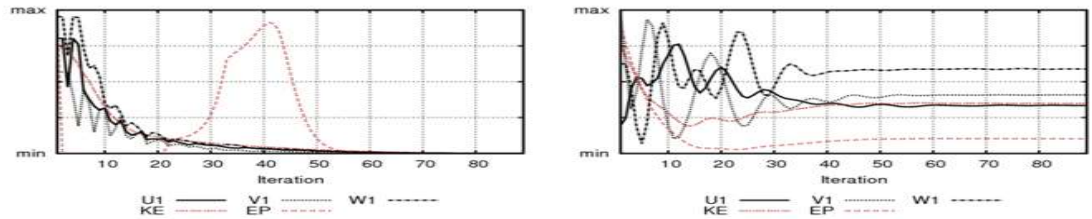

Figure 5.4 Residuals (left) and spot values (right) for sector 090

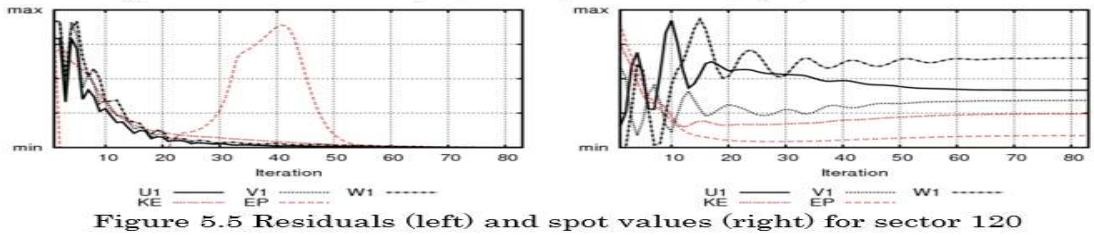

Figure 5.5 Residuals (left) and spot values (right) for sector 120

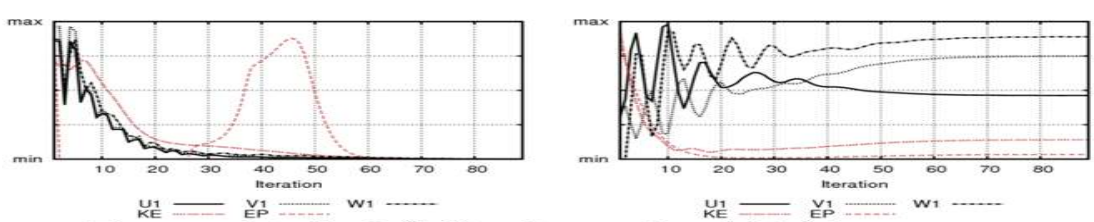

Figure 5.6 Residuals (left) and spot values (right) for sector 150

Figure A.2.7: Simulation convergence parameters, sectors 0°-150°

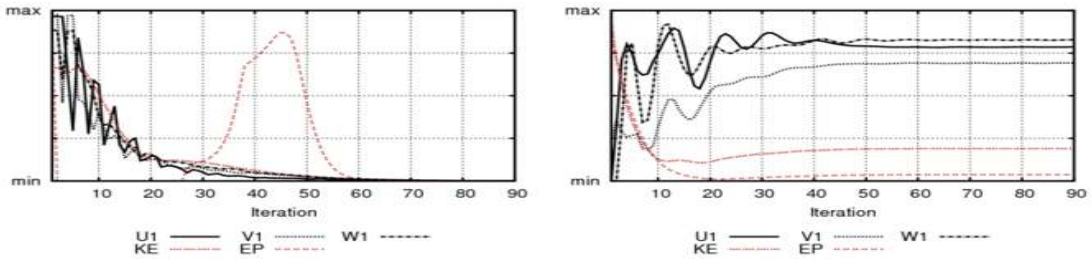

Figure 5.7 Residuals (left) and spot values (right) for sector 180

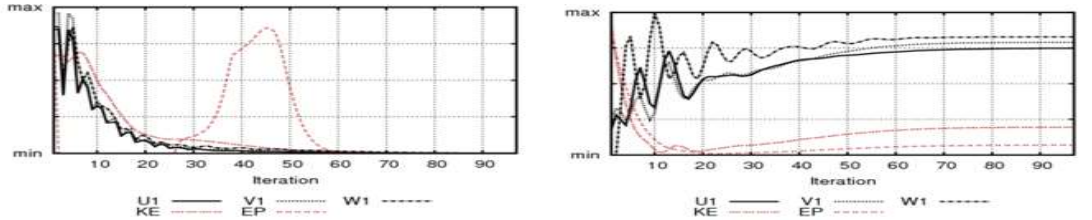

Figure 5.8 Residuals (left) and spot values (right) for sector 210

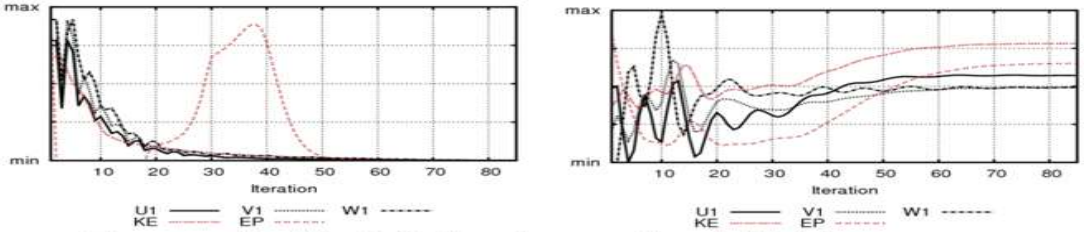

Figure 5.9 Residuals (left) and spot values (right) for sector 240

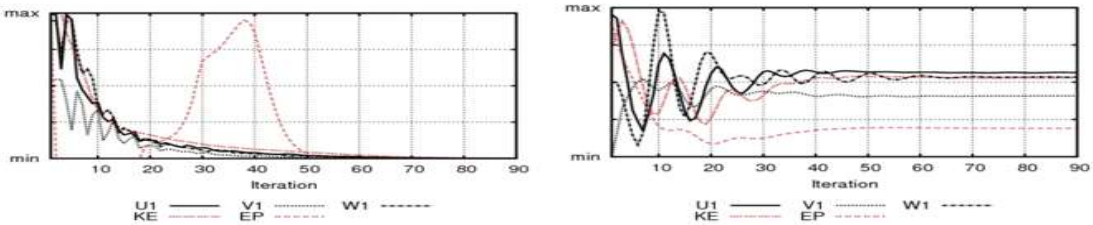

Figure 5.10 Residuals (left) and spot values (right) for sector 270

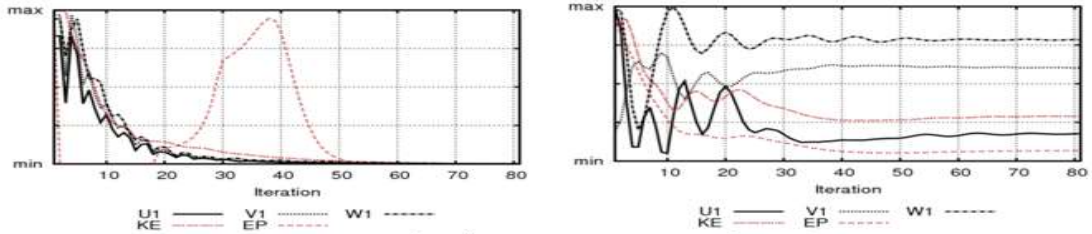

Figure 5.11 Residuals (left) and spot values (right) for sector 300

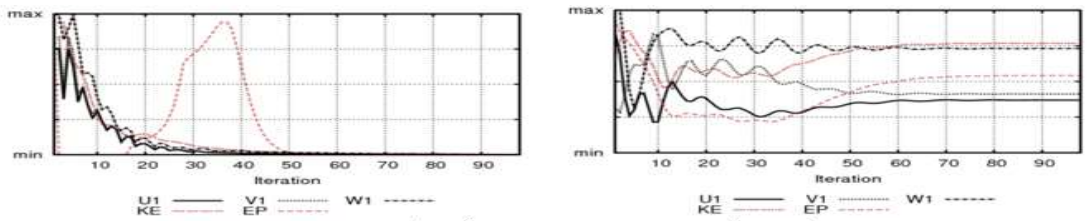

Figure 5.12 Residuals (left) and spot values (right) for sector 330

Figure A.2.8: Simulation convergence parameters, sectors 180°-330°

Appendix A.3

Appendix to Chapter 10

A.3.1 Anisotropy of wind speed profile

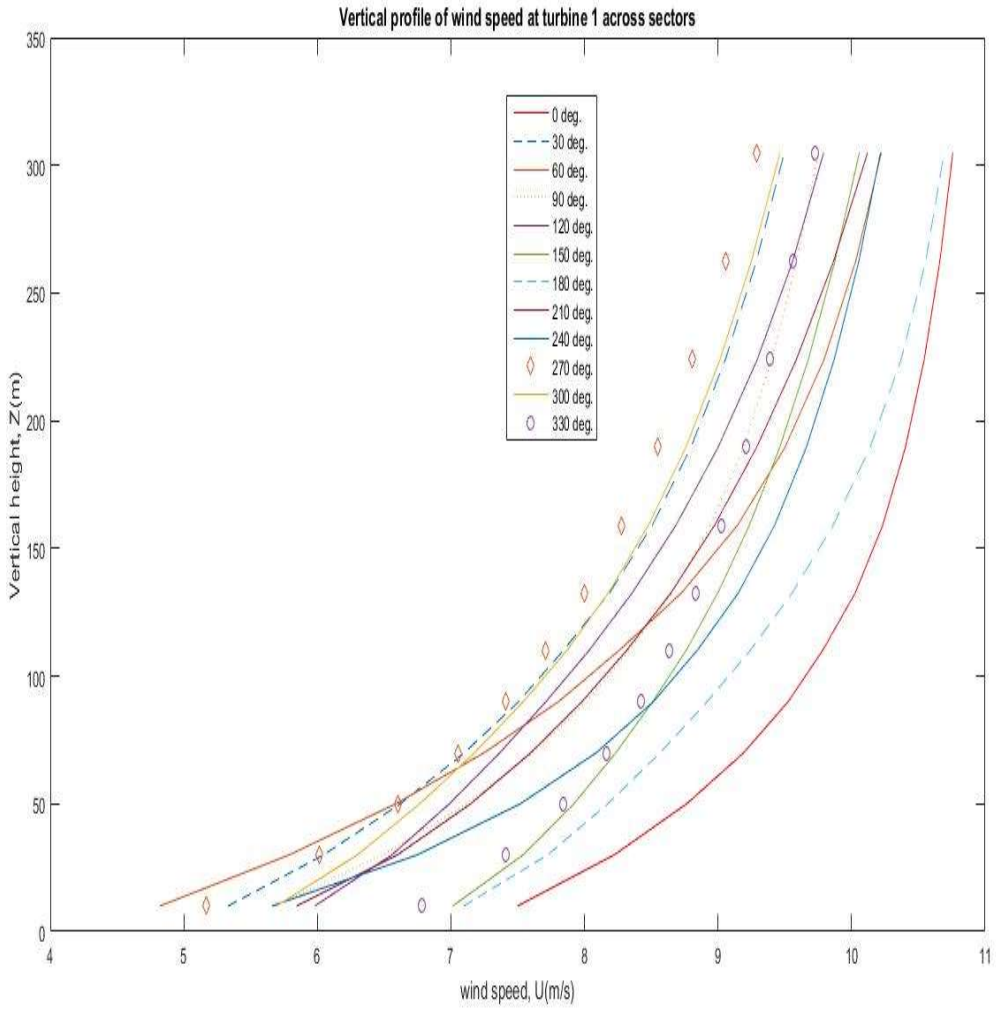

Figure A.3.1: Directional variation of wind speed (U) with vertical height, z(m)

A.3.2 Anisotropy of inflow angle (°) profile

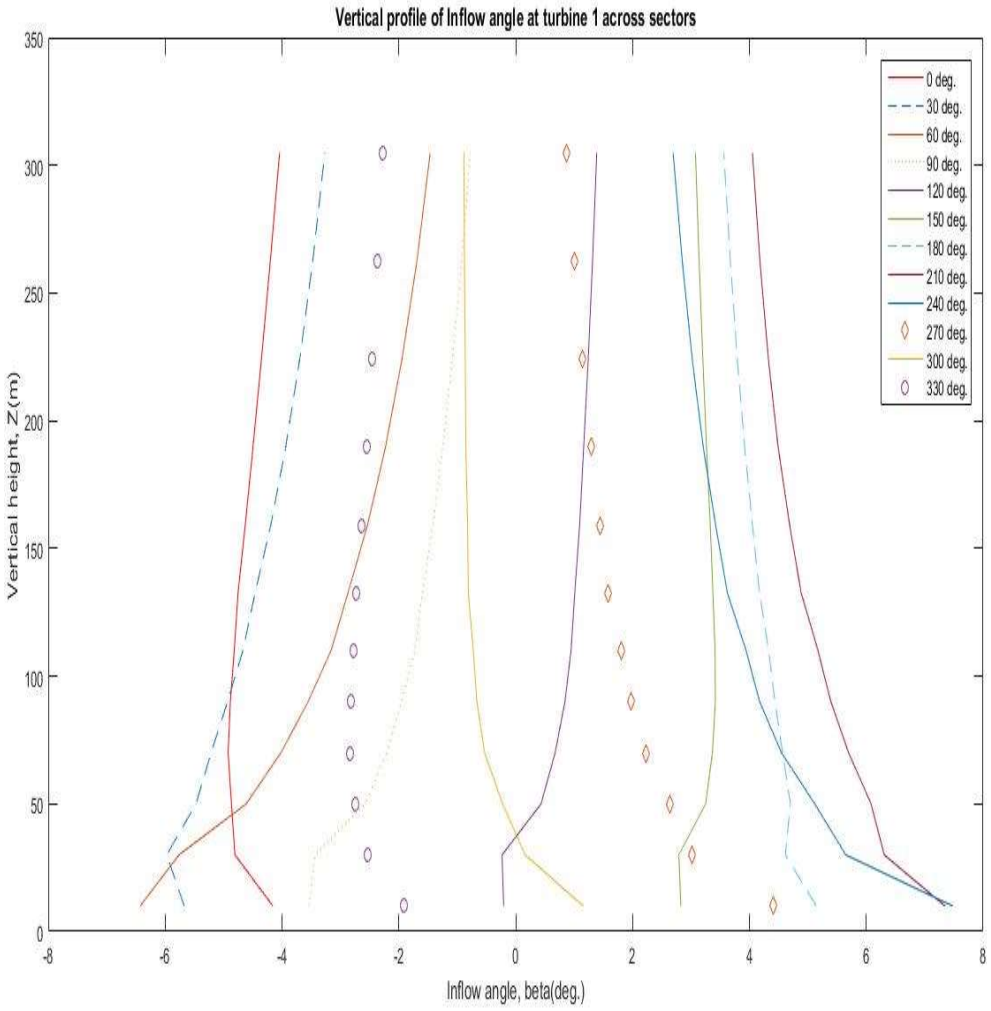

Figure A.3.2: Directional variation of inflow angle (°) with vertical height, z(m)

A.3.3 Anisotropy of wind shear (Ush) profile

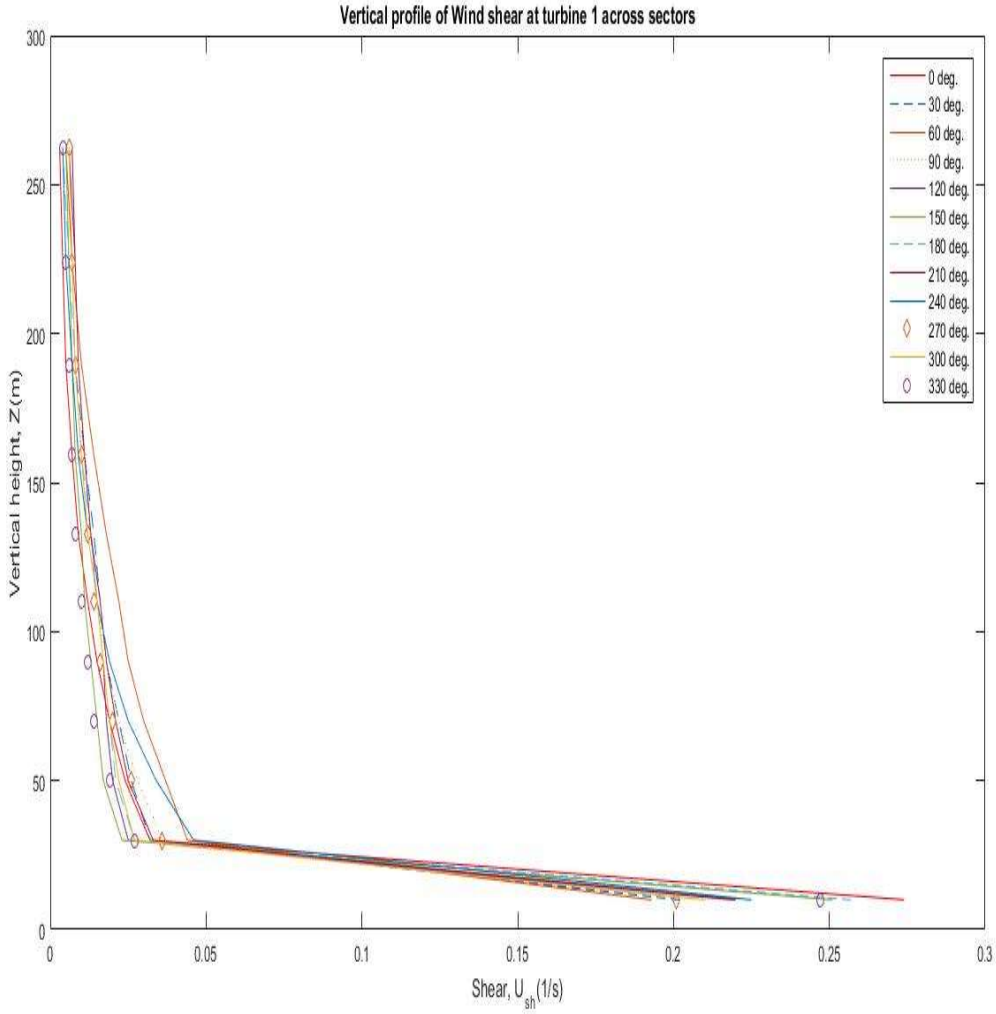

Figure A.3.3: Directional variation of wind shear (Ush) with vertical height, z(m)

A.3.4 Anisotropy of turbulent kinetic energy (TKE) profile

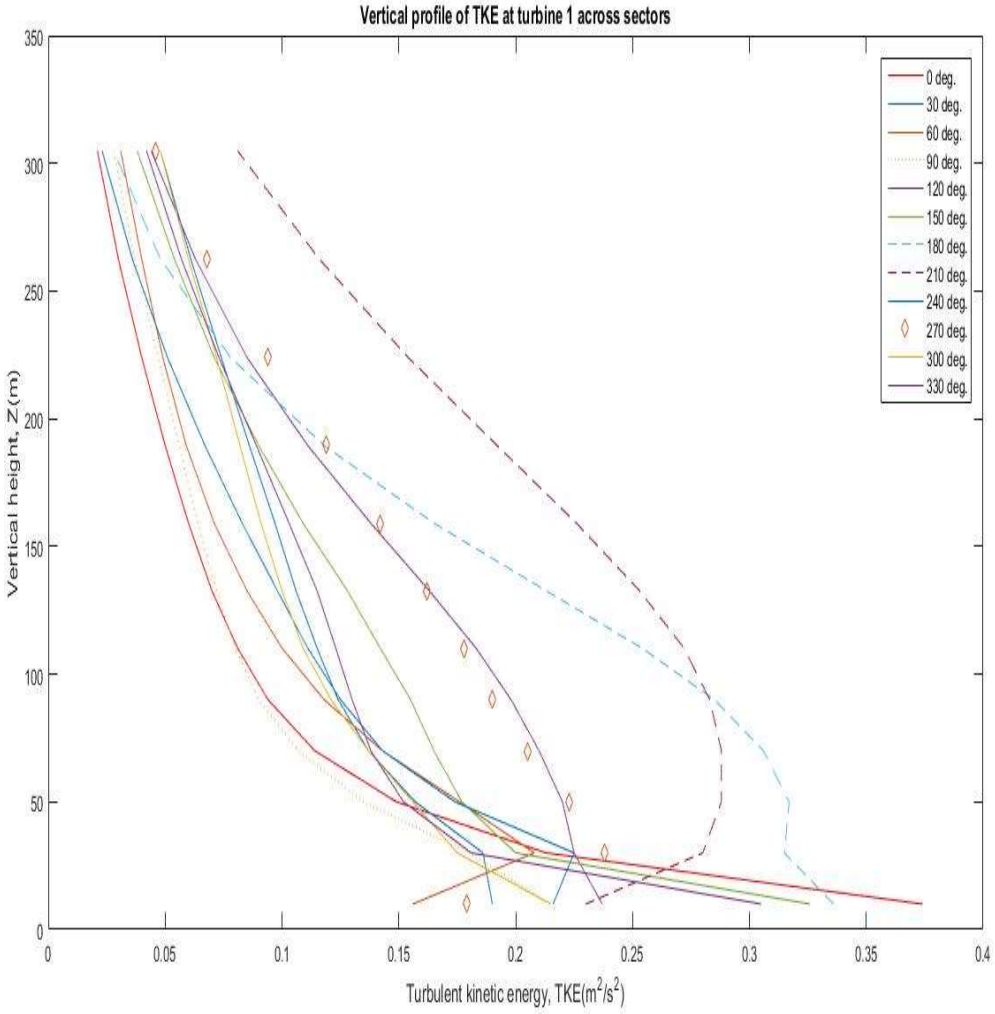

Figure A.3.4: Directional variation of turbulent kinetic energy (TKE) with vertical height, z(m)

A.3.5 Anisotropy of turbulence intensity (TI) profile

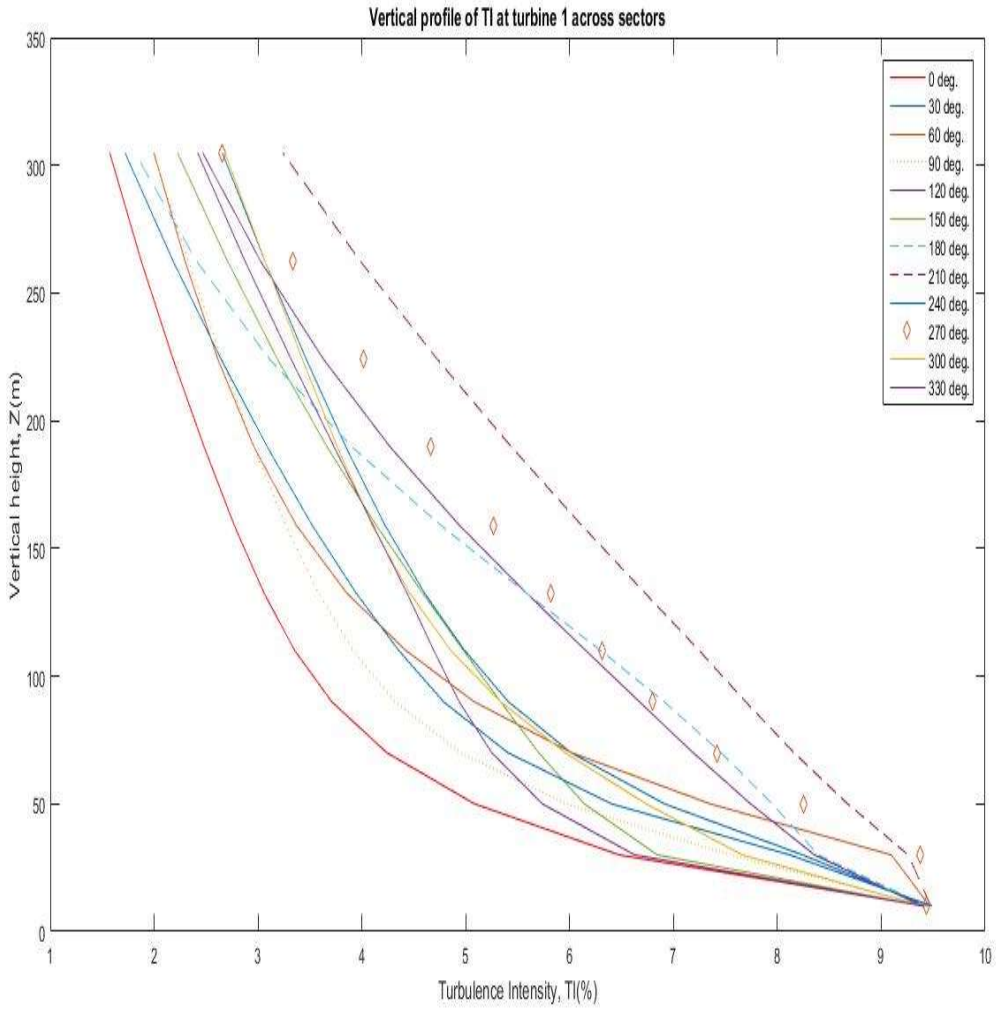

Figure A.3.5: Directional variation of turbulence intensity (TI) with vertical height, z(m)

A.3.6 Anisotropy of wind shear exponent profile

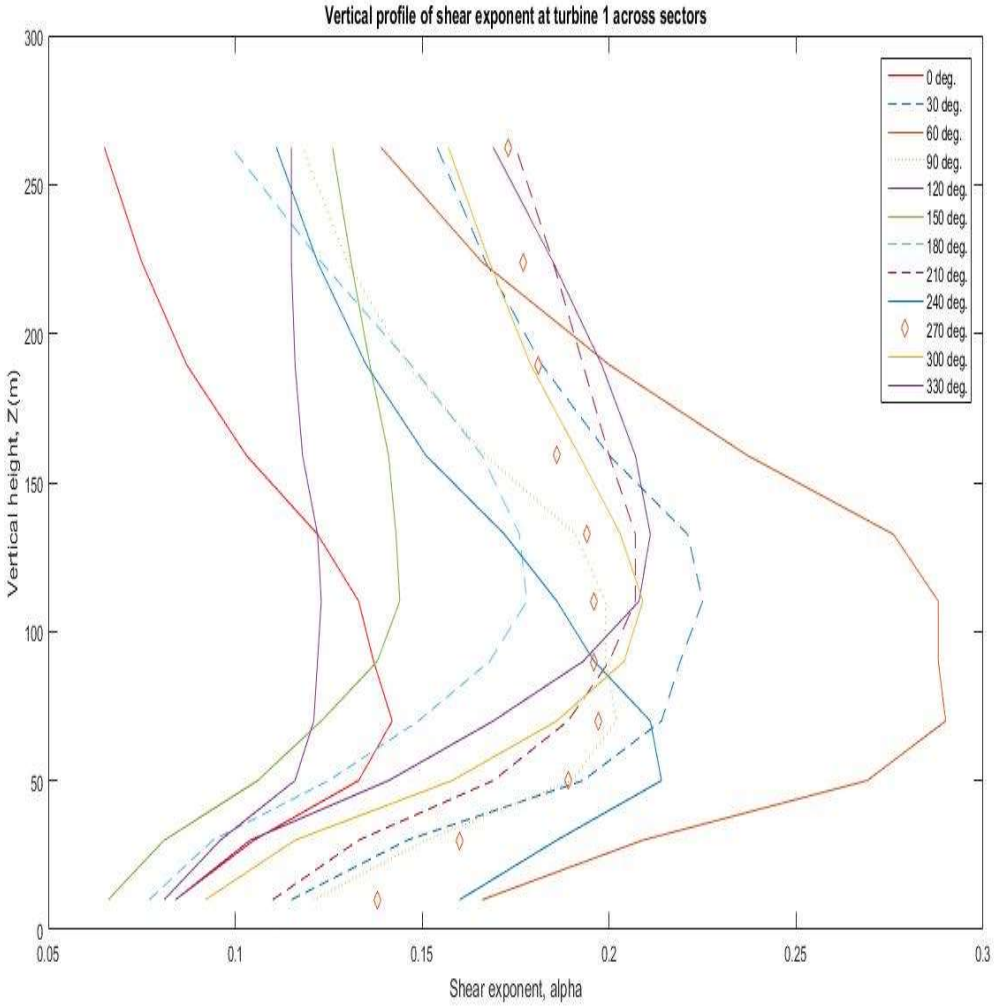

Figure A.3.6: Directional variation of wind shear exponent with vertical height, z(m)

A.3.7 Anisotropy of TI-wind speed (U) interaction

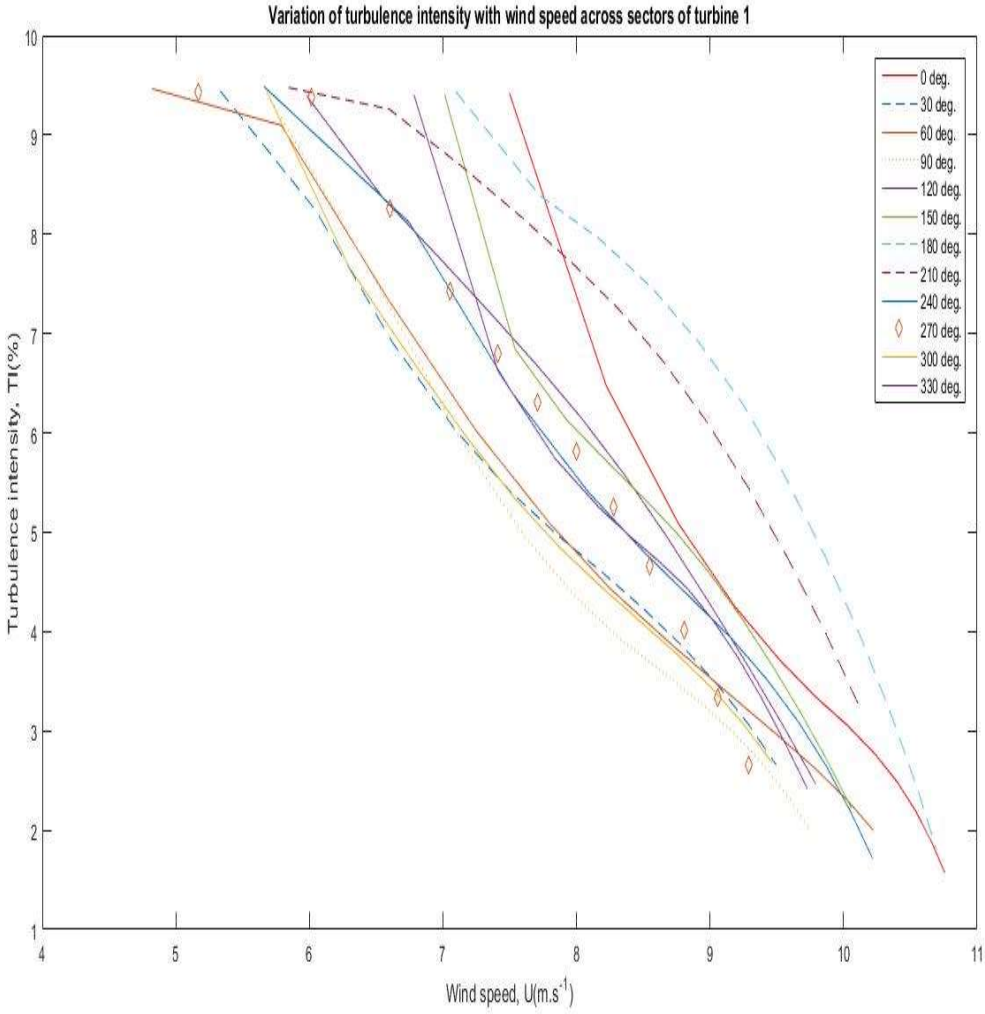

Figure A.3.7: Directional variation of TI (%) with wind speed, U (m/s)

A.3.8 Inclination of the complex terrain at Braes of Doune wind farm

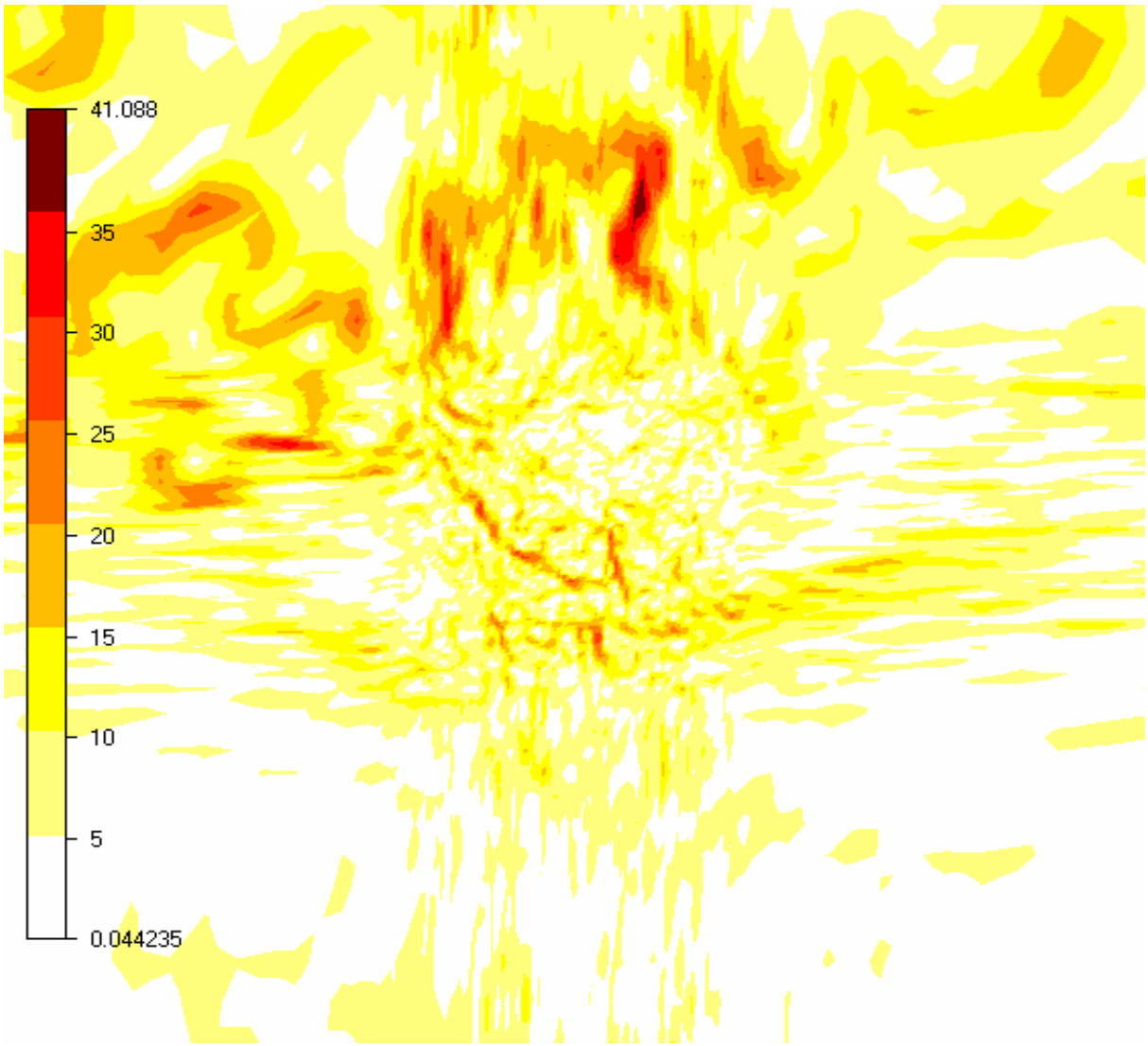

Figure A.3.8: 3D terrain inclination map showing angles in degree

A.3.9 Weibull distribution of wind speed

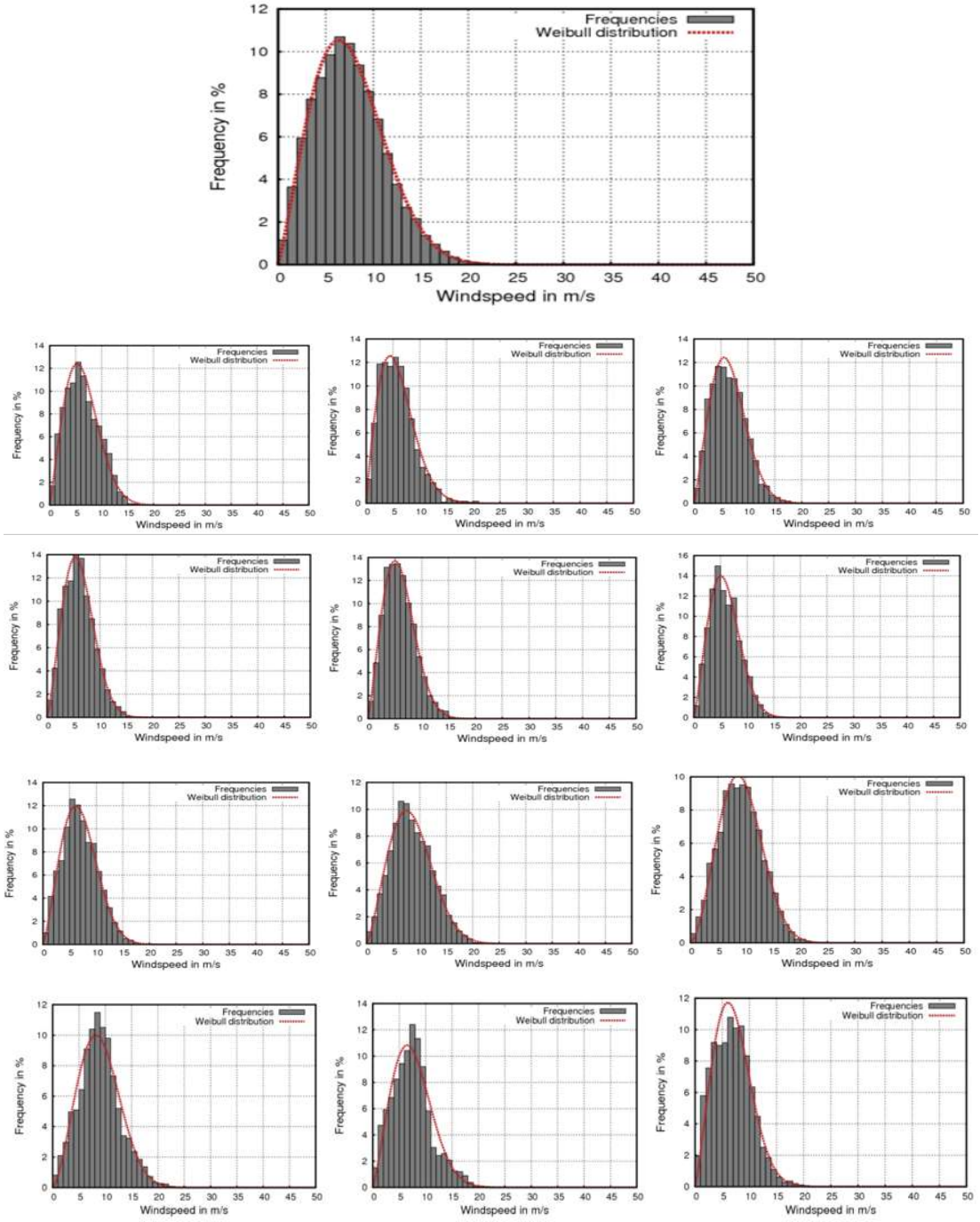

Top: All sectors; and Bottom (L-R): 0-30°, 30-60°,...330-360° sectors

Figure A.3.9: Weibull distribution of wind speed for: All sector (top); and 0°-360° sectors (L-R)

A.3.10 Wind roses for the coupled model wind speed

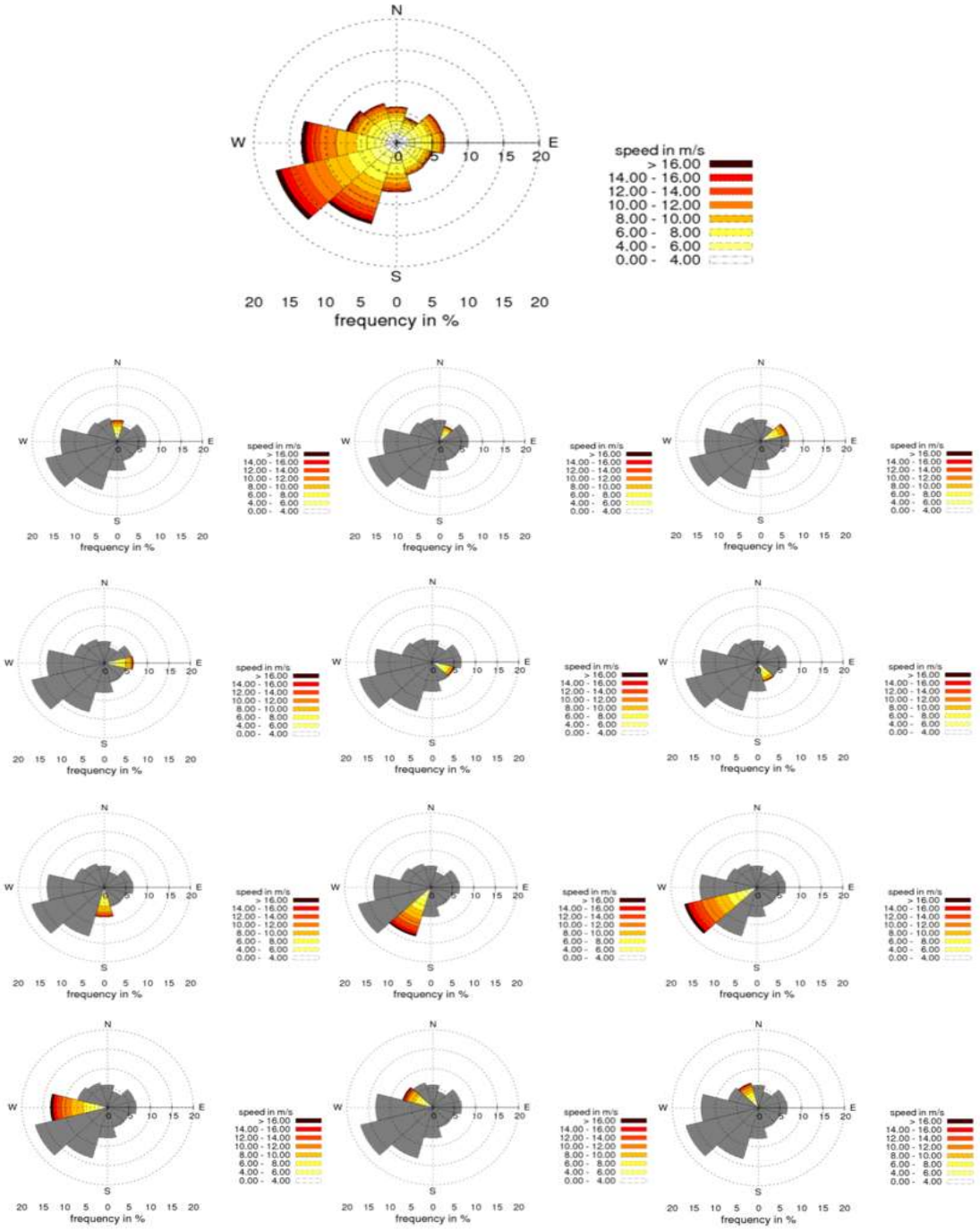

Top: All sectors; and Bottom (L-R): 0-30°, 30-60°,...330-360° sectors

Figure A.3.10: Wind rose for coupled model for: All sector (top); and 0°-360° sectors (L-R)

A.3.11 Variation of wind density over Braes of Doune wind farm

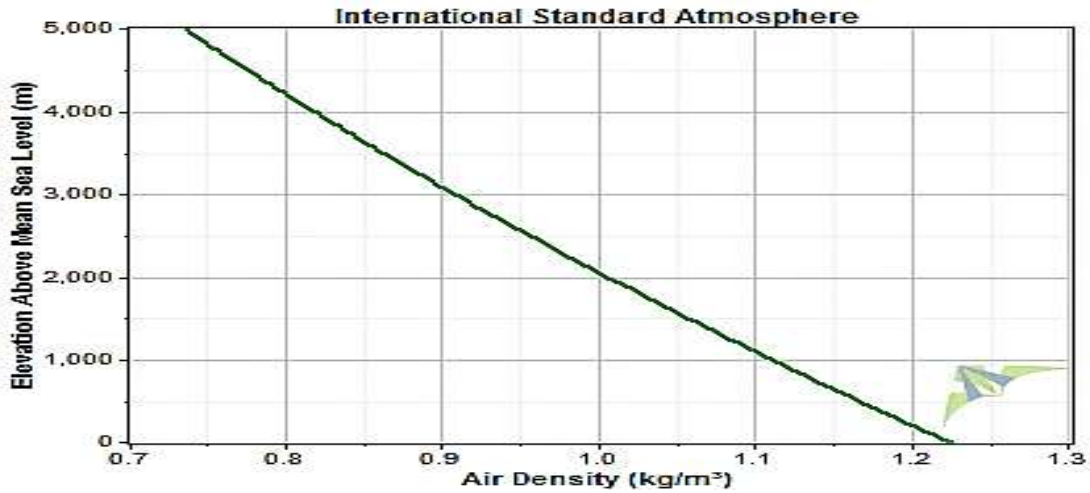

Figure A.3.11: Wind density

A.3.12 Monthly distribution of wind speed frequency (2000 – 2010)

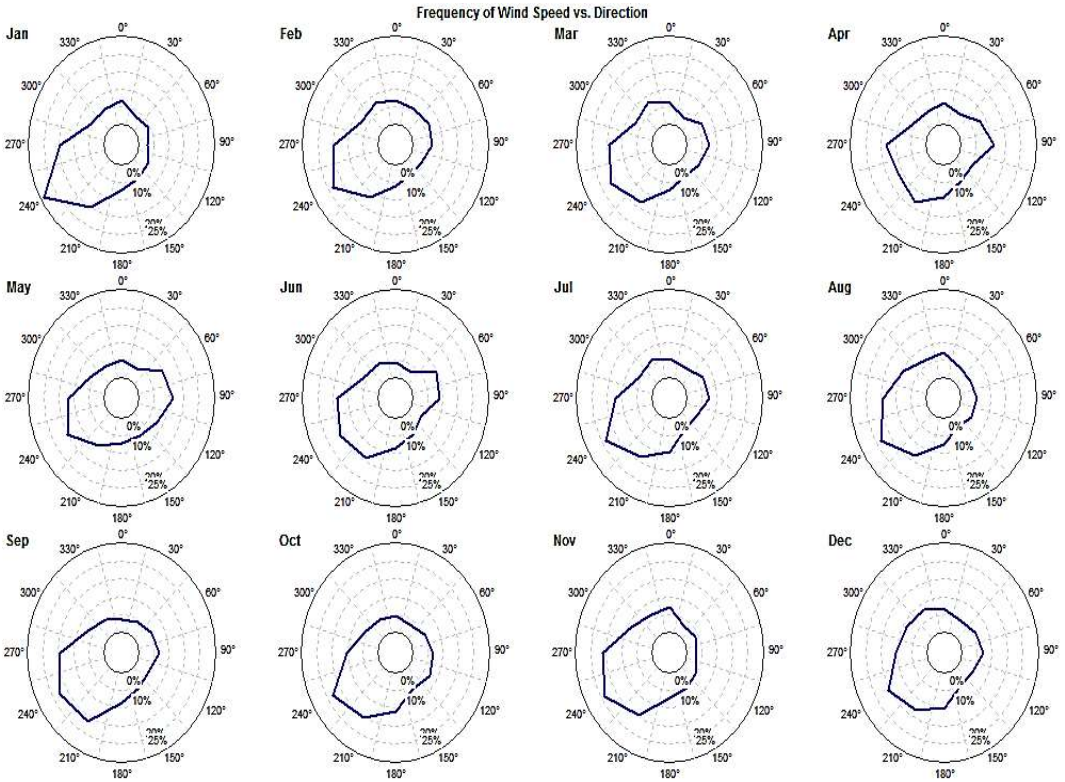

Figure A.3.12: Monthly distribution of wind speed frequency per sector - WRF

A.3.13 Local wind climate at Braes of Doune wind farm

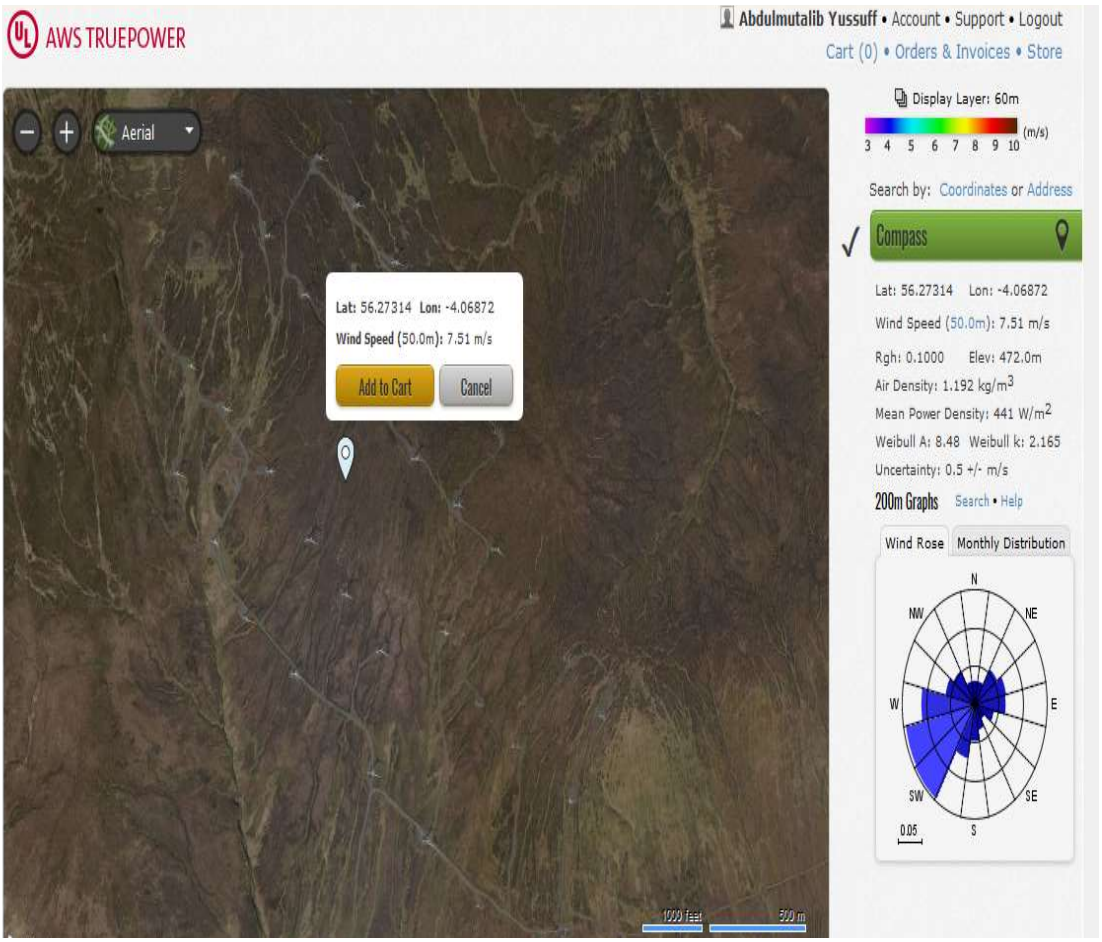

Figure A.3.13: Reference wind climate at Braes of Doune wind farm - Windographer

A.3.14 Input variables for calculating analytical wake models

Wake model	Upstream wind speed	Downstream spacing	Radial spacing	Induction factor	Rotor diameter	Hub height	Turbulence intensity	Roughness length
Jensen	✓	✓		✓	✓	✓		✓
Larsen	✓	✓	✓	✓	✓	✓	✓	
Ishihara	✓	✓	✓	✓	✓		✓	
Frandsen	✓	✓		✓	✓			

Figure A.3.14: Required inputs for each analytical wake models [83]

A.3.15 Wind farm zoning by wake-adjusted wind speed

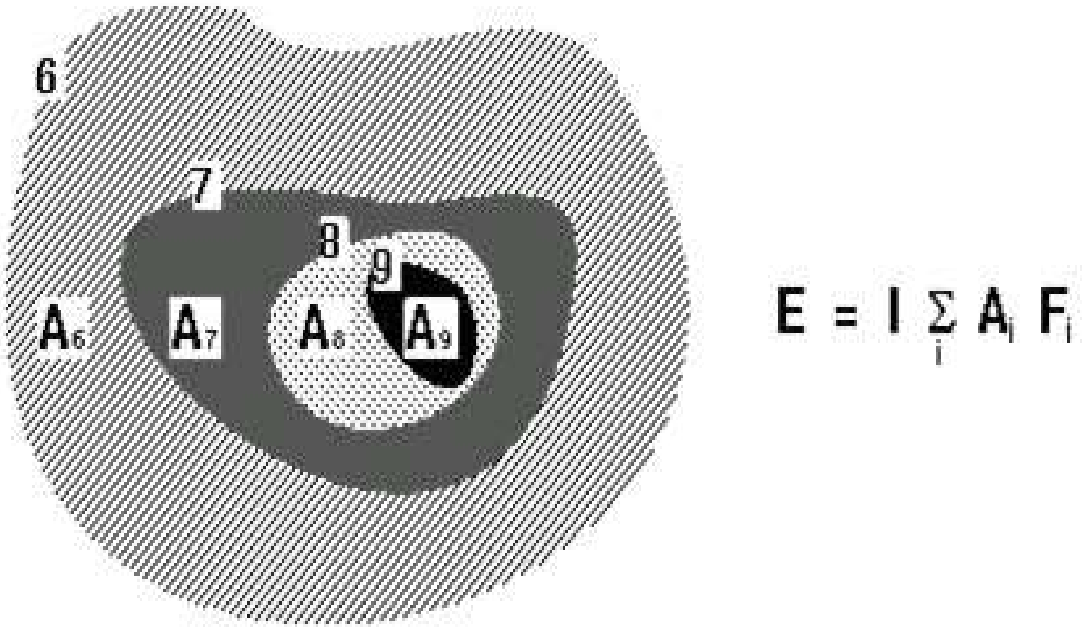

Figure A.3.15: Area for energy yield estimation

A.3.16 Performance of analytical wake models at downwind distances

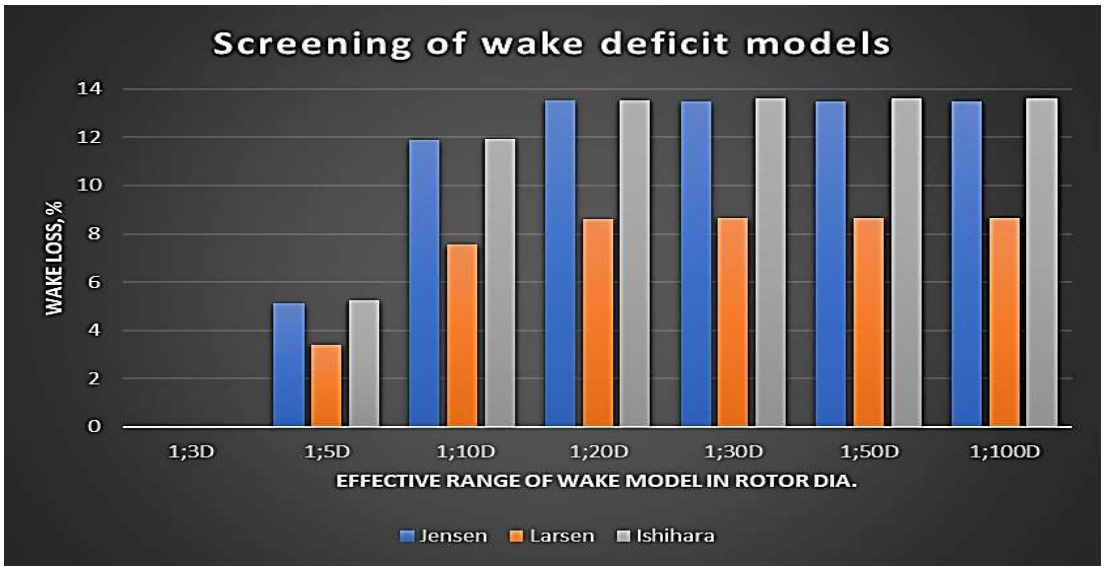

Figure A.3.16: Screening of wake deficit models at selected distances downwind

A.3.17 Turbulence intensity (TI) map at 240° and 270° sectors

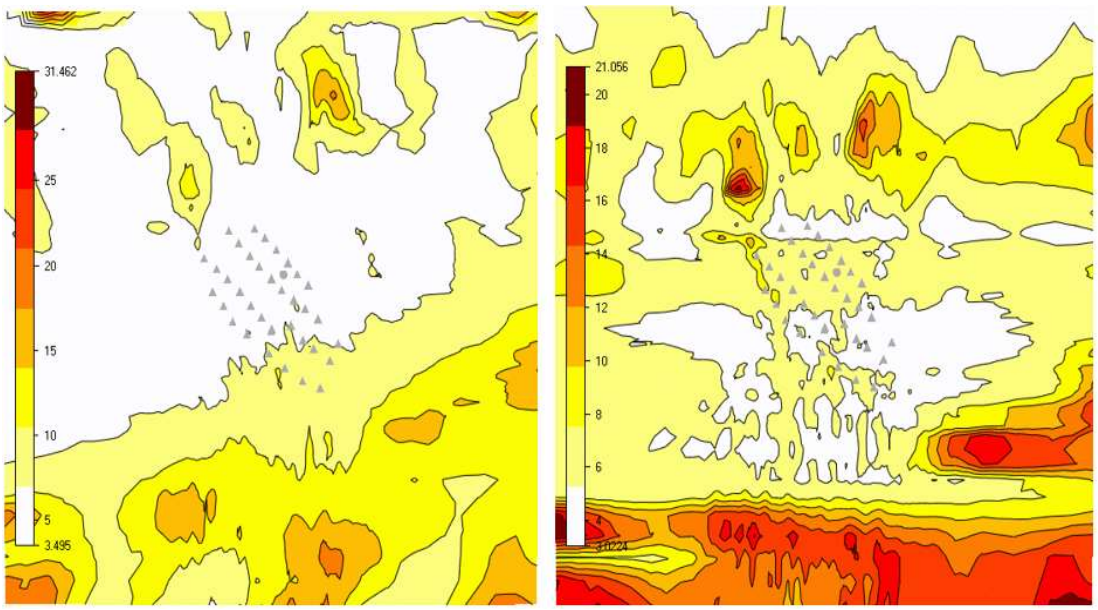

Figure A.3.17: TI map for 240° and 270° sectors (south westerly)

A.3.18 Wind shear map at 240° and 270° sectors

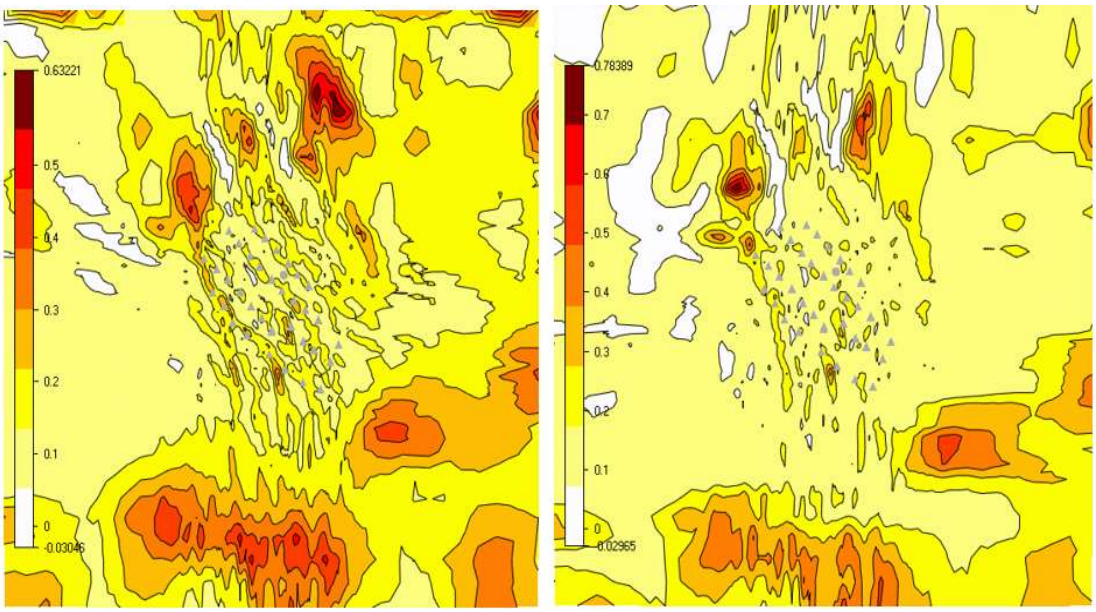

Figure A.3.18: Wind shear map at 240° and 270° sectors (south westerly)

Appendix A.4

Appendix to Chapter 11

A.4.1 Statistical distributions for power output and wind speed

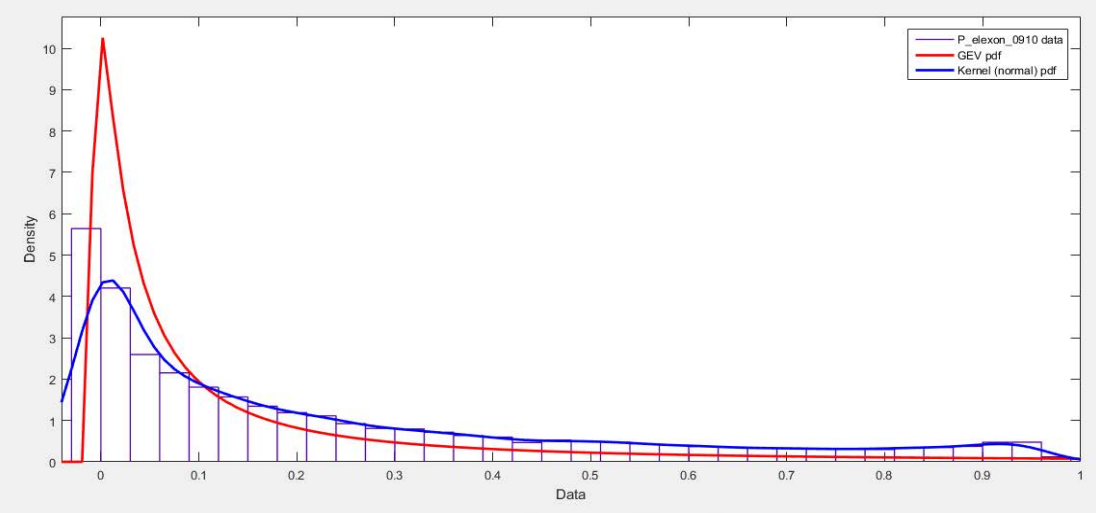

(a) Fitting GEV and Kernel PDFs to actual power production from ELEXON (2009-2010)

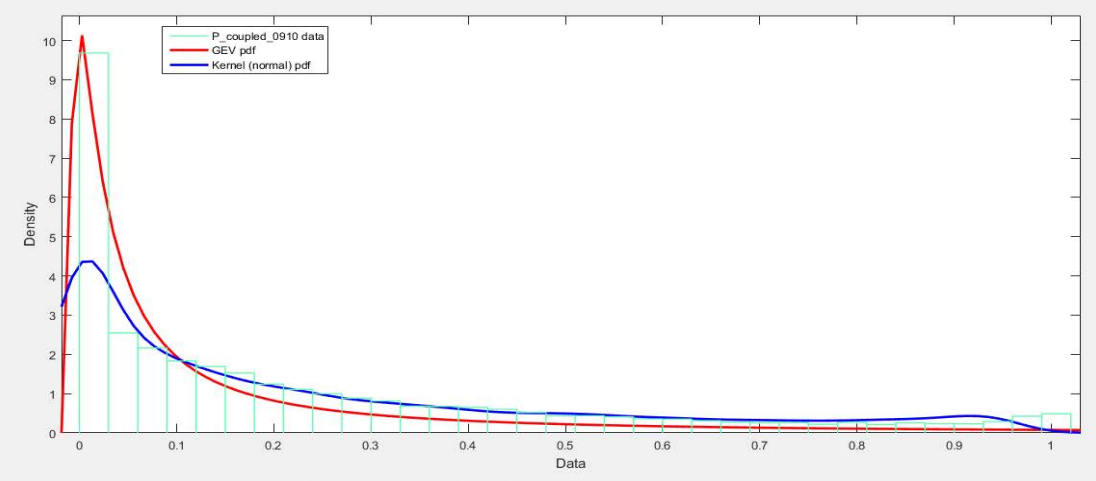

(b) Fitting GEV and Kernel PDFs to predicted power curve from coupled model (2009-2010)

Figure A.4.1: Probability density functions (PDFs) for power output

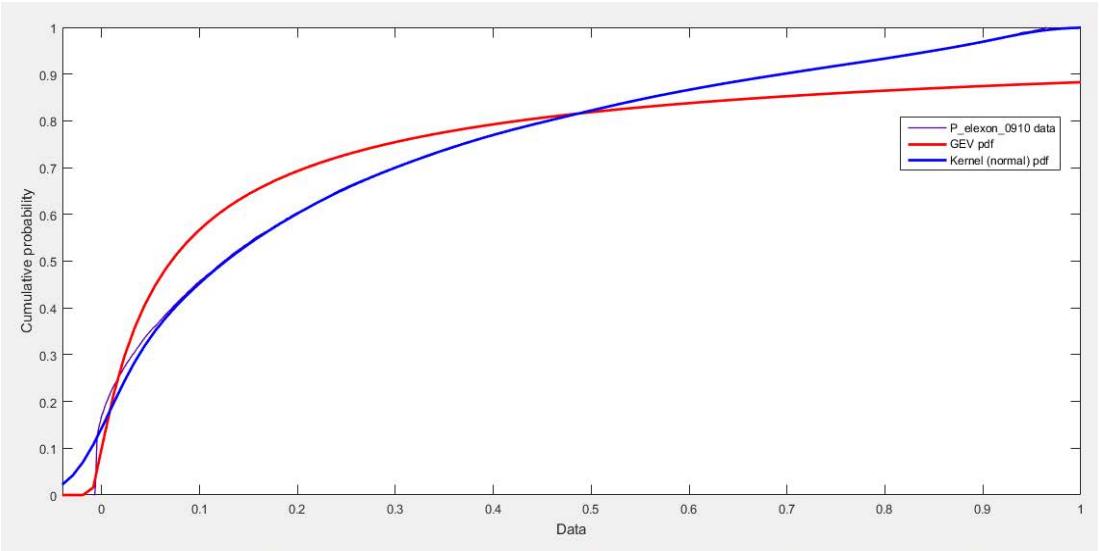

(a) Fitting GEV and Kernel CDFs to actual power production from ELEXON (2009-2010)

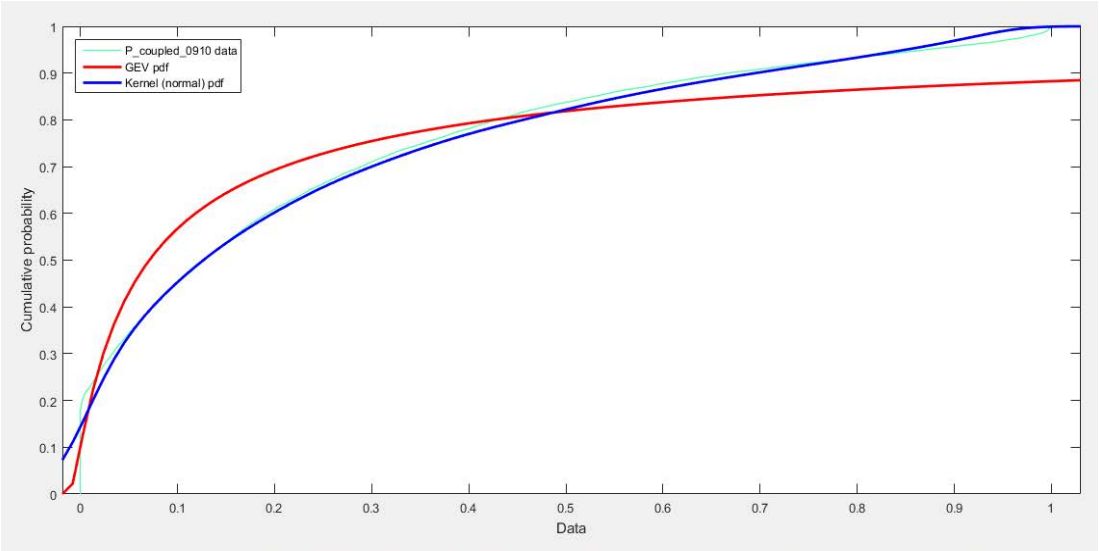

(b) Fitting GEV and Kernel CDFs to predicted power curve from coupled model (2009-2010)

Figure A.4.2: Cummulative distribution functions (CDFs) for power output

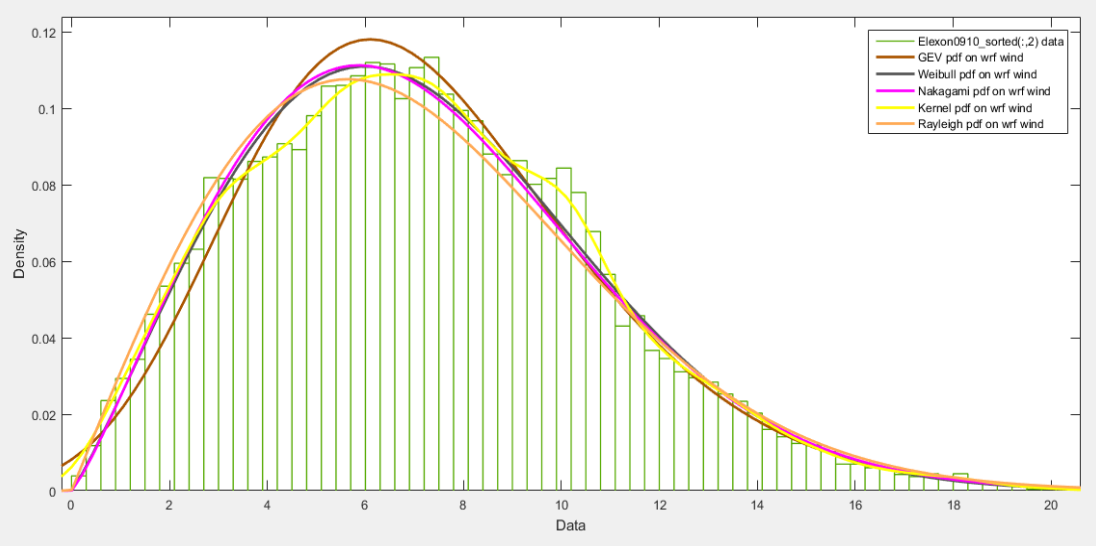

(a) Fitting PDF types to WRF wind speed (2009-2010)

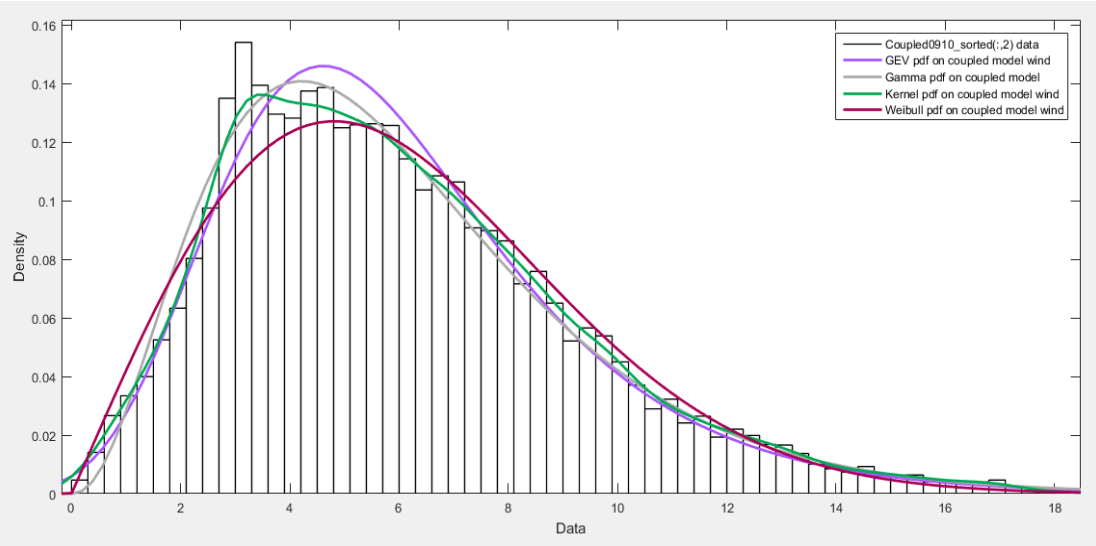

(b) Fitting PDF types to coupled model wind speed (2009-2010)

Figure A.4.3: Probability density functions (PDFs) for wind speeds

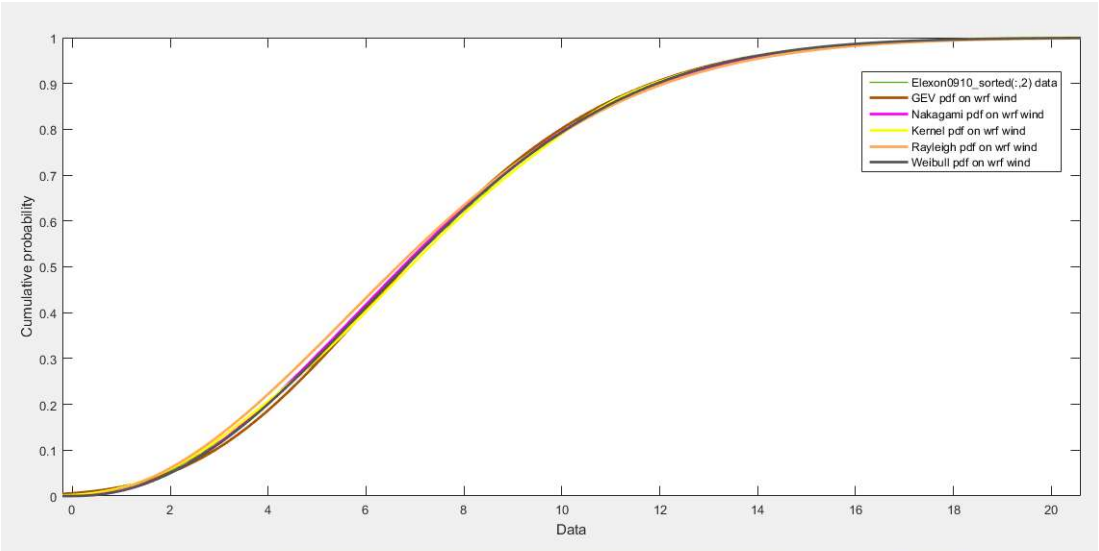

(a) Fitting CDF types to WRF wind speed (2009-2010)

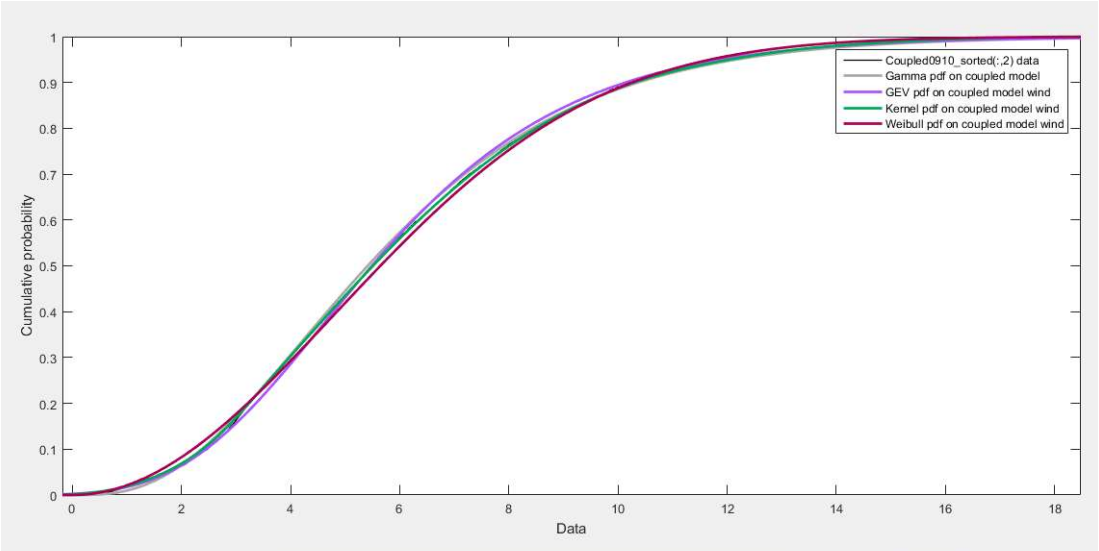

(b) Fitting CDF types to coupled model wind speed (2009-2010)

Figure A.4.4: Cummulative distribution functions (CDFs) for wind speed

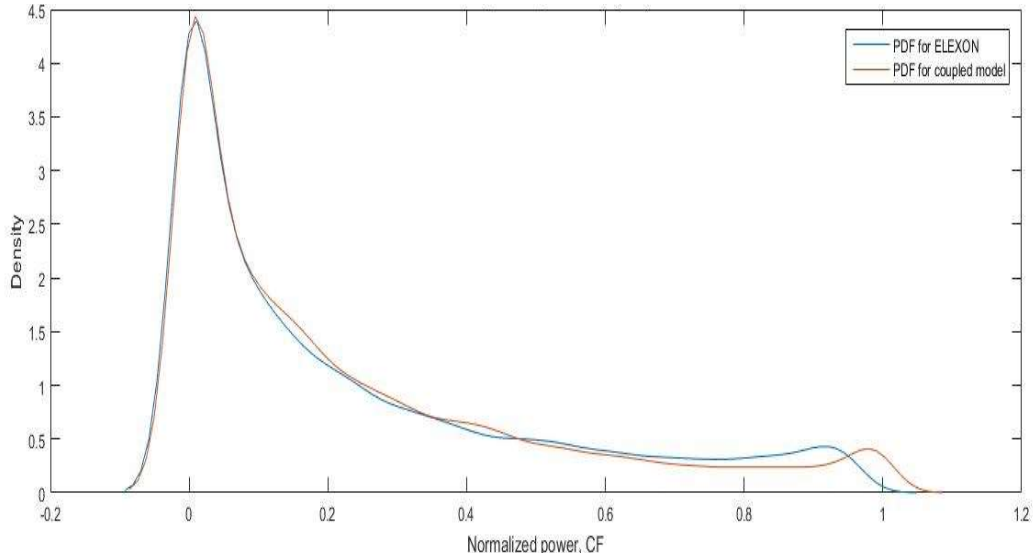

(a) Kernel PDF for both ELEXON and model power outputs (2009-2010)

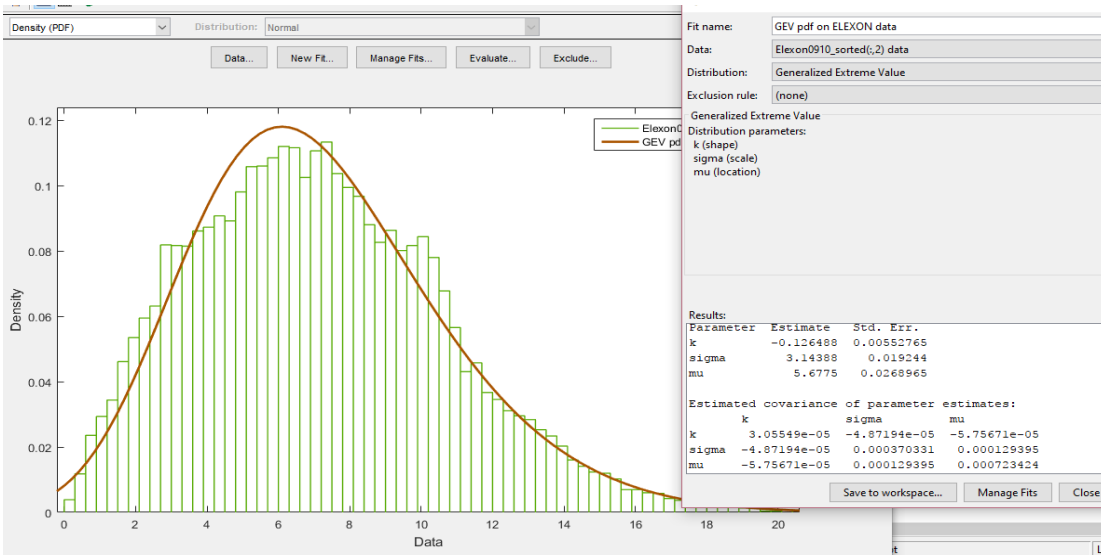

(b) Generalized extreme value PDF for ELEXON power output (2009-2010)

Figure A.4.5: Generalized extreme value and Kernel PDFs for power output

Bibliography

[1] International Renewable Energy Agency (IRENA), "Wind power - technology Brief. Energy 1–24," 2016. [Online]. Available: doi:10.1049/ep.1976.0231 xv, 1, 2

[2] European Wind Energy Association (EWEA), "Wind in power - 2015 European statistics 1-24," 2016. [Online]. Available: http://www.ewea.org/Statistics/ 1

[3] Department of Energy & Climate Change, "UK renewable energy roadmap," nov 2013. [Online]. Available: https://www.gov.uk/government/collections/uk-renewable-energy-roadmap5August2017) 1, 2

[4] J. Dowds, P. Hines, T. Ryan, W. Buchanan, E. Kirby, J. Apt, and P. Jaramillo, *A review of large-scale wind integration studies.* Renewable and Sustainable Energy Reviews, 2015. 8, 9

[5] H. Holttinen, M. O'Malley, J. Dillon, D. Flynn, M. Milligan, L. Söder, A. Orths, H. Abilgaard, J. C. Smith, and F. van Hulle, "Recommendations for Wind Integration Studies," in *Proc. 11th Int. Work. Large-Scale Integr. Wind Power into Power Syst. as well as Transm. Networks Offshore Wind Power Plants*, 2012. xv, 8

[6] S. Hewitt, L. Margetts, and A. Revell, "Building a Digital Wind Farm," in *Archives of Computational Methods in Engineering*, vol. 25, pp. 879–899, 2017. [Online]. Available: https://doi.org/10.1007/s11831-017-9222-7 xv, 11

[7] S. L. Hawkins, *'High resolution reanalysis of wind speeds over the British Isles for wind energy integration'*, Available at, 2012. [Online]. Available: https://www.era.lib.ed.ac.uk/handle/1842/78985August2017) 14, 15, 17, 20, 23, 24, 29, 31, 33, 62, 68, 80

[8] B. P. Hayes, A. J. Collin, I. Hernando-Gil, J. L. Acosta, S. Hawkins, G. P. Harrison, and S. Z. Djokic, "All-scale modelling of wind generation and responsive demand in power system studies," in *IEEE Power Energy Soc. Gen. Meet.*, 2012. 14

[9] "What is a GCM?" 2013. [Online]. Available: http://ipcc-data.org/guidelines/pages/gcm{_}guide.html5August2017) xv, 14

[10] B. W. Shen, R. Atlas, J. D. Chern, O. Reale, S. J. Lin, T. Lee, and J. Chang, "The 0.125 degree finite-volume general circulation model on the NASA Columbia supercomputer: Preliminary simulations of mesoscale vortices," *Geophys. Res. Lett.*, vol. 33, 2006. 14

[11] B. W. Shen, R. Atlas, O. Reale, S. J. Lin, J. D. Chern, J. Chang, C. Henze, and J. L. Li, "Hurricane forecasts with a global mesoscale-resolving model: Preliminary results with Hurricane Katrina (2005)," *Geophys. Res. Lett.*, vol. 33, 2006. 14

[12] B. W. Shen, W. K. Tao, W. K. Lau, and R. Atlas, "Predicting tropical cyclogenesis with a global mesoscale model: Hierarchical multiscale interactions during the formation of tropical cyclone Nargis (2008)," *J. Geophys. Res. Atmos.*, vol. 115, 2010. 15

[13] G. Heinemann, "'On the consideration of mesoscale transports in climate modelling'," *Theor. Appl. Climatol.*, vol. 83, no. 1-4, pp. 35–50, 2006. 15

[14] R. J. Ronda, G. J. Steeneveld, B. G. Heusinkveld, J. J. Attema, A. A. M. Holtslag, R. J. Ronda, G. J. Steeneveld, B. G. Heusinkveld, J. J. Attema, and A. A. M. Holtslag, "Urban fine-scale forecasting reveals weather conditions with unprecedented detail," *Bull. Am. Meteorol. Soc. BAMS-D-*, vol. 1, pp. 16–297, 2017. 15

[15] R. A. Pielke, "Examples of Mesoscale Models," *Int. Geophys.*, vol. 98, pp. 427–500, 2013. 15

[16] I. Orlanski, *A rational Subdivision of Scales for Atmospheric Processes.* American Meteorological Society, 1975. 15

[17] *WRF Model Users' Page*, Available at, 2017. [Online]. Available: http://www2.mmm.ucar.edu/wrf/users/6August2017) xv, 15, 16, 17

[18] A. Bowen and N. Mortensen, "Exploring the limits of WAsP: The Wind Atlas Analysis and Application Program," *Eur. Union Wind Energy Conf.*, pp. 584–587, 1996. 17

[19] A. J. Bowen and N. G. Mortensen, *WAsP prediction errors due to site orography.* Riso-E Report, 2004. 17

[20] A. D. Griffiths and J. H. Middleton, "Simulations of separated flow over two-dimensional hills," *J. Wind Eng. Ind. Aerodyn.*, vol. 98, pp. 155–160, 2010. 17

[21] D. Randall, *Reynolds Averaging*, Available at, 2009. [Online]. Available: https://core.ac.uk/display/226596876August2017) 18

[22] S. Hussain, P. H. Oosthuizen, and A. Kalendar, "Evaluation of various turbulence models for the prediction of the airflow and temperature distributions in atria," *Energy Build.*, vol. 48, pp. 18–28, 2012. 18

[23] C. Abiven, *No Title.* Are Mesoscale-coupled CFD Models the next generations models, in: EWEA Technology Workshop Resource Assessment, 2013. 18

[24] V. D. Jothiprakasam, E. Dupont, and B. Carissimo, *Downscaling wind energy resource from mesoscale to CFD model and data assimilating field measurements into CFD model,*

in: EWEA 2013. Wien, 2013. 18

[25] B. T. Olsen, A. N. Hahmann, A. M. Sempreviva, J. Badger, and H. E. Jørgensen, "An intercomparison of mesoscale models at simple sites for wind energy applications," *Wind Energy Sci.*, vol. 2, pp. 211–228, 2017. 18

[26] W. Energy, "Wind Energy literature survey no. 19 A," *Wind Energy*, vol. 14, pp. 155–157, 2011. 18

[27] U. S. D. of Commerce, *ESRL Themes: Surface and Planetary Boundary Layer Processes*, Available at. [Online]. Available: https://www.esrl.noaa.gov/research/themes/pbl/6August2017) 18, 19

[28] C. Anderson, "Principles of Wind Energy - Wind and its Characteristics," *Lect. notes Distrib. Princ. Wind Energy course PGEE*, vol. 11029, 2017. xv, 19, 20

[29] F. T. M. Nieuwstadt and P. G. Duynkerke, "Turbulence in the atmospheric boundary layer," *Atmos. Res.*, vol. 40, pp. 111–142, 1996. 20

[30] B. Sanderse, "Aerodynamics of Wind Turbine Wakes: Literature Review," Energy Research Center of the Netherlands (ECN), ECN-E–09-016, Petten, The Netherlands, Tech. Rep 5, 46, Tech. Rep., 2009. xv, 20, 32

[31] M. Princevac, "University of California Riverside Department of Mechanical Engineering," 2008. [Online]. Available: http://www.engr.ucr.edu/{~}marko/urban{_}rural{_}field{_}measurements{_}files/urban{_}1.jpg xv, 21

[32] N. E. Theeuwes, G.-j. Steeneveld, R. J. Ronda, M. W. Rotach, and A. a. M. Holtslag, "Cool city mornings by urban heat," *Environ. Res. Lett.*, vol. 10, no. 11402, p. 2, 2015. xv, 21

[33] T. Burton, D. Sharpe, N. Jenkind, and E. Bossanyi, *Wind Energy Handbook*. Ltd: John Wiley & Sons, 2001. 21, 33

[34] M. O. Hansen, *Aerodynamics of Wind Turbines*. Taylor & Francis Group: Routledge, 2015. 21

[35] S. Trzaska and E. Schnarr, "A review of downscaling methods for climate change projections," *United States Agency Int. Dev. by Tetra Tech ARD*, pp. 1–42, 2014. xv, 24

[36] F. Wippermann and G. Gross, "On the construction of orographically influenced wind roses for given distributions of the large-scale wind," *Beitr. Phys. Atmos.*, vol. 54, pp. 492–501, 1981. 23

[37] D. Heimann, "Estimation of regional surface layer wind field characteristics using a three-layer mesoscale model," *Beitr. Phys. Atmos.*, vol. 59, pp. 518–537, 1986. 23

[38] F. Frey-Buness, D. Heimann, and R. Sausen, "A statistical-dynamical downscaling procedure for global climate simulations," *Theoretical and Applied Climatology*, vol. 50, no. 3, pp. 117–131, Sep. 1995. [Online]. Available: https://doi.org/10.1007/BF00866111 23

[39] R. Benestad, *Downscaling Climate Information Downscaling Climate Information Summary and Keywords.* Oxford: Research Encyclopedia of Climate Science, 2016. 24, 25

[40] M. Ekström, M. R. Grose, and P. H. Whetton, *An appraisal of downscaling methods used in climate change research.* Wiley Interdisciplinary Reviews: Climate Change, 2015. 24, 25

[41] J. Dowell, S. Weiss, D. Hill, and D. Infield, "Short-term spatio-temporal prediction of wind speed and direction," *Wind Energy*, vol. 17, pp. 1945–1955, 2014. 24

[42] B. M. Sanandaji, A. Tascikaraoglu, K. Poolla, and P. Varaiya, "Low-dimensional models in spatio-temporal wind speed forecasting, in: Proceedings of the American Control Conference," *Inst. Electr. Electron. Eng. Inc*, pp. 4485–4490, 2015. 24

[43] C. Portal and I. for the European Network of Earth System Modelling (IS-ENES2), "Climate impact portal for exploration, visualization and analysis of climate model data," mar 2017. [Online]. Available: https://climate4impact.eu/impactportal/help/contactexpert.jsp?q=Downscaling6August2017) 24, 25

[44] H. Kooijman, "Power curve , energy yield , and customer value, in: EWEA Technology Workshop Resource Assessment," *GE Power Water, Wind Farm Eng. Dublin, Ireland, pp*, pp. 25–26, 2013. 28

[45] D. Carvalho, A. Rocha, C. S. Santos, and R. Pereira, "Wind resource modelling in complex terrain using different mesoscale-microscale coupling techniques," *Appl. Energy*, vol. 108, pp. 493–504, 2013. 28

[46] M. Bilal, Y. Birkelund, M. Homola, and M. S. Virk, "Wind over complex terrain" *Microscale Model. with two types mesoscale Wind. Nygårdsfjell. Renew. Energy*, vol. 99, pp. 647–653, 2016. 28

[47] J. Bleeg, D. Digraskar, J. Woodcock, and J. F. Corbett, "Modeling stable thermal stratification and its impact on wind flow over topography, in: Wind Energy," in *John Sons Ltd*, 2015, pp. 369–383. 28

[48] A. Sapronova, C. Meissner, and M. Mana, "'Improving an Accuracy of ANN-Based Mesoscale-Microscale Coupling Model by Data Categorization: With Application to

Wind Forecast for Offshore and Complex Terrain Onshore Wind Farms', in," in *Int. Work. Data Anal. Renew. Energy Integr. , Cham (Lecture Notes Comput. Sci.*, 2014, pp. 61–66. 29

[49] J. Sanz Rodrigo, R.A. Chavez-Arroyo, P. Moriarty, M. Churchfield, B. Kosovic, P.E. Rethore, K.S. Hansen, A. Hahmann, J.D. Mirocha, and D. Rife *Mesoscale to microscale wind farm flow modeling and evaluation.* Wiley Interdisciplinary Reviews:Energy and Environment 6, 2017. 29

[50] A. U. Haque, P. Mandal, J. Meng, and M. Negnevitsky, "Wind speed forecast model for wind farm based on a hybrid machine learning algorithm," *Int. J. Sustain. Energy*, vol. 34, 2015. 29

[51] The National Center for Atmospheric Research (NCAR), *Renewable Energy - Research Applications Laboratory 2015 Annual Report*, Available at. [Online]. Available: https://nar.ucar.edu/2015/ral/renewable-energy6August2017) xv, 29

[52] D. Renkema, *Validation of wind turbine wake models Using wind farm data and wind tunnel measurements*, Available at, 2007. [Online]. Available: http://lr.home.tudelft.nl/fileadmin/Faculteit/LR/Organisatie/Afdelingen{_}en{_}Leerstoelen/Afdeling{_}AEWE/Wind{_}Energy/Education/Masters{_}Projects/Finished{_}Master{_}projects/doc/Douwe{_}Renkema{_}r.pdf6August2017) 31, 33, 37, 38, 39

[53] F. Seim, A. R. Gravdahl, and M. S. Adaramola, "Validation of kinematic wind turbine wake models in complex terrain using actual windfarm production data," *Energy*, vol. 123, pp. 742–753, 2017. 31, 39, 42

[54] J. F. Manwell, J. G. Mcgowan, and A. L. Rogers, *Wind Energy Explained Theory, Design and Application Second Edition, 2nd ed, Wiley.* Ltd., England: John Wiley & Sons, 2009. 31, 33

[55] R. J. Barthelmie, O. Rathmann, S. T. Frandsen, K. S. Hansen, E. S. Politis, J. Prospathopoulos, K. Rados, D. Cabezón, W. Schlez, J. Phillips, A. Neubert, J. G. Schepers, and S. P. van der Pijl, "Modelling and measurements of wakes in large wind farms," *J. Phys. Conf. Ser.*, vol. 75, p. 12049, 2007. 31

[56] A. J. R. Mclean and G. Hassan, *Equivalent Wind Power Curves.* Garrad Hassan: Report for the Trade Wind Project. October, 2008. 31

[57] O. Anaya-Lara, N. Jenkins, J. Ekanayake, P. Cartwright, and M. Hughes, *Wind Energy Generation Modelling and Control, Wiley.* John Wiley & Sons, 2009. 31

[58] S. N. Laboratories, *Computational Fluid Dynamics Simulations Provide Insight for Rotor Design, Energy and Climate - Secure & Sustainable*

Energy Future, Available at, 2014. [Online]. Available: http://energy.sandia.gov/computational-fluid-dynamics-simulations-provide-insight-for-rotor-design/6August2017) xv, 32

[59] G. R. Pirrung, H. A. Madsen, T. Kim, and J. Heinz, "A coupled near and far wake model for wind turbine aerodynamics," *Wind Energy*, vol. 19, pp. 2053–2069, 2016. 33

[60] G. Pirrung, V. Riziotis, H. Madsen, M. Hansen, and T. Kim, "Comparison of a Coupled Near and Far Wake Model with a Free Wake Vortex Code," *Wind Energy Sci. Discuss.*, pp. 1–28, 2016. 33

[61] M. Magnusson, "Near-wake behaviour of wind turbines," *J. Wind Eng. Ind. Aerodyn.*, vol. 80, pp. 147–167, 1999. 33

[62] K. Bhaganagar and M. Debnath, "Implications of stably stratified atmospheric boundary layer turbulence on the near-wake structure of wind turbines," *Energies*, vol. 7, pp. 5740–5763, 2014. 33

[63] Y. Wang, V. Leble, M. White, and G. N. Barakos, "No Title," *Wake Charact. Large-scale Wind Turbines*, vol. 2015, pp. 87–98, 2015. 33

[64] S. Salunkhe, S. Bhushan, D. Thompson, and T. O'Doherty, "Analysis and Validation of Hydrokinetic Turbine Turbulent Wake Predictions," in *October*, A. Wave and T. E. C. (awtec, Eds. Singapore, 2016, pp. 10–12. 33, 34

[65] H. F. Wang and Y. Zhou, "The finite-length square cylinder near wake," *J. Fluid Mech.*, vol. 638, p. 453, 2009. 33

[66] J. N. Sørensen, R. Mikkelsen, S. Sarmast, S. Ivanell, and D. Henningson, "Determination of Wind Turbine Near-Wake Length Based on Stability Analysis," *J. Phys. Conf. Ser.*, vol. 524, p. 12155, 2014. 33

[67] P. Hashemi-Tari, K. Siddiqui, M. Refan, and H. Hangan, "Wind Tunnel Investigation of the Near-wake Flow Dynamics of a Horizontal Axis Wind Turbine," *J. Phys. Conf. Ser.*, vol. 524, p. 12176, 2014. 33, 34

[68] W. Tong, S. Chowdhury, A. Mehmani, J. Zhang, and A. Messac, "Sensitivity of Array-Like and Optimized Wind Farm Output to Key Factors and Choice of Wake Models, in: Volume 3A: 39th Design Automation Conference," in *ASME*. p. V03AT03A024, 2013. 33

[69] T. Göçmen, P. V. D. Laan, P. E. Réthoré, A. P. Diaz, G. C. Larsen, and S. Ott, *Wind turbine wake models developed at the technical university of Denmark: A review.* Renewable and Sustainable Energy Reviews, 2016. 34, 39

[70] P. Dvorak, "A closer look at wake loss modeling based on production data. [online] Windpower Engineering & Development." [Online]. Available: http://www.windpowerengineering.com/construction/simulation/closer-look-wake-loss-modeling-based-production-data/ 34, 35, 37

[71] P. D. G. J. W. van Bussel, *WIND ENERGY ONLINE READER*, Video frame [online] Available at:, 2008. [Online]. Available: http://mstudioblackboard.tudelft.nl./duwind/Windenergyonlinereader/index.htm xv, 35

[72] D. Zigras and K. Moennich, "Farm Efficiencies in Large Wind Farms, in: {G}erman Wind Energy Conference," in *Bremen.* p. 4: Germany, 2006. 36

[73] V. Timmers, "Farm Level Power Curve for Wind Integration Studies," Master's thesis, Institute for Energy Systems, University of Edinburgh, 2017. xv, 36, 37, 39, 44, 86, 87

[74] S. Jeon, B. Kim, and J. Huh, "Comparison and verification of wake models in an onshore wind farm considering single wake condition of the 2 MW wind turbine," *Energy*, vol. 93, 2015. 37, 39

[75] W. Schlez, A. Umaña, R. Barthelmie, G. Larsen, K. Rados, B. Lange, G. Schepers, and T. Hegberg, *ENDOW: Improvement of Wake Models within Offshore Wind Farms.* 281-287: Wind Engineering 25, 2009. 37, 39

[76] G. C. Larsen, H. A. Madsen, and N. N. Sorensen, "Mean Wake Deficit in the near Field," in *Eur. Wind Energy Conf. Exhib.* Spain, 2003: Madrid, 2003, pp. 1–5. 38, 39

[77] A. Duckworth and R. J. Barthelmie, *Validation of wind turbine wake models.* Wind Engineering, 2008. 39

[78] M. Thørgersen, T. Sørensen, and P. Nielsen, "WindPRO/PARK: Introduction to Wind Turbine Wake Modelling and Wake Generated Turbulence," *EMD Int. A/S,...*, vol. 61, 2005. 39

[79] M. Zanganeh and V. Khalajzadeh, "Validation of the WAsP Model for a Terrain Surrounded by Mountainous Region," *Eng. Technol.*, pp. 379–383, 2011. 39

[80] International Electrotechnical Commission (IEC), "Wind turbines – Part 1: Design requirements," Tech. Rep., 2005. [Online]. Available: https://webstore.iec.ch/preview/info{_}iec61400-1{%}7Bed3.0{%}7Den.pdf 39

[81] N. Charhouni, M. Sallaou, and A. Arbaoui, *'Qualification of Three Analytical Wake Models'*, Available at, 2016. [Online]. Available: http://www.davidpublisher.com/Public/uploads/Contribute/57b12255d1e46.pdf5August2017) 39

[82] S. Frandsen, R. Barthelmie, S. Pryor, O. Rathmann, and S. et. al. Larsen, *'The necessary distance between large wind farms offshore-study Title: The necessary distance between large wind farms offshore-study'*, Available at:, 2004. [Online]. Available: http://orbit.dtu.dk/fedora/objects/orbit:90472/datastreams/file{_}7711064/content5August2017) 39

[83] W. Tong, S. Chowdhury, J. Zhang, and A. Messac, "Impact of Different Wake Models on the Estimation of Wind Farm Power Generation. 12th AIAA Aviation Technology," in *Integration.* and Operations (ATIO) Conference and 14th AIAA/ISSMO, 2012, pp. 1–13. xv, xvii, 40, 41, 42, 43, 114

[84] L. Tian, W. Zhu, W. Shen, N. Zhao, and Z. Shen, "Development and validation of a new two-dimensional wake model for wind turbine wakes," *J. Wind Eng. Ind. Aerodyn.*, vol. 137, 2015. 40

[85] T. Ishihara, A. Yamaguchi, and Y. Fujino, "Development of a New Wake Model Based on a Wind Tunnel Experiment," Tech. rep, Global Wind, 1, Tech. Rep., 2004. 40, 41, 42

[86] A. Mittal and K. Sreenivas, ""Investigation of Two Analytical Wake Models Using Data from Wind Farms." International Mechanical Engineering Congress and Exposition," N. Denver, Ed., 2011. 40

[87] G. Steinfeld, "Wind energy meteorology - modeling of wind turbine wakes." 2011. [Online]. Available: https://www.slideshare.net/Jupiter276/vl-wind-energymeteorologyss1109windfarmmodelinggerald?next{_}slideshow=1 43

[88] J. F. Ainslie, "Calculating the flow field in the wake of wind turbines," *J. Wind Eng. Ind. Aerodyn.*, vol. 27, pp. 213–224, 1988. 43

[89] M. E. Harrison, W. M. J. Batten, L. S. Blunden, L. E. Myers, and A. S. Bahaj, "2nd int. conf. ocean energy," F. Brest, Ed., 2008, pp. 1–9. 43

[90] Sustainable Energy Authority of Ireland (SEIA), "Guidelines for Wind Farm Development," 2014. [Online]. Available: http://www.seai.ie/Renewables/Wind{_}Energy/Wind{_}Farms/Wind{_}Farm{_}Development/Guidelines{_}for{_}wind{_}farm{_}development/ 45

[91] R. Weibel and M. Heller, *Digital Terrain Modeling.* Geographical Information Systems: Principles and Applications, 1991. xvi, 45, 46

[92] Z. Li, Q. Zhu, and C. M. Gold, *Digital terrain modelling.* New York: Principles and methodology, 2005. 45

[93] S. N. Heritage, "Planning and Development of Renewable Energy Projects: Guidance on Visual Representation of Wind Farms," Tech. Rep., 2017. [Online]. Available: http://www.

snh.gov.uk/planning-and-development/renewable-energy/visual-representation/ 45, 46

[94] W. Tian, A. Ozbay, and H. Hu, *Terrain Effects on Characteristics of Surface Wind and Wind Turbine Wakes, in: Procedia Engineering.* pp. 542-548: Elsevier Ltd, 2015. 46, 47

[95] P. Moreno, A. R. Gravdahl, and M. Romero, "Wind flow over complex terrain: application of linear and CFD models, in: 2003 European Wind Energy Conference and Exhibition," S. Madrid, Ed., 2003. 47

[96] T. Wallbank, *WindSim Validation Study: CFD validation in Complex terrain*, 2008. 47, 59

[97] B. Efe, S. Mentes, Y. Unal, E. Tan, E. Unal, T. Ozdemir, B. Barutcu, B. Onol, and S. Topcu, "72hr forecast of wind power in Manisa," in *Turkey by using WRF Model coupled to Wind.* International Conference on Renewable Energy Research and Applications, ICRERA 2012, 2012. 47

[98] R. Chavez-Arroyo, O. Probst, and C. Meissner, "Evaluation of the wind resource for a coastal site in Mexico by combining WindSim with WRF," in *EWEA2012presentation*, 2012. 47

[99] L. F. Ramos, C. Krüger, and M. R. D. Moraes, *Levantamento do potencial eólico da reigão da campanha meridional do Rio Grande do Sul com o modelo de mesoescala WRF e o modelo CFD WindSim.* DELOS (Desarrollo Local Sostenible), 2013. 47

[100] B. Yaksi, S. Akin, and Y. A. Kara, "A Wind Power Plant Feasibility Study for Bursa, Gemlik Region in Turkey by WINDSIM Software," *Int. J. Energy Appl. Technol.*, vol. 3, pp. 72–76, 2016. 47

[101] T. S. D. Karthik, "Turbulence models and their applications," 10th Indo-German Winter Academy 1-52, Tech. Rep., 2011. 50, 52

[102] CFD Online, "Turbulence modeling," vol. 11, p. 2017, 2013. [Online]. Available: https://www.cfd-online.com/Wiki/Turbulence{_}modeling 51, 55

[103] W. P. Jones and B. E. Launder, "'The prediction of laminarization with a two-equation model of turbulence'," *Int. J. Heat Mass Transf.*, vol. 15, no. 2, pp. 301–314, 1972. 51

[104] B. Launder and D. Spalding, "The numerical computation of turbulent flows," *Comput. Methods Appl. Mech. Eng.*, vol. 3, p. 2, 1974. 51

[105] A. R. Gravdahl, "Meso Scale Modeling with a Reynolds Averaged Navier - Stokes Solver Assessment of wind resources along the Norwegian coast, in: 31st IEA Experts Meeting State of the Art on Wind Resource Estimation," in *VECTOR AS.* Denmark: Risø, 1998, pp. 1–14. xviii, 51, 52, 53, 57, 58

[106] D. Kuzmin and O. Mierka, *'On the implementation of the k-ϵ turbulence model in incompressible flow solvers based on a finite element discretization'*, 2006. [Online]. Available: http://num.math.uni-goettingen.de/bail/documents/proceedings/mierka.pdf26July2017) xviii, 51, 53

[107] H. A. Panofsky, H. Tennekes, D. H. Lenschow, and J. C. Wyngaard, "The characteristics of turbulent velocity components in the surface layer under convective conditions," *Boundary-Layer Meteorol.*, vol. 11, pp. 355–361, 1977. 52

[108] A. Z. Dhunny, M. R. Lollchund, and S. D. D. V. Rughooputh, "'Wind energy evaluation for a highly complex terrain using Computational Fluid Dynamics (CFD)'," in *Renew. Energy.* pp. 1–9: 101, 2017. 52

[109] Q. Chen, "Comparison oF Different k-ϵ Models for Indoor Air Flow Computations," *Numer. Heat Transf. Part B Fundam.*, vol. 28, pp. 353–369, 1995. 52

[110] S. Murakami, N. Ohira, and S. Kato, "CFD Analysis of a Thermal Plume and the Indoor Air Flow Using k–ϵ Models with Buoyancy Effects," T. Flow and Combustion, Eds. 113–134: 63, 1999. 52

[111] F. Martelli and W. Rodi, *'Engineering turbulence modelling and experiments 2'*, proceeding ed., Florence, Italy, 31 May-2 June, 1993., 1993. [Online]. Available: https://www.elsevier.com/books/engineering-turbulence-modelling-and-experiments-2/martelli/978-0-444-89802-926July2017) 52

[112] O. Temel and J. van Beeck, "Two-equation eddy viscosity models based on the Monin-Obukhov similarity theory," *Appl. Math. Model.*, vol. 42, pp. 1–16, 2017. xviii, 53, 58

[113] A. N. Kolmogorov, *Selected Works of A. N.* Springer Netherlands, Dordrecht, 1991, vol. Volume III. 53

[114] S. Krist, R. Biedron, and C. Rumsey, *CFL3D user's manual (version 5.0).* Hampton, Va.: National Aeronautics and Space Administration, Langley Research Center, 1998. 55

[115] C. G. Speziale, R. Abid, and E. C. Anderson, "Critical evaluation of two-equation models for near-wall turbulence," *AIAA J.*, vol. 30, pp. 324–331, 1992. 56

[116] F. R. Menter, "Improved two-equation k-omega turbulence models for aerodynamic flows," NASA Technical Memorandum 1-31, Tech. Rep., 1992. 56

[117] A. Huser, P. J. Nilsen, and H. Skåtun, "Application of k-ϵ model to the stable ABL: Pollution in complex terrain," *J. Wind Eng. Ind. Aerodyn.*, pp. 67–68, 425–436, 1997. 58

[118] T. Koblitz, A. Bechmann, J. Berg, A. Sogachev, N. Sørensen, and P.-e. Réthoré, "Atmospheric stability and complex terrain: comparing measurements and CFD," *J.*

Phys. Conf. Ser., vol. 555, p. 12060, 2014. 59

[119] D. B. Spalding, "A general purpose computer program for multi-dimensional one- and two-phase flow," *Math. Comput. Simul.*, vol. 23, pp. 267–276, 1981. 59

[120] M. R. Malin and D. B. Spalding, "The prediction of Turbulent Jets & Plumes by Use of the k W Model of Turbulence," *Physicochem. Hydrodyn.*, vol. 5, pp. 153–198, 1984. 59

[121] H. Rosten, D. Spalding, and D. Tatchell, "PHOENICS: A General-Purpose Program for Fluid-Flow," *Heat-trans. Chem. Process.*, vol. 11, p. 2017, aug 1983. [Online]. Available: https://link.springer.com/chapter/10.1007/978-3-662-02335-8{_}49 59

[122] B. Blocken, T. Stathopoulos, and J. Carmeliet, "CFD simulation of the atmospheric boundary layer: wall function problems," *Atmos. Environ.*, vol. 41, pp. 238–252, 2007. 59

[123] "Factbook: Wind power - growth onshore, hope offshore - a.t. kearney energy transition institute." xvi, 93, 94

[124] "Wind in Power: 2017 European Statistics," 2017. [Online]. Available: https://windeurope.org/about-wind/statistics/european/wind-in-power-2017/ xvi, 94